

## **CryoEM structures of the human CLC-2 voltage gated chloride channel reveal a ball and chain gating mechanism**

Mengyuan Xu<sup>1</sup>, Torben Neelands<sup>1</sup>, Alexander S. Powers<sup>2,3,4,5</sup>, Yan Liu<sup>6</sup>, Steven D. Miller<sup>2</sup>, Grigore Pintilie<sup>7</sup>, J. Du Bois<sup>2</sup>, Ron O. Dror<sup>1,3,4,5</sup>, Wah Chiu<sup>6,7</sup>, Merritt Maduke<sup>1</sup>

<sup>1</sup>Department of Molecular and Cellular Physiology, Stanford University, Stanford, CA 94305

<sup>2</sup>Department of Chemistry, Stanford University, Stanford, CA 94305

<sup>3</sup>Department of Computer Science, Stanford University, Stanford, CA 94305

<sup>4</sup>Department of Structural Biology, Stanford University, Stanford, CA 94305

<sup>5</sup>Institute for Computational and Mathematical Engineering, Stanford University, Stanford, CA 94305

<sup>6</sup>Division of CryoEM and Bioimaging, SSRL, SLAC National Accelerator Laboratory, Stanford University, Menlo Park 94025

<sup>7</sup>Department of Bioengineering and Department of Microbiology and Immunology, Stanford University, Stanford, 94305

### **Correspondence:**

Dr. Merritt Maduke

279 Campus Drive West

Stanford, CA 94035

Tel: 650-723-9075

Email: [maduke@stanford.edu](mailto:maduke@stanford.edu)

**Keywords:** chloride channel, cryo-electron microscopy, electrophysiology

## **ABSTRACT:**

CLC-2 is a voltage-gated chloride channel that contributes to electrical excitability and ion homeostasis in many different mammalian tissues and cell types. Among the nine mammalian CLC homologs, CLC-2 is uniquely activated by hyperpolarization, rather than depolarization, of the plasma membrane. The molecular basis for the divergence in polarity of voltage gating mechanisms among closely related CLC homologs has been a long-standing mystery, in part because few CLC channel structures are available, and those that exist exhibit high conformational similarity. Here, we report cryoEM structures of human CLC-2 at 2.46 – 2.76 Å, in the presence and absence of the potent and selective inhibitor AK-42. AK-42 binds within the extracellular entryway of the Cl<sup>-</sup>-permeation pathway, occupying a pocket previously proposed through computational docking studies. In the apo structure, we observed two distinct apo conformations of CLC-2 involving rotation of one of the cytoplasmic C-terminal domains (CTDs). In the absence of CTD rotation, an intracellular N-terminal 15-residue hairpin peptide nestles against the TM domain to physically occlude the Cl<sup>-</sup>-permeation pathway from the intracellular side. This peptide is highly conserved among species variants of CLC-2 but is not present in any other CLC homologs. Previous studies suggested that the N-terminal domain of CLC-2 influences channel properties via a “ball-and-chain” gating mechanism, but conflicting data cast doubt on such a mechanism, and thus the structure of the N-terminal domain and its interaction with the channel has been uncertain. Through electrophysiological studies of an N-terminal deletion mutant lacking the 15-residue hairpin peptide, we show that loss of this short sequence increases the magnitude and decreases the rectification of CLC-2 currents expressed in mammalian cells. Furthermore, we show that with repetitive hyperpolarization WT CLC-2 currents increase in resemblance to the hairpin-deleted CLC-2 currents. These functional results combined with our structural data support a model in which the N-terminal hairpin of CLC-2 stabilizes a closed state of the channel by blocking the cytoplasmic Cl<sup>-</sup>-permeation pathway.

## 1 INTRODUCTION

2 Ion transport across the cell membrane establishes and exploits ion gradients to store energy  
3 and regulate electrical signaling. Ion transport is catalyzed by two classes of membrane proteins: ion  
4 channels and active transporters. The CLC “Chloride Channel” family encompasses both major ion-  
5 transport mechanisms: half of the CLC homologs are electrodiffusive chloride ( $\text{Cl}^-$ ) channels, and half  
6 are secondary active transporters that stoichiometrically exchange  $\text{Cl}^-$  for protons ( $\text{H}^+$ ) (Jentsch and  
7 Pusch, 2018). The occurrence of two mechanisms in one family suggests they operate by variations on  
8 a common theme (Miller, 2006), and experimental results revealed that CLC channels are “broken”  
9 transporters (Lisal and Maduke, 2008).

10 In both CLC channels and transporters, a conserved glutamate residue referred to as the  
11 “gating glutamate” ( $E_{\text{gate}}$ ) plays a central mechanistic role. High resolution CLC transporter structures  
12 show that this residue can adopt four different conformations (Dutzler et al., 2002; Dutzler et al., 2003;  
13 Feng et al., 2010; Chavan et al., 2020; Schrecker et al., 2020) (**Figure 1A**), which contribute to the  $\text{Cl}^-$   
14 / $\text{H}^+$  exchange mechanism (Accardi and Miller, 2004; Feng et al., 2012; Chavan et al., 2020; Leisle et  
15 al., 2020). Due to the small number of CLC channel structures relative to transporters, characterization  
16 of the central role for the  $E_{\text{gate}}$  residue in CLC channels has primarily relied on extensive functional  
17 studies of channel gating rather than observed  $E_{\text{gate}}$  side chain conformations (Jentsch and Pusch,  
18 2018). The first CLC channel structure reported was of bovine CLC-K (Park et al., 2017), a kidney-  
19 expressed homolog that is the lone CLC homolog lacking the  $E_{\text{gate}}$  (Kieferle et al., 1994). The only other  
20 CLC channel structures reported prior to 2023 are of the human CLC-1: one of these cryoEM structures  
21 shows  $E_{\text{gate}}$  in the “out” position (Park and MacKinnon, 2018) while the other lacked density for  $E_{\text{gate}}$   
22 (Wang et al., 2019). The  $E_{\text{gate}}$  “out” position was originally posited to be exclusive to the CLC channel  
23 homologs, as its positioning off to the side widens the  $\text{Cl}^-$ -permeation pathway and, in CLC-1, results in  
24 a continuous pathway (Park and MacKinnon, 2018). Such a continuous pathway precludes exchange  
25 coupling (Jardetzky, 1966; Miller, 2021). The open  $\text{Cl}^-$ -permeation pathway in the CLC-1 structure is  
26 consistent with the known functional properties of CLC-1 in the absence of an applied transmembrane

27 voltage. CLC-1 is a voltage-gated channel that is predominantly in the open state at zero mV (Altamura  
28 et al., 2020) (**Figure 1B**). At negative transmembrane voltages that favor CLC-1 closing, the  $E_{\text{gate}}$   
29 sidechain presumably moves to either the “middle” or “down” positions, or both, to occlude the channel  
30 pore.

31 CLC-2, like CLC-1, is a voltage-gated channel, but with opposite voltage dependence, opening  
32 instead of closing in response to hyperpolarization (Thiemann et al., 1992; Wang et al., 2017). CLC-2  
33 chloride channels are expressed in every mammalian organ, where they play diverse physiological  
34 functions (Thiemann et al., 1992; Lein et al., 2007; Duan, 2013; Stolting et al., 2014; Jentsch and  
35 Pusch, 2018). Perturbation of CLC-2 function is associated with human disease including  
36 leukodystrophies (Jentsch and Pusch, 2018), blindness (Xu et al., 2023), primary aldosteronism  
37 (Fernandes-Rosa et al., 2018; Scholl et al., 2018), and atrial fibrillation (Hansen et al., 2020). Despite  
38 their importance in human physiology, our understanding of CLC-2 molecular and physiological  
39 mechanisms is incomplete. A mystery concerning CLC-2 is why electrophysiological recordings of  
40 natively expressed channels reveal tremendous variation in voltage-dependent gating. CLC-2 currents  
41 are typically inwardly rectifying and activated by hyperpolarization, but the kinetics and degree of  
42 rectification are highly variable (Bosl et al., 2001; Jentsch and Pusch, 2018). In some cases, this  
43 variability is understood – for example interactions between CLC-2 and the astrocytic GlialCAM protein  
44 yields voltage-independent currents (Jeworutzki et al., 2012; Maduke and Reimer, 2012). Yet many  
45 questions about CLC-2 gating remain.

46 Like CLC-1, CLC-2 gating depends critically on  $E_{\text{gate}}$  (Niemeyer et al., 2003; Cederholm et al.,  
47 2010). At zero mV, CLC-2 is predominantly in the closed state (Stolting et al., 2013; Stolting et al.,  
48 2014; Jentsch and Pusch, 2018), presumably with  $E_{\text{gate}}$  blocking the pore. Such pore localization for  
49  $E_{\text{gate}}$  was modeled in a recent CLC-2 cryoEM structure (Ma et al., 2023); however, experimental density  
50 for the sidechain was lacking, and therefore the precise structure of this gate remains uncertain (**Figure**  
51 **1B**). Structures with improved resolution will be crucial to understanding CLC-2 gating, which involves  
52 interactions between  $E_{\text{gate}}$ ,  $\text{Cl}^-$  and  $\text{H}^+$ , with differential effects of external vs internal ions (Pusch et al.,



53 1999; Niemeyer et al., 2003; Sanchez-Rodriguez et al., 2010; Sanchez-Rodriguez et al., 2012; De  
54 Jesus-Perez et al., 2016). In addition to the  $E_{\text{gate}}$  mechanism, a “ball-and-chain” gating mechanism, in  
55 which the tethered N-terminus blocks the pore, has been proposed for CLC-2 (Grunder et al., 1992).  
56 However, this idea has been controversial (Varela et al., 2002) and the mechanism by which mutations  
57 in the N-terminal domain influence gating remains unknown. Because a structural foundation for  
58 understanding CLC-2 gating has been lacking, we determined cryoEM structures of CLC-2, in the  
59 presence and absence of the selective inhibitor AK-42 (Koster et al., 2020). The structures and  
60 complementary electrophysiology data presented here provide atomic insight into an N-terminal hairpin  
61 gating mechanism for CLC-2 channels.

62

## 63 RESULTS

### 64 Overview of cryoEM structure determination

65 Human CLC-2 (hCLC-2) protein was purified from cultured HEK293 GnT1<sup>-</sup> cells and further  
66 examined by cryoEM single particle analysis. Selected two-dimensional class averages showed a clear  
67 transmembrane domain embedded in a detergent micelle and features indicating an intracellular  
68 domain. Further refinement revealed a well-resolved transmembrane (TM) domain density at 2.46 Å,  
69 “CLC2-TM” (**Figure 2; Figure 2 - figure supplements 1-3**). Density for the C-terminal intracellular  
70 domain (CTD) is less well resolved. Such relatively weak density for the CTD relative to the TM domain  
71 was also observed in the cryoEM analysis of human CLC-1 (Park and MacKinnon, 2018; Wang et al.,  
72 2019), which is hCLC-2’s closest homolog. The CTD of CLC-0, a CLC-1 ortholog from *Torpedo*  
73 *marmorata* (Steinmeyer et al., 1991) displays large movements in spectroscopic studies (Bykova et al.,  
74 2006; Alioth et al., 2007). Thus, conformational flexibility in the CTD appears to be a shared feature  
75 within this branch of the CLC family. To further characterize CTD map density, 3D classification was  
76 performed. Amongst ten 3D classes identified, two showed significantly improved density for the CTD.  
77 With non-uniform refinement and further local refinement, we determined two conformations of CLC-2  
78 structures at 2.75 and 2.76 Å, respectively (**Figure 2 - figure supplement 2**).

79

## 80 **Structure of the transmembrane domain**

81 The TM region of CLC-2 displays a typical CLC family symmetric homodimeric structure, with  
82 each subunit containing an independent Cl<sup>-</sup> pathway (**Figure 2A, B**). In the cryoEM map, clear density  
83 for the E<sub>gate</sub> residue (E205 in CLC-2) reveals it occupying the “down” position, at the S<sub>cen</sub> Cl<sup>-</sup> binding site  
84 (**Figure 2C**). This downward E<sub>gate</sub> positioning has previously been observed only in the x-ray  
85 crystallographic structure of the *C. merolae* CLC transporter homolog (cmCLC) (Feng et al., 2010), but  
86 not in any CLC channel homolog (**Figure 2 – figure supplement 4A,B**). In the recent CLC-2 structure  
87 by Ma et al., E<sub>gate</sub> lacked density and was modeled in two different conformations (Ma et al., 2023)  
88 (**Figure 2 – figure supplement 4C**). Our cryoEM map also reveals a density feature at the S<sub>ext</sub> site,  
89 consistent with a bound Cl<sup>-</sup> ion (**Figure 2C**). The ion at the S<sub>ext</sub> site is stabilized by surrounding  
90 backbone nitrogen atoms, a characteristic feature of CLCs (Dutzler et al., 2003; Picollo et al., 2009;  
91 Feng et al., 2010; Park and MacKinnon, 2018).

92 Two lines of evidence point to the structure representing a closed state, as expected at zero  
93 mV. First, E<sub>gate</sub> physically occupies the S<sub>cen</sub> Cl<sup>-</sup> binding site (**Figures 1A, 2C**), thus blocking the  
94 permeation pathway. Second, we used Caver (Chovancova et al., 2012) to detect pathways through  
95 the protein. A continuous pathway through the protein could only be detected with a very small probe  
96 radius of 0.5 Å. In this case, the route detected follows the canonical Cl<sup>-</sup> transport pathway from the  
97 extracellular side to S<sub>cen</sub>, but then circumnavigates E<sub>gate</sub> to reach the intracellular pathway (**Figure 3A,**  
98 **Video 1**). The pinch point of ~0.7 Å near the E<sub>gate</sub> residue is too narrow for a Cl<sup>-</sup> ion and thus indicates  
99 a closed conformational state. The CLC-2 pathway is constricted compared to that in CLC-1, where the  
100 location of E<sub>gate</sub> in the “out” position permits a wider Cl<sup>-</sup> diffusion pathway (**Figure 3B, Video 2**). Close-  
101 up views of the canonical Cl<sup>-</sup> pathway in CLC-2 and CLC-1 are shown in **Figure 3 – figure**  
102 **supplement 1**. The two lines of evidence just discussed – E<sub>gate</sub> at the S<sub>cen</sub> site and the Caver pinch  
103 point – argue that E<sub>gate</sub> is in the deprotonated state: (1) the location of E<sub>gate</sub> in an anion-binding site is  
104 most consistent with the sidechain being negatively charged; (2) neutralization of E<sub>gate</sub> leads to an

105 open-channel phenotype (Niemeyer et al., 2003; de Santiago et al., 2005), which is incompatible with  
106 the observed pinched-closed pore.

107 At the CLC inner-gate region, near conserved residues Tyr<sub>C</sub> (Y553) and Ser<sub>C</sub> (S162), the  
108 canonical (primary) Cl<sup>-</sup> permeation pathway is similar for CLC-2 and CLC-1 and wider than that seen in  
109 the CLC transporters (**Figure 3 – figure supplement 2A, B, Video 3**). CLC-2 also displays a bifurcated  
110 pore, with a secondary pathway to the intracellular side, distinct from the primary pathway common to  
111 CLC family members. The secondary pathway is shared with CLC-1 but not seen in other CLC  
112 homologs of known structure. While the functional role of this distinctive secondary pore is not yet  
113 known, it is intriguing to note it is located near the region thought to act as a conduit for H<sup>+</sup> in the CLC  
114 transporters (**Figure 3 – figure supplement 2C**).

115

### 116 **Two conformations of the intracellular domain**

117 All eukaryotic CLCs contain a pair of “cystathionine β-synthase” (CBS) domains in their  
118 intracellular C-terminal domain (Jentsch and Pusch, 2018). CBS domains are found in a wide variety of  
119 functionally unrelated protein families, in all kingdoms of life, where they serve to regulate the activity of  
120 the attached protein (Ereno-Orbea et al., 2013; Anashkin et al., 2017). In the CLCs, mutations in or  
121 near the CBS domains alter channel gating and are associated with human disease, including  
122 myotonia, Dent’s disease, Bartter syndrome, osteopetrosis, leukoencephalopathy, retinal degeneration,  
123 lysosomal storage disease, and neurodevelopmental disorders (Estevez et al., 2004; Giorgio et al.,  
124 2017; Jentsch and Pusch, 2018; Guo et al., 2019; Nicoli et al., 2019; Altamura et al., 2020; Ganesello  
125 et al., 2020; Duncan et al., 2021; Zifarelli, 2022; Palmer et al., 2023; Xu et al., 2023). Structurally, the  
126 CLC CBS domains interact across subunits, forming dimers of dimers and thus increasing the overall  
127 interaction area of the homodimer (Feng et al., 2010; Park et al., 2017; Park and MacKinnon, 2018;  
128 Wang et al., 2019; Schrecker et al., 2020). Structural rearrangement of the C-terminal domains is  
129 thought to occur during channel gating (Yamada et al., 2016; Jentsch and Pusch, 2018) and has been  
130 observed spectroscopically (Bykova et al., 2006; Ma et al., 2011), but no rearrangements have yet

131 been observed at high resolution. The physiological relevance of C-terminal domain rearrangements is  
132 suggested by disease-causing mutations that alter channel gating (Estevez et al., 2004; Brenes et al.,  
133 2023).

134 During the 3D classification data processing with a C1 reconstruction (no symmetry imposed),  
135 two distinct conformations were separated from the same CLC-2 dataset (**Figure 2 - figure**  
136 **supplement 2**). Structural comparison of these two classes reveals that they are very similar in the  
137 transmembrane domain, with RMSD of 0.58 Å and 0.42 Å for the two subunits. The main structural  
138 differences occur at the intracellular domain, with one class exhibiting a symmetric arrangement and  
139 the other, asymmetric. These two conformations are named as CLC2-CTDsym and CLC2-CTDasym,  
140 respectively (**Figure 4, Figure 4 - figure supplements 1,2**). In both classes, the CBS domains can be  
141 fit to the density; however residues 645-743 in the CLC-2 C-terminal domain are not resolved and thus  
142 are omitted from the models and from the Q-score calculation (Pintilie et al., 2020) (**Figure 4 – figure**  
143 **supplement 1**). In the asymmetric arrangement (CLC2-CTDasym), one of the CTDs rotates toward the  
144 TM region approximately 35° relative to the conformation in the symmetric structure (**Figure 4B**).  
145 Structural comparison focused on individual CTDs within the two classes reveals low RMSD values (~1  
146 Å), which indicates that the CTD undergoes a rigid body movement to accomplish the conformational  
147 change (**Figure 4C, Video 4**). Molecular dynamics (MD) simulations confirm conformational dynamics  
148 consistent with a domain rotation (**Figure 4 – figure supplement 3**). In both structures, the orientation  
149 of the CTD relative to the membrane is substantially different from that observed in other CLC  
150 structures (**Figure 4 - figure supplement 4**).

151

### 152 **The hairpin structure corresponds to the N-terminal region**

153 Another new feature of the determined CLC-2 structure is a hairpin density blocking the main  
154 Cl<sup>-</sup> pathway on the intracellular side (**Figure 4A**). This feature is not continuous with any other protein  
155 density in the map. In theory, such density could arise from a protein sequence on CLC-2 (from the

156 unstructured N- or C-terminal regions) or from a separate protein carried along in the purification. Given  
157 the history of studies on CLC-2 gating, we first considered the CLC-2 N-terminal region.

158         Shortly after the initial cloning of CLC-2 (Thiemann et al., 1992), experiments on CLC-2  
159 expressed in *Xenopus* oocytes demonstrated that deletion of an 18-residue segment of the N-terminus  
160 yielded a constitutively open channel, lacking the characteristic voltage-dependent gating of CLC-2,  
161 and that transplantation of this segment to the C-terminal domain restored gating (Grunder et al., 1992).  
162 Further, mutation of certain residues in the transmembrane domain (at a putative “receptor” site for the  
163 N-terminal blockade) also yielded an open-channel phenotype (Jordt and Jentsch, 1997). Based on  
164 these results, it was argued that CLC-2 has a “ball-and-chain” type gating mechanism reminiscent of  
165 that occurring in the *Shaker* potassium channel (Zagotta et al., 1990). However, experiments performed  
166 using the inside-out patch clamp configuration (Pusch et al., 1999) or using whole-cell recording with  
167 CLC-2 expressed in mammalian cells (Varela et al., 2002) failed to recapitulate the gating phenotype  
168 and called into question a ball-and-chain mechanism. Thus, while mutations in the N-terminus of CLC-2  
169 influence gating, the precise mechanism-of-action has been uncertain.

170         Our cryoEM map allowed continuous modeling of the CLC-2 sequence starting from the first TM  
171 helix (residue 88). The lack of sufficient density for modeling residues 1-87 suggests that the N terminal  
172 cytoplasmic region of CLC-2 is intrinsically disordered. However, our observation of a resolvable hairpin  
173 density at the intracellular pore, together with the previous hypothesis of N-terminal ball-and-chain  
174 gating for CLC-2, prompted us to consider whether the hairpin density corresponds to N-terminal  
175 residues. We tested several candidate fragments from the CLC-2 N-terminal region and found that the  
176 hairpin density fits perfectly with residues corresponding to 14-28 (**Figure 5A**). Inspection of the Q-  
177 score validation plot for these residues shows they have higher values than the Q-score expected for  
178 the corresponding resolution (**Figure 5B**), which indicates reliable model building at this resolution  
179 (Pintilie et al., 2020). In contrast, the best-fitting peptide from disordered regions of the C-terminal  
180 cytoplasmic region yielded poorer Q scores, generally lower than the Q-score expected for the  
181 corresponding resolution (**Figure 5 – figure supplement 1**). The N-terminal residues corresponding to

182 the hairpin peptide are conserved throughout the mammalian CLC-2 homologs and partially conserved  
183 in *Drosophila* CLC-2 (**Figure 5 - figure supplement 2**).

184 Interestingly, the presence of the N-terminal hairpin is associated with conformational changes  
185 in the CTD and TM domains. In CLC2-CTDsym, N-terminal density was observed on both subunits. In  
186 CLC2-CTDasym, only the subunit whose CTD adopts the “symmetric” orientation (seen in CLC2-  
187 CTDSym) contains the hairpin density; in the subunit with the rotated CTD, no hairpin density is  
188 observed (**Figure 4, Figure 5A**). Along with the absence of hairpin density, the subunit with the rotated  
189 CTD exhibits a difference in the linker connecting transmembrane helices J and K, which is poorly  
190 resolved and insufficient for model building. In contrast, the subunits with the hairpin density contain  
191 reliable density in the JK-linker region, allowing confident modeling of an alpha helix (“JK-helix”, **Figure**  
192 **5A**). This observation suggests that the JK-helix stabilizes the N-terminal hairpin peptide. Indeed,  
193 residues on the JK-helix interact directly with residues at the peptide’s hairpin turn (**Figure 5C**).  
194 Interactions with other regions in the TM domain (near helices C, D, J, and R) appear to further stabilize  
195 the hairpin in its binding site. In addition, the negative surface potential of the hairpin likely contributes  
196 to its interaction with the positive TM domain (**Figure 5 – figure supplement 3; Video 5**). MD  
197 simulations help separately validate the assignment and stability of the hairpin: in MD simulations  
198 initiated from the structure, we found that the N-terminus remained tightly associated with the channel  
199 in all simulations (**Figure 5 – figure supplement 4**).

200

### 201 **Functional support for pore block by the N-terminal hairpin structure**

202 The hairpin structure appears to directly block the pore (**Figure 5 – figure supplement 5**). To  
203 evaluate the potential functional effect of pore block by the N-terminal hairpin, we performed whole-cell  
204 patch clamp recording on CLC-2, both WT and a deletion mutant lacking the hairpin residues (“Delta-  
205 N”), expressed in CHO cells. Delta-N CLC-2 exhibits currents that display less rectification and faster  
206 activation kinetics than WT CLC-2 (**Figure 6A-B, Figure 6 – figure supplement 1**). This gating  
207 phenotype is intermediate between the non-rectifying phenotype of N-deletion constructs from whole-

208 cell recordings in oocytes (Jordt and Jentsch, 1997) and the highly rectifying phenotype from whole-cell  
209 recordings in HEK 293 cells (Varela et al., 2002). The Discussion section addresses the variability  
210 observed in CLC-2 current recordings. As was reported for N-deletion currents in oocytes, our delta-N  
211 currents are substantially larger than WT currents, ~6-fold on average when identical transfection  
212 conditions are used (**Figure 6C**). This difference cannot be explained by a difference in plasma-  
213 membrane expression, as surface biotinylation experiments revealed that expression levels of the two  
214 constructs are within 30% of one another (**Figure 6D, E**).

215 Strikingly, WT but not delta-N CLC-2 currents “run up” during recording sessions. In patch-  
216 clamp recording experiments, the term “run-up” describes a progressive increase in current that occurs  
217 after the initial measurement. To quantify CLC-2 run-up, we developed the following protocol: (1) on  
218 acquisition of whole-cell recording mode, an initial voltage-family of currents was recorded, as in **Figure**  
219 **6A**; (2) from a holding potential of 0 mV, a single 1-s test pulse to -100 mV was repeated every 5  
220 seconds to monitor time-dependent changes in current amplitude over 5 minutes, after which a second  
221 voltage-family of currents was recorded; (3) 300 nM AK-42 was added to selectively block all CLC-2  
222 current (Koster et al., 2020), and the steady state inhibition current was used for leak subtraction. In  
223 contrast to chloride-channel inhibitors historically used in electrophysiological experiments (Sepela and  
224 Sack, 2018), AK-42 is potent and highly selective for CLC-2 over other anion channels (Koster et al.,  
225 2020). Representative current traces and summary data for this set of experiments are shown in **Figure**  
226 **6F, G**; individual I-V traces are shown in **Figure 6 – figure supplement 1**. The increase in WT but not  
227 delta-N CLC-2 currents over time is consistent with an “unblocking” of the pore by release of the N-  
228 terminal hairpin peptide.

229 The increase in WT currents is accompanied by an apparent decrease in channel rectification,  
230 towards the level displayed by Delta-N CLC-2. WT CLC-2 currents recorded in heterologous and native  
231 expression systems are generally highly inwardly rectifying. Analogous to a rectifier in an electrical  
232 circuit, WT CLC-2 acts as a directional current valve, allowing much larger absolute currents to flow at  
233 negative membrane potentials compared to positive ones. At the beginning of each recording, our WT



234 CLC-2 currents display such inward rectification, but this characteristic appears to diminish during five  
235 minutes of repeated voltage pulsing to -100 mV, as substantial currents at positive voltages appear. For  
236 the experiment shown in **Figure 6F**, the steady-state current at +80 mV increases from 161 pA to 902  
237 pA, almost six-fold, compared to a 2.4-fold increase at -100 mV. This observation is surprising because  
238 WT CLC-2 has been characterized as passing little to no current at positive voltages (Park et al., 1998;  
239 Arreola et al., 2002). We initially considered that the increase in current at +80 mV could be due to the  
240 patch-clamp seal becoming leaky over time or that a background channel is being activated; however,  
241 such 'leak' currents would not be expected to be blocked by the small molecule inhibitor AK-42, which  
242 is highly selective for CLC-2 over all other CLCs and anion channels (Koster et al., 2020). AK-42 block  
243 of the augmented +80 mV currents seen at the end of each WT CLC-2 recording supports the idea that  
244 the hairpin peptide may contribute to the inward rectification of CLC-2 (**Figure 6F, Figure 6 – figure**  
245 **supplement 2**).

246

#### 247 **AK-42 bound structure**

248 AK-42's selectivity empowered our biophysical studies of CLC-2 and will also be invaluable for  
249 studies of CLC-2's physiological function. We determined the structure of CLC-2 in complex with AK-42  
250 (**Figure 7**). While the TM domain could be resolved to 2.7 Å, the CTD exhibited poor density compared  
251 to the apo sample and did not allow us to confidently model the CTD when masking the whole protein  
252 for refinement. To improve the density quality, we masked the CTD only for refinement; this masking  
253 provided an acceptable density map at 4 Å and allowed us to confidently dock the CTD from apo  
254 structure (**Figure 7 – figure supplements 1-4**).

255 Like the apo CLC-2 structure, the TM domain of CLC2-TM-AK42 is well-resolved with clear  
256 densities for AK-42 and for CLC-2 sidechains, including the E<sub>gate</sub> sidechain (**Figure 7 – figure**  
257 **supplements 5,6**). The overall density for CLC2-TM-AK42 is very similar to that observed in apo CLC-  
258 2, but with an extra density that fits very well to the AK-42 molecule (**Figure 7B, Video 6**). Residues in  
259 the AK-42 binding pocket exhibit little conformational change between the apo and AK-42 bound CLC-2



260 structures. The exception is residue M460, which moves  $\sim 3$  Å to avoid a clash with AK-42's phenyl ring  
261 (**Figure 7 - figure supplement 7**). Located at the extracellular side of Cl<sup>-</sup> pathway, the bound AK-42  
262 appears to directly block Cl<sup>-</sup> permeation (**Figure 7C**). This AK-42 binding pocket is the same as  
263 observed in the docking prediction we previously made using a CLC-2 homology model (Koster et al.,  
264 2020). In that docking study, the top docking poses varied in detail, and therefore the specific  
265 interactions were not certain, but the general position of the binding site is confirmed by our cryoEM  
266 structure. Two conformations were found to fit the density well with the carboxyl group on opposite  
267 sides. They were tested using the Quantum Mechanical Restraints (QMR) method (Liebschner et al.,  
268 2023); one had significantly lower energy ( $\sim 17$  kcal/mol) and strain on the ligand (10.2 kcal/mol),  
269 considering the ligand and nearby residues only. For the lower energy conformation, the Q-scores of  
270 AK-42 in the map are 0.74 and 0.76 in the two subunits, respectively. Both are higher than the  
271 expected Q-score at this resolution (0.64), which indicates a good fit of AK-42 to the cryoEM density  
272 (Pintilie et al., 2020). A similar AK-42 binding pose was observed in another recently published  
273 structure of CLC-2 (Ma et al., 2023). The RMSD between our CLC2-TM-AK42 structure and that of Ma  
274 et al. is 0.655 Å, and the RMSD between the apo TM structures is 0.756 Å .

275 In the binding site, AK-42's phenyl ring nestles into a hydrophobic pocket lined by F306, F463,  
276 F459, M460 and L524 (**Figure 7B**). The carboxyl group of AK-42 forms hydrogen bonds with the side  
277 chain of S392 and backbone of K394 (**Figure 7B**). These polar interactions are consistent with  
278 mutagenesis data. At 30 nM AK-42, inhibition of S392A is reduced  $\sim 50\%$  compared to WT, consistent  
279 with disruption of the observed hydrogen bond, while inhibition of K394A is not significantly different  
280 from WT, consistent with a backbone rather than a side-chain interaction (Koster et al., 2020; Ma et al.,  
281 2023). A third hydrogen bond – between K204 and the pyridine nitrogen of AK-42 – also contributes to  
282 AK-42's stability in the binding pocket. A pivotal role for the pyridine nitrogen was discovered during the  
283 development of AK-42, where it was found that inhibitor potency is increased by over two orders of  
284 magnitude by addition of a nitrogen at this position but not by addition of a nitrogen at any other  
285 position in the ring (Koster et al., 2020). The interaction of this pyridine nitrogen with K204 is supported

286 by mutagenesis data, which shows that inhibition of K204M and K204R (K210M and K210R in rat CLC-  
287 2) is reduced ~3-fold compared to WT (Koster et al., 2020; Ma et al., 2023). The distance between the  
288 nitrogen atoms on K204 and AK-42 is 3.6 Å, within acceptable hydrogen bond distance, while the  
289 distances between K204 and any other atoms on AK-42 are too far to allow hydrogen bond formation.

290 Notably, density corresponding to the N-terminal hairpin structure is not seen in the AK-42  
291 bound structure. After intensive 3D classification, only very minimal hairpin density was observed in a  
292 few classes. It thus appears that the majority of AK-42 bound CLC-2 particles have a flexible N-  
293 terminus that is not blocking the Cl<sup>-</sup> pathway. There is no obvious explanation for this difference  
294 compared to the apo structure. The orientation of the CTD in the AK-42 bound structure is the same as  
295 observed in the apo structure that shows N-terminal hairpin binding; the density for the J-K helix is  
296 weaker than in the apo dataset, but still sufficient to allow modeling of the helix. The TM regions also  
297 appear similar. To scrutinize for subtle conformational changes, we calculated a distance difference  
298 matrix (Nishikawa, 1972) comparing CLC2-TM and AK-42 bound CLC-2 (**Figure 7 – figure**  
299 **supplement 8**). The minor changes observed do not readily suggest a structure-based hypothesis for  
300 the observed difference in N-terminus. It could be that AK-42 inhibits dynamics that are essential for  
301 hairpin peptide binding.

302

## 303 **DISCUSSION**

304 Our CLC-2 channel structures display quintessential CLC characteristics, including a  
305 homodimeric arrangement of subunits, transmembrane domains composed of 18 helical segments, and  
306 conserved residues surrounding central anion-binding sites S<sub>ext</sub> and S<sub>cen</sub> (Jentsch and Pusch, 2018). At  
307 2.5 Å resolution, we observe clear density for critical features, including a Cl<sup>-</sup> ion at S<sub>ext</sub> and the E<sub>gate</sub>  
308 residue at S<sub>cen</sub> (**Figure 2C**). In this position, E<sub>gate</sub> blocks the pore, generating a closed conformational  
309 state – as expected for CLC-2 at 0 mV (**Figure 1**).

310

## 311 **AK-42 binding site and inhibition potency**

312 A distinctive feature of AK-42—unique amongst CLC inhibitors—is its high selectivity for CLC-2  
313 versus other channels, transporters, and receptors (Koster et al., 2020). The  $IC_{50}$  for inhibition of CLC-2  
314 by AK-42 (17 nM) is more than four orders of magnitude lower than the  $IC_{50}$  for inhibition of CLC-1,  
315 CLC-2's closest homolog. CLC-1 and CLC-2 are 50% identical overall, and within the AK-42 binding  
316 site only five residues are different (**Figure 7 – figure supplement 9**). Structural comparison of CLC-1  
317 (PDB ID:6coy) with CLC2-AK42 reveals that these five residues (I112 (S139), S392 (M419), Q393  
318 (P420), K394 (R421), and L397 (I424)) exhibit only relatively minor differences in backbone  
319 conformation. While the S392 side chain contributes to a hydrogen-bond interaction with AK-42 (**Figure**  
320 **7B**), which M419 in CLC-1 cannot provide, this interaction alone cannot explain the four orders of  
321 magnitude difference in AK-42 potency. Indeed, the mutation S392A reduces inhibition by 30 nM AK-42  
322 only ~3-fold (Ma et al., 2023). Similarly, Q393P (Q399P in rat CLC-2) reduces inhibition by less than  
323 five-fold (Koster et al., 2020; Ma et al., 2023). A steric clash between F279 (F252 in CLC-2) and the  
324 benzyl substituent in AK-42 may also contribute to the lack of potency of AK-42 towards CLC-1 (**Figure**  
325 **7 - figure supplement 9**). In CLC-2, this same residue (F252) is shifted away from the binding site,  
326 opening a sub-pocket that the benzyl group occupies. This difference is not simply induced by AK-42  
327 binding, as F252 is also shifted away from the binding site in the CLC-2 apo structure. In the structure-  
328 activity relationship studies used to develop AK-42, the benzyl substituent increased selectivity  
329 approximately 5-fold (Koster et al., 2020), thus supporting the significance of this interaction to  
330 selectivity. Unfortunately, this hypothesis cannot be tested through mutagenesis experiments due to the  
331 extremely low expression of F252 mutants (Ma et al., 2023).

332 The pathway from the extracellular solution appears sufficiently wide for AK-42 to worm its way  
333 into the binding site (**Figure 7C**). It is not yet known whether this pathway becomes wider in the CLC-2  
334 open state. Intriguingly, the lack of density for the hairpin peptide in the AK-42-bound structure  
335 suggests that hairpin and AK-42 binding may be mutually exclusive. Studies to evaluate state-  
336 dependence of AK-42 inhibition and of hairpin block will be valuable for understanding CLC-2  
337 conformational change and gating dynamics.

338

339 **E<sub>gate</sub> conformation**

340 CLC-2 is the first CLC channel homolog to be seen in a closed conformational state. While it  
341 was expected that E<sub>gate</sub> would localize to the Cl<sup>-</sup>-permeation pathway in the closed conformational  
342 state, it was not certain whether the S<sub>ext</sub> or S<sub>cen</sub> site would be preferred. The structure of CLC-1  
343 provides an argument that S<sub>ext</sub> might be preferred. In CLC-1, anion density is observed at S<sub>ext</sub> but not at  
344 S<sub>cen</sub> (Park and MacKinnon, 2018). It was hypothesized that the lack of density at S<sub>cen</sub> in CLC-1 may  
345 reflect a reduced anion-binding affinity that contributes to increased Cl<sup>-</sup> conduction (higher Cl<sup>-</sup>  
346 throughput) by the CLC channels compared to the transporters (Park and MacKinnon, 2018), as all  
347 structures of WT CLC transporters show anion density (either Cl<sup>-</sup> or E<sub>gate</sub>) at both S<sub>ext</sub> and S<sub>cen</sub> (Dutzler  
348 et al., 2003; Chavan et al., 2020; Schrecker et al., 2020). If true for all channels, one might expect E<sub>gate</sub>  
349 in CLC-2 to occupy S<sub>ext</sub> rather than S<sub>cen</sub> in the closed state. However, we do not observe this  
350 occupancy, and therefore the decreased anion affinity at S<sub>cen</sub> is not the universal reason for increased  
351 Cl<sup>-</sup> conduction in CLC channels relative to the transporters. Instead, our CLC-2 structure is consistent  
352 with the predictions made by Arreola and colleagues, who used homology modeling in concert with  
353 detailed electrophysiological analyses to conclude that the CLC-2 gate is formed by the E<sub>gate</sub>-Tyr<sub>C</sub> pair  
354 at S<sub>cen</sub> (De Jesus-Perez et al., 2021). Additional experiments, to directly measure anion affinity and to  
355 determine structures of CLC-2 and CLC-1 in both open and closed conformations are needed to better  
356 understand these channels' similarities and differences.

357

358 **CTD conformation**

359 CLC-2 is also the first CLC in which two conformations of the CTD are observed. While many  
360 previous studies indicate that conformational change of the CTDs plays a critical role in CLC gating  
361 (Jentsch and Pusch, 2018; Grieschat et al., 2020), the mechanistic details are currently fuzzy. Unlike  
362 other CLC variants, CLC-2 can still conduct Cl<sup>-</sup> when its CTD is removed; however, the modified gating  
363 kinetics of this mutant do suggest a role of the CTD in regulating channel function (Garcia-Olivares et

364 al., 2008). The impact of mutations in various regions of the CLC-2 CTD further supports its role in  
365 gating (Yusef et al., 2006; Paul et al., 2007; Stolting et al., 2013; Giorgio et al., 2017), as do the effects  
366 of ATP binding on channel kinetics (Saint-Martin et al., 2009; Stolting et al., 2013). While we do not see  
367 ATP bound in our structure (none was added to the protein preparation), the binding-site region  
368 overlaps reasonably well with the structure of the ATP-bound CLC-5 CTD (**Figure 4 – figure**  
369 **supplement 5**). The physiological significance of an intact CTD is underscored by CTD mutations and  
370 truncations of CLC-2 that occur in human leukoencephalopathy and retinal degeneration (Giorgio et al.,  
371 2017; Guo et al., 2019; Xu et al., 2023). It is likely that the structural rearrangement we observe  
372 strongly influences channel gating: the CTD upward hinge rotation restricts access to the hairpin-  
373 blocking site and substantially changes CTD interactions with the transmembrane domain.

374

### 375 **Ball and Chain Gating**

376 Steric block of the Cl<sup>-</sup> permeation pathway by the N-terminal hairpin peptide (**Figure 5**)  
377 rekindles the hypothesis of a “ball-and-chain”-type gating mechanism for CLC-2, first proposed over 30  
378 years ago (Grunder et al., 1992). In those studies, residue Q19 in the N-terminal hairpin, which  
379 hydrogen bonds to Q153 in the TM domain (**Figure 5C**), was identified as a residue critical to the “ball”  
380 blocking mechanism (Grunder et al., 1992). In follow-up studies, it was concluded that the “receptor”  
381 site on the TM domain is formed by residues in a stretch from 342-351 (Jordt and Jentsch, 1997) on  
382 helix J, which also forms part of the hairpin-docking site (**Figure 5C, Figure 5 – figure supplement**  
383 **6A**). The hairpin-TM interface identified in our structure also exquisitely harmonizes with results from  
384 studying human mutations associated with primary aldosteronism. These gain-of-function mutations,  
385 which map squarely onto the peptide hairpin and surrounding TM region (**Figure 5 – figure**  
386 **supplement 6B**), cause increases in CLC-2 currents that depolarize the glomerulosal membrane  
387 potential thus leading to disease (Fernandes-Rosa et al., 2018; Scholl et al., 2018).

388 Our electrophysiology results also support a ball-and-chain gating mechanism. First, we  
389 demonstrate that the increase in current in hairpin-deleted channels reflects an increase in channel

390 activity rather than an increase in surface expression (**Figure 6D,E**), consistent with loss of a channel-  
391 closing mechanism. Second, we show that WT but not delta-N CLC-2 currents increase over time  
392 (**Figure 6F,G**), consistent with relief of the hairpin block. Importantly, our use of the selective inhibitor  
393 AK-42 (Koster et al., 2020) provides confidence that the current increase is specific to CLC-2 and not a  
394 result of leak or a run-up of other Cl<sup>-</sup> currents, which notoriously lurk in all mammalian cells and can  
395 confound interpretation of experimental results. In the context of our structure and the mutagenesis  
396 studies discussed above, our electrophysiological results fortify a ball-and-chain model for CLC-2  
397 gating.

398

### 399 **Ball-and-chain gating as a potential mechanism for CLC-2 current variability**

400 How do we explain the ostensible discrepancy between our results, which support a ball-and-  
401 chain model, and the previously published results that were used to argue against a ball-and-chain type  
402 gating mechanism? We think the discrepancy is not as dire as it originally seemed. The previous  
403 discrepancy is as follows. In studies of an N-terminal CLC-2 deletion mutant in HEK 293 cells, Varela et  
404 al. observed currents that differed depending on whether whole-cell or nystatin-perforated patch clamp  
405 recording was used: with whole-cell recording, deletion-mutant currents displayed rectification similar to  
406 WT CLC-2 but with much faster kinetics; with perforated-patch recording, currents were voltage  
407 independent and non-rectifying (Varela et al., 2002). At the time, this difference was interpreted to  
408 mean that the open-channel phenotype (and therefore ball-and-chain gating) was artifactual, due to a  
409 diffusible intracellular factor binding to the N-terminal deletion channel, but not the WT channel, locking  
410 it open in the perforated-patch recording configuration (but diffusing away in whole-cell recording  
411 experiments). However, Varela et al. also aptly pointed out that mutagenesis experiments did support a  
412 role for the CLC-2 N-terminus in channel gating. Further, they noted that the different results between  
413 their two recording configurations could be due to differences of physiological relevance, such as  
414 osmotic forces and/or channel-cytoskeleton interactions (Grunder et al., 1992; Ahmed et al., 2000).  
415 Such factors could also explain the differences between our whole-cell recordings and those of Varela

416 et al. We note that our Delta-N currents observed with whole-cell recording (**Figure 6 – figure**  
417 **supplement 1**) are similar to currents displayed by the aldosteronism peptide-hairpin mutant G24D in  
418 perforated-patch clamp recordings (Goppner et al., 2019), supporting that our use of whole-cell  
419 recording is not introducing an artifact.

420 We hypothesize that sensitivity of ball-and-chain gating to physiological variables may underlie  
421 the tremendous variation in kinetics and voltage-dependence observed amongst recordings of natively  
422 expressed CLC-2 (Bosl et al., 2001; Jentsch and Pusch, 2018). Such variation could arise from  
423 differences in one or more of the factors known to modulate CLC-2 gating – osmotic forces,  
424 transmembrane voltage, ATP, phosphorylation, or interactions with the cytoskeleton or other cellular  
425 proteins (Nighot et al., 2017; Jentsch and Pusch, 2018; Okamoto et al., 2019) – and could be further  
426 modulated by the expression of N-terminal splice variants (Furukawa et al., 1995; Cid et al., 2000). We  
427 propose that mechanistic studies of the CLC-2 gating run-up we report here (**Figure 6F**) will be  
428 valuable to guide studies on the variability of CLC-2 currents in native systems and how it relates to  
429 ball-and-chain gating.

430

### 431 **Revised framework for CLC-2 gating**

432 The established framework for CLC channel gating (Jentsch and Pusch, 2018) is based on  
433 pioneering investigations on the *Torpedo* homolog CLC-0. These investigations identified two separate  
434 mechanisms responsible for channel gating (Miller, 1982). The first gating mechanism, referred to as  
435 “fast” or “protopore” gating, opens and closes each pore of the homodimer independently on a  
436 millisecond timescale.  $E_{\text{gate}}$  (**Figure 1**) plays a central role in this protopore gating (Dutzler et al., 2003),  
437 with voltage-dependence arising from interactions between  $E_{\text{gate}}$  and ions in the pore (Pusch et al.,  
438 1995). The second gating mechanism, referred to as “slow” or “common” gating, is orders of magnitude  
439 slower (seconds to tens-of-seconds timescale) than “fast” gating and operates in a highly cooperative  
440 manner to open and close both CLC-0 pores simultaneously. The simultaneous opening/closing of  
441 pores that are separated by >30 Angstrom, together with the exceptionally high temperature



442 dependence of slow gating (Pusch et al., 1997), suggests that large structural rearrangements are  
443 involved. Indeed, large movements of the CTDs were observed in a fluorescence resonance energy  
444 transfer study of CLC-0 slow gating (Bykova et al., 2006).

445 In CLC-2, electrophysiological studies of WT and mutant channels were used to illustrate that  
446 CLC-2 has two gating mechanisms (Zuniga et al., 2004; de Santiago et al., 2005; Yusef et al., 2006).  
447 However, it remains uncertain as to whether these two mechanisms are analogous to the fast protopore  
448 and slow common gating mechanisms observed in CLC-0. On one hand, studies demonstrating that  
449 interactions between  $E_{\text{gate}}$  and ions in the pore play a critical role in gating support that CLC-2 has a  
450 “fast” protopore gating mechanism (Niemeyer et al., 2003; Niemeyer et al., 2009; Sanchez-Rodriguez  
451 et al., 2010; Sanchez-Rodriguez et al., 2012; De Jesus-Perez et al., 2016). On the other hand, there  
452 are substantial differences between CLC-2’s “slow” gating mode and CLC-0’s common gating in terms  
453 of kinetics and temperature dependence. Moreover, unlike CLC-0 (Lin et al., 1999), CLC-2 slow and  
454 fast gating cannot be separately affected by mutation (Zuniga et al., 2004; de Santiago et al., 2005;  
455 Yusef et al., 2006; De Jesus-Perez et al., 2021). Finally, in contrast to CLC-0, it has not been  
456 demonstrated that the “slow” gate in CLC-2 corresponds to a common gating process operating on both  
457 pores simultaneously.

458 Our results strongly motivate a revised framework for understanding CLC-2 protopore gating. At  
459 least two events are needed to open each protopore - relief of block by the N-terminal hairpin (ball and  
460 chain gating) and  $E_{\text{gate}}$  movement (**Figure 8**). A key aspect of our revised framework is that ball and  
461 chain gating is coupled to CTD conformational change: close examination of the state with the CTD  
462 rotated (**Figure 4A**) reveals that the hairpin can’t access its pore-blocking site in this state. Thus, CTD  
463 rotation facilitates hairpin release and channel opening. This structural model is consistent with  
464 electrophysiological studies showing that removal of the CTD speeds CLC-2 activation and deactivation  
465 kinetics (Garcia-Olivares et al., 2008). In contrast to CLC-0, where movements in the CTD have been  
466 linked to the highly cooperative conformational change involved in common gating (Estevez et al.,



467 2004; Bykova et al., 2006), our structures illustrate that in CLC-2 the CTDs can move independently of  
468 one another.

469 CLC-2 gating is more complex than depicted in our simple cartoon, and many questions remain.  
470 First, prior results suggest that CLC-2 “slow” gating involves conformational change beyond the  $E_{gate}$   
471 and hairpin/CTD motions depicted in our model. Even when  $E_{gate}$  is neutralized, CLC-2 retains some  
472 voltage-dependent gating (Niemeyer et al., 2003), indicating a conformational change beyond  $E_{gate}$ .  
473 This additional voltage-dependent gating cannot be solely due to N-terminal ball and chain gating, since  
474 channels with N-terminal deletions retain biexponential voltage dependence as is seen in the wild type  
475 channels (Varela et al., 2002). Second, electrophysiological studies indicate that CLC-2 has at least two  
476 open states (de Santiago et al., 2005), but the physical basis for these different open states is  
477 unknown. These points strongly motivate studies to elucidate additional conformational changes in  
478 CLC-2. Whether such changes include a highly cooperative common gating mechanism will require  
479 functional studies to complement structures, ideally with visualization of gating in single-channel  
480 recordings. Augmenting complexity in understanding CLC-2 is our observation that channel rectification  
481 changes upon N-terminal deletion or ball and chain gating (**Figure 6F; Figure 6 – Figure supplement**  
482 **2**): the molecular underpinnings of this change in rectification are wholly unknown. Addressing all these  
483 questions will be important for understanding CLC-2’s diverse functional characteristics and  
484 physiological roles in various tissues and cells (Bosl et al., 2001; Jentsch and Pusch, 2018).

485

## 486 **Summary**

487 The structures and electrophysiological data presented here reveal a ball-and-chain mechanism  
488 involved in CLC-2 gating and offer a framework for understanding CLC-2’s multiple gating mechanisms.  
489 In addition, the structures illuminate details for molecular recognition by the selective inhibitor AK-42,  
490 the first and currently only known small-molecule modulator that is both potent and selective for a CLC  
491 family member.

492

493 **METHODS**

494 **Molecular biology and AK-42 synthesis**

495 Full-length human CLC-2 (Uniprot ID: P51788) was fused to a C-terminal twin-strep tag with a  
496 linker of 5'- TCGAATTCTTTGGAAGTTTTGTTTCAAGGTCCAAGTCTGCTGCCGCCGCT-3' containing a  
497 HRV 3C protease cleavage sequence (underlined). This human C-terminal twin-strep-tagged CLC-2  
498 fusion construct was cloned into a modified pFastBac vector that contains a CMV promoter for protein  
499 expression in mammalian cells (Goehring et al., 2014; Park et al., 2017). For electrophysiology and cell  
500 surface protein biotinylation/isolation experiments, the twin-strep tag was replaced by a EGFP tag. A C-  
501 terminal GFP tag was previously shown to have no significant effect on CLC-2 channel kinetics or  
502 voltage dependence (Park, Arreola 1998). In the N-terminal deletion CLC-2 (delta-N), residues 14-27  
503 (ALQYEQTLMYGRYT) were removed from full-length (WT) CLC-2.

504 AK-42 was synthesized and quantified as previously described (Koster et al., 2020)

505

506 **Protein expression/ purification**

507 The full-length CLC-2 construct was transformed to DH10Bac competent cells (Invitrogen) to  
508 isolate baculovirus bacmid. The bacmid was transfected to sf9 cells using Cellfectin-II (Invitrogen) to  
509 produce baculovirus. The baculovirus were then further amplified twice in sf9 cells. The protein was  
510 expressed with HEK293 GnTI<sup>-</sup> cells with the amplified baculovirus. HEK293 GnTI<sup>-</sup> cells were cultured in  
511 Freestyle 293 medium (Invitrogen) supplemented with 2% FBS on a shaker at 37 °C in the presence of  
512 8% CO<sub>2</sub> to a density of 3 × 10<sup>6</sup> cells per ml, then infected with 5% v/v baculovirus. After culturing for  
513 another 8-16 hours, sodium butyrate was added at final concentration of 10 mM, then further expressed  
514 for 48 hours at 37 °C before harvest. Cells were pelleted and stored at -80 °C.

515 Frozen cell pellets were resuspended in resuspension buffer containing 50 mM Hepes, pH 7.5,  
516 300 mM NaCl, 1 mM dithiothreitol (DTT), 1 mM ethylenediaminetetraacetic acid (EDTA), and 1  
517 protease inhibitor cocktail tablet (MedChem Express), then briefly lysis cells with dounce homogenizer  
518 for 10-15 times. Cellular debris were collected by centrifugation at 18k rpm for 30 minutes at 4 °C, and

519 then resuspended with resuspension buffer supplemented with 1% lauryl maltose neopentyl glycol  
520 (LMNG) and 0.1% cholesteryl semisuccinate (CHS). After extraction for 2 hours, the lysate was  
521 centrifuged at 18k rpm for 40 minutes at 4 °C. The clarified lysate was incubated with 1 mL of strep-  
522 Tacin XT high-capacity resin (IBA) for 2 hours at 4 °C. Resin was washed with wash buffer containing  
523 50 mM Hepes, pH 7.5, 300 mM NaCl, 1 mM DTT, 1 mM EDTA, 0.02% LMNG, and 0.002% CHS.  
524 Purified protein was released from resin with 50 µg HRV 3C protease and incubated at 4 °C for  
525 overnight. The retrieved protein was concentrated to 0.5 ml with Amicon Ultra (50 kDa cutoff, EMD  
526 Millipore) and followed by size-exclusion chromatography (SEC) using a superdex 200 Increased  
527 10/300 chromatography column on an AKTA Purifier 10 FPLC system (GE Healthcare) with buffer  
528 containing 20 mM Hepes, 150 mM NaCl, 1 mM DTT, 0.5 mM EDTA, 0.002% LMNG, and 0.0002%  
529 CHS. Protein fractions were pooled, concentrated with Amicon Ultra (50 kDa cutoff, EMD Millipore) to  
530 ~5 mg/ml, and immediately used for cryoEM grid preparation.

531 For CLC-2 and AK-42 complex, AK-42 was first dissolved in DMSO to 45 mM, then further  
532 diluted with CLC-2 SEC buffer to 2 mM and mixed with purified and concentrated CLC-2 protein (2.9  
533 mg/mL) to make final solution with CLC-2/AK-42 at a molar ratio of 1:10 (20 µM CLC-2 with 200 µM  
534 AK-42). The mixture was incubated at 4 °C for 3 hours and then used for cryoEM grid preparation.

535

### 536 **CryoEM data collection and processing**

537 Three microliters of the purified CLC-2 or CLC-2/AK-42 mixture was applied to glow-discharged  
538 copper Quantifoil R1.2/1.3 or R2/1 holey carbon grids (Quantifoil). Grids were incubated for 15 s, then  
539 blotted for 4s or 6s at 100% humidity, then plunge-frozen in liquid-nitrogen-cooled liquid ethane using a  
540 Vitrobot Mark IV (Thermo Fisher Scientific) at 4 °C.

541 The grids were imaged on a Titan Krios electron microscope (Thermo Fisher) operated at 300  
542 kV with a Falcon 4 direct electron detector (Thermo Fisher Scientific) and SelectrisX energy filter  
543 (Thermo Fisher Scientific). Micrographs were recorded at a magnification of 130,000 × (pixel size of  
544 0.946 Å per pixel) with EPU software (Thermo Fisher Scientific) Each image was composed of 40

545 individual frames with total cumulative dose of 50 e<sup>-</sup> per Å<sup>2</sup>. For CLC-2 dataset, images were collected  
546 with an exposure time of 7.5 seconds and a dose rate of 6.7 e<sup>-</sup> per second per Å<sup>2</sup> (OR 6.0 e<sup>-</sup> per  
547 second per pixel). For CLC-2/AK-42 dataset, images were collected with an exposure time of 5.6  
548 seconds and a dose rate of 8.9 e<sup>-</sup> per second per Å<sup>2</sup> (OR 8.0 e<sup>-</sup> per second per pixel). Defocus values  
549 were set from -1.0 μm to -2.0 μm.

550 CryoEM data processing was performed mainly using CryoSPARC 3.2 (Structura Biotechnology  
551 Inc), except those mentioned specifically. For CLC-2 sample, a total of 14,198 movie stacks were  
552 subjected to motion correction. The contrast-transfer function (CTF) parameters were estimated using  
553 patch CTF. Initially, a total of 56,091 particles were auto-picked and subjected to reference-free 2D  
554 classification. A total of 7 class averages were selected as templated for automated particle picking. A  
555 total of 4,999,780 particles were auto-picked and extracted with a box size of 256 pixels. The extracted  
556 particles were then subjected to 2D classification to remove ice, contaminants, and aggregates. The  
557 following ab initio reconstruction and 3D refinement (for all structures presented in this paper) are all  
558 performed with C1 symmetry (no symmetry imposed). The cleared-up classes were used for ab initio  
559 reconstruction with two classes. These models were used as reference for a heterogenous refinement  
560 with no symmetry imposed. The best class from heterogenous refinement which contained 2,415,222  
561 particles were subjected to non-uniform 3D refinements, followed by local 3D refinements, yielding final  
562 CLC2-TM map at 2.46 Å, as determined by the gold-standard measure of Fourier shell correlation  
563 (FSC) using a cut-off of 0.143. Local resolution was estimated with relion 3.1. To further improve  
564 density map of CTD, the selected 2,415,222 particles were divided into 10 subsets for 3D classification  
565 in relion 3.1. A reference map for 3D classification was generated by the 3D ab initio model in  
566 CryoSparc. Two of the classes, containing 56,580 and 39,272 particles respectively, showed distinct  
567 CTD features and were used for further non-uniform 3D refinement and local 3D refinements,  
568 separately. The resolution was determined by Fourier shell correlation (FSC) using a cut-off of 0.143 at  
569 2.75 Å and 2.76 Å, respectively.

570 Processing for CLC2-AK42 sample was executed similarly as described above. In brief, a total  
571 of 14,300 movie stacks were motion corrected by CryoSPARC. After auto-picking, 5,214,695 particles  
572 were extracted and subjected to 2D classification. After 2D classification, 2,391,813 particles were used  
573 for non-uniform 3D and local refinement to generate the final 2.74 Å map. To further improve the CTD  
574 density map, 3D classification was performed. The best of the 10 classes, containing 66,251 particles,  
575 was used for further refinement. Local refinement with masking of the CTD allowed a resolution 4.03 Å  
576 to be reached.

577

### 578 **Model building and refinement**

579 The initial model of CLC-2 was generated by SWISS-MODEL using human CLC-1 (PDB:6qvc)  
580 as a homology model. It was fit to each map and manually rebuilt using Coot (Emsley and Cowtan,  
581 2004) (v0.91). The models were further refined with ISOLDE (Croll, 2018) in ChimeraX (Pettersen et  
582 al., 2004) (v.1.6) and Phenix (Liebschner et al., 2019) (v1.20) real space refinement. The two potential  
583 conformations for the AK-42 ligand were tested using the Quantum Mechanical Restraints (QMR)  
584 method (Liebschner et al., 2023). Q-scores were performed with the MapQ Chimera plugin v1.9.12.

585

### 586 **Cell surface protein biotinylation and isolation**

587 CHO K1 cells (ATCC CCL-61) were cultured at 37°C [95/5% O<sub>2</sub>/CO<sub>2</sub> ratio] in F12K media  
588 (ATCC, Catalog no. 30-2004) supplemented with 10% fetal bovine serum (Gibco) and 1%  
589 penicillin/streptomycin (Gibco). Cells were seeded at 5×10<sup>6</sup> in 15-cm dishes. After 48 hours, the  
590 confluency reached around 60%, and cells were transfected with 6 µg of CLC-2 plasmid, either WT or  
591 Delta-N, using Lipofectamine LTX, opti-MEM, and PLUS reagent (Invitrogen). For the control sample,  
592 CHO cells were seeded at the same time as the transfected groups and kept culturing in parallel. 48-72  
593 hours after transient transfection, two 15-cm dishes cells for each sample (WT, delta-N, or control) were  
594 combined to create one sample for use in the biotinylation of surface proteins assay, which was  
595 performed using a Pierce cell surface protein biotinylation and isolation kit (Thermo Scientific, A44390).

596 Briefly, cells were washed twice in PBS (0.1 M sodium phosphate, 0.15 M NaCl, pH 7.2) and then  
597 incubated with PBS containing 0.25 mg/ml of sulfosuccinimidyl 2-(biotin-amido)-ethyl-1,3-  
598 dithiopropionate (EZ-link Sulfo-NHS-SS-biotin, Pierce) at room temperature for 10 minutes. Cells were  
599 incubated in ice-cold TBS (25 mM Tris, 0.15 M NaCl, pH 7.2) twice to quench the labeling. Cells were  
600 then scraped and lysed in lysis buffer from the Kit. Samples were incubated at 4°C for 30 minutes and  
601 then centrifugated at 15,000 × g for 5 minutes. Following centrifugation, the extracted membrane  
602 samples from the supernatant were incubated with 50 µl NeutrAvidin™ Agarose (Pierce) at 4°C for 2  
603 hours, then washed with wash buffer from the kit four times. Finally, the isolated proteins were eluted  
604 with 60 µl elution buffer (from the kit) containing 100 mM DTT. 40 µl of each sample was used for  
605 Western blotting detection with 1:2,500 anti-GFP antibody (Invitrogen A11122) and 1:10,000 anti-rabbit  
606 secondary antibody (Licor 926-68073). The relative expression level was calculated by quantifying the  
607 intensities of the 100-kD bands on the Western blot, using a Li-Cor Odyssey 9120 Infrared Imaging  
608 System. The samples from three independent experiments (independent transfections on different  
609 days) were run on a single Western blot, shown in Figure 6D and in Figure 6 – source data 2.

610

### 611 **Cell Culture and patch-clamp recording**

612 CHO K1 cells (ATCC CCL–61) were cultured at 37°C [95/5% O<sub>2</sub>/CO<sub>2</sub> ratio] in F12K media (ATCC,  
613 Catalog no. 30-2004) supplemented with 10% fetal bovine serum (Gibco) and 1%  
614 penicillin/streptomycin (Gibco). At 60% confluency, cells were transfected with 120 ng CLC-2, either  
615 WT or delta-N, using Lipofectamine LTX, opti-MEM, and PLUS reagent (Invitrogen). 105 ng of a soluble  
616 GFP construct was co-transfected with the CLC-2 construct to improve visualization of transfected  
617 cells.

618 Whole-cell patch-clamp experiments were performed using an Axopatch 200B amplifier attached to a  
619 Digidata 1440A. Data were acquired at 10 kHz with filtering at 5 kHz. Traces shown in figures were  
620 filtered offline in Clampfit at 1 kHz (8-pole Bessel). Borosilicate glass micropipettes (Sutter Instruments  
621 BF150-86-10) were pulled and fire-polished to a tip diameter with a resistance of 1.8 to 3.4 MΩ. For

622 whole-cell patch-clamp recordings, the external solution was composed of 148 mM CsCl, 2 mM CaCl<sub>2</sub>  
623 (from a 1 M aqueous stock), 100 mM D-mannitol, and 10 mM HEPES, adjusted to pH 7.4 with 2 M  
624 CsOH. The internal solution was composed of 146 mM CsCl, 5 mM EGTA, 5 mM NaF, 60 mM D-  
625 mannitol, and 10 mM HEPES, adjusted to pH 7.4 with 2 M CsOH. Bath perfusion of external solution (2  
626 mL/min) was initiated after whole cell and series resistance compensation (70% or more) was  
627 established. For leak subtraction, 300 nM AK-42 was perfused at 2 mL/min. AK-42 was diluted from a 1  
628 mM stock solution in DMSO (0.03% final [DMSO]).

629

### 630 **MD simulations**

631 **System setup for MD simulations.** The apo dimer structure was used for simulations. For all  
632 simulations, hydrogen atoms were added, and protein chain termini were capped with neutral acetyl  
633 and methylamide groups. Titratable residues were kept in their dominant protonation state at pH 7.  
634 Histidine residues were modeled as neutral, with a hydrogen atom bound to epsilon nitrogen. The  
635 Dowser program was used to hydrate pockets within and around each structure (Morozenko and  
636 Stuchebrukhov, 2016). Then the receptor was inserted into a pre-equilibrated palmitoyl-oleoyl-  
637 phosphatidylcholine (POPC) bilayer using Dabble (Betz, 2017). Sodium and chloride ions were added  
638 to neutralize each system at a concentration of 150 mM. Approximate system dimensions were 131 Å x  
639 95 Å x 125 Å.

640 **Simulation protocols.** All simulations were run on a single Graphical Processing Unit (GPU)  
641 using the Amber18 Compute Unified Device Architecture (CUDA) version of particle-mesh Ewald  
642 molecular dynamics (PMEMD) (Salomon-Ferrer et al., 2013). We used the CHARMM36m parameter  
643 set for protein molecules, lipids, and ions, and the CHARMM TIP3P water model for waters (Huang and  
644 MacKerell, 2013). Heating (to 310 K over 137.5 ps) and equilibration (28 ns with restraints on protein  
645 and ligand) steps were performed before production simulations as described previously (Suomivuori et  
646 al., 2020). Trajectory snapshots were saved every 200 ps. All simulations were at least 2 microseconds  
647 in length.



648           **Simulation analysis protocols.** The AmberTools18 CPPTRAJ package (Roe and Cheatham,  
649 2013) was used to reimage trajectories, while Visual Molecular Dynamics (VMD) (Humphrey et al.,  
650 1996), PyMol (Schrodinger), and Matplotlib Python package were used for visualization and analysis.  
651 For analysis, the N-terminus peptide backbone was defined as segment name P5, excluding residues  
652 14 15 27 28. For the CTD analysis, we used segment names P9 P3 P4 P8 excluding residue 419 to  
653 578. For bar plots, individual dots show the average value in each independent simulation. Bar values  
654 show the average value across the independent simulations. The error bars for simulation results show  
655 the 68% confidence intervals of the mean (appropriate for non-parametric distributions) calculated  
656 using bootstrapping with the Seaborn Python library.

657

## 658 **ACKNOWLEDGMENTS**

659 We thank Huawei Zhang for sharing pdb coordinates and cryo-EM density for CLC-2/AK-42 in advance  
660 of release. We thank Anna Koster, Bill Kobertz, Dan Collins, Jürgen Kreiter, Martin Prieto, Shwetha  
661 Srinivasan, and Chris Miller for comments on the manuscript. We also thank Nigel Moriarty (Phenix) for  
662 performing Quantum Mechanical Restraints (QMR) analysis of the AK-42 ligand.

663

## 664 **FUNDING**

665 This research was funded by NIH R21NS125767 (M.M. and W.C.) and NIH R01NS113611 (M.M.,  
666 J.D.B., and R.O.D.). CryoEM was performed at the Stanford-SLAC Cryo-EM Center (S<sup>2</sup>C<sup>2</sup>), which  
667 is supported by the National Institutes of Health Common Fund Transformative High-Resolution Cryo-  
668 Electron Microscopy program (U24 GM129541). M.X. was supported by a Wu Tsai Neurosciences  
669 Institute Interdisciplinary Scholar Award. S.D.M. is supported by a Stanford Bio-X Bowes fellowship.

670

## 671 **AUTHOR CONTRIBUTIONS**

672 **MX:** Conceived and carried out experiments, performed molecular biology to generate constructs,  
673 purified protein, collected and analyzed cryoEM data, built and refined experimental model, performed



674 surface biotinylation experiments, generated figures, drafted, reviewed, and edited manuscript. **TN:**  
675 Conceived, carried out, and analyzed electrophysiology experiments, reviewed manuscript. **ASP:**  
676 Conceived, carried out, and analyzed MD simulations, reviewed and edited manuscript. **YL:** cryoEM  
677 data collection and analysis. **SDM:** Synthesized AK-42, performed transfections and cell culture for  
678 electrophysiology experiments, analyzed electrophysiology data, reviewed and edited manuscript. **GP:**  
679 Model refinement, analysis, validation and deposition, writing related to ligand modeling and validation.  
680 **JDB:** Supervision, manuscript review and editing, funding. **ROD:** Supervision, manuscript review and  
681 editing, funding. **WC:** Supervision, manuscript review and editing, funding. **MM:** Conceived  
682 experiments, supervised, drafted, reviewed, and edited manuscript, funding.

683

## 684 DATA AVAILABILITY

685 Cryo-EM Density maps and structure coordinates have been deposited in the Electron  
686 Microscopy Data Bank (EMDB) and the Protein Data Bank (PDB), with accession codes EMD-41127  
687 and PDB 8TA3 for the CLC2-TM, EMD-41128 and PDB 8TA4 for the CLC2-CTDsym, EMD-41129 and  
688 PDB 8TA5 for CLC2-CTDasym, EMD-41126 and PDB 8TA2 for CLC2-TM-AK42, and EMD-41130 and  
689 PDB 8TA6 for CLC2-AK42-CTD-only.

690

## 691 FIGURE LEGENDS

692 **Figure 1. Gating conformations in CLC transporters and channels. (A)** Cartoon depictions of the  
693 CLC anion-permeation pathway. The “gating glutamate” ( $E_{\text{gate}}$ ) can occupy anion binding sites within  
694 the permeation pathway (“down” and “middle” conformations, occupying the central ( $S_{\text{cen}}$ ) and  
695 external ( $S_{\text{ext}}$ ) anion-binding sites respectively) or away from these sites (“up” and “out”  
696 conformations). Coupling of  $E_{\text{gate}}$  movement to  $\text{Cl}^-/\text{H}^+$  binding/unbinding and global conformational  
697 change generates 2:1  $\text{Cl}^-/\text{H}^+$  exchange. **(B)**  $E_{\text{gate}}$  is required for voltage-dependent gating in CLC  
698 channels but cryoEM density for this residue has been observed only in CLC-1 (PDB ID: 6coy), in the  
699 “out” position. In contrast to CLC-1, which is predominantly open at zero mV, CLC-2 is predominantly

700 closed. The open probability ( $P_o$ ) versus voltage (V) traces were drawn based on published data  
701 reported for CLC-1 (Lisal and Maduke, 2008) and CLC-2 (Stolting et al., 2013).

702

703 **Figure 2. CryoEM structure of the human CLC-2 channel.** Overall structure of the transmembrane  
704 domain ("CLC2-TM") at 2.46 Å. The identical subunits of the homodimer are shown in purple and  
705 gray, Cl<sup>-</sup> ions are shown as green balls. **(A)** cryoEM density map with model overlay (contour level:  
706 0.71, 5.5  $\sigma$ ) and **(B)** model only with dashed arrows indicating the locations of pathways detected by  
707 Caver: orange, primary Cl<sup>-</sup> pathway common to all CLCs; yellow, secondary Cl<sup>-</sup> pathway detected in  
708 CLC-2 and CLC-1. Details of the pathways are presented in Figure 3. The secondary pathway,  
709 whose function is not yet known, was so named when first observed in the CLC-1 structure (Park and  
710 MacKinnon, 2018). **(C)** Zoomed-in views showing cryoEM density overlay of bound Cl<sup>-</sup> and key  
711 residues – E<sub>gate</sub> (E205) and inner-gate residues Ser<sub>C</sub> (S162) and Tyr<sub>C</sub> (Y553). S<sub>cen</sub> is indicated with a  
712 green dashed circle. Contour level: 1.1, 7.2  $\sigma$  (middle panel); 0.97, 6.3  $\sigma$  (right panel).

713

714 **Figure 2 - figure supplement 1. Micrograph, 2D classes, and structure validation of CLC2-TM.**

715 **(A)** Representative motion-corrected cryoEM micrograph. **(B)** 2D class averages. **(C)** Gold standard  
716 FSC plots calculated in cryoSPARC. **(D)** Local resolution of the cryoEM map of the CLC2-TM. **(E)**  
717 Model validation using Q-scores (Pintilie et al., 2020) of subunit A (left) and subunit B (right). The  
718 black line represents the expected Q-score at respective resolution based on the correlation between  
719 Q-scores and map resolution.

720

721 **Figure 2 - figure supplement 2. CryoEM workflow of the CLC2 single-particle cryoEM data**

722 **processing.** A total of 14,198 movie stacks were collected on a 300 kV Titan Krios cryo-electron  
723 microscope. cryoSPARC was used for 2D classification, and the CLC2-TM density map was obtained  
724 after 2D classification. Relion was used for 3D classification and yielded two conformations differing

725 in the CTD: CLC2-CTDsym and CLC2-CTDasym. Resolutions shown refer to the whole protein  
726 molecule.

727

728 **Figure 2 - figure supplement 3. Helix map of CLC2-TM.** cryoEM densities and model of CLC-2  
729 transmembrane helices (contour level: 0.73, 2.7  $\sigma$ )

730

731 **Figure 2 - figure supplement 4. E<sub>gate</sub> position and Cl<sup>-</sup> binding sites (S<sub>ext</sub> and S<sub>cen</sub>).** (A)  
732 Comparison between CLC-2 (purple), CLC-1 (light blue), and cmCLC (salmon pink). E<sub>gate</sub> (E205 in  
733 CLC-2, E232 in CLC-1, and E210 in cmCLC), Ser<sub>C</sub> (S162 in CLC2, S189 in CLC-1, and S165 in  
734 cmCLC) and Tyr<sub>C</sub> (Y553 in CLC-2, Y578 in CLC-1, and Y515 in cmCLC) are shown as sticks. In  
735 CLC-2 and cmCLC, S<sub>ext</sub> is occupied by Cl<sup>-</sup>, and S<sub>cen</sub> is occupied by E<sub>gate</sub>. E<sub>gate</sub> is in the “down”  
736 position. In CLC-1, S<sub>ext</sub> is occupied by Cl<sup>-</sup>, and S<sub>cen</sub> lacks anion density. E<sub>gate</sub> is in the “out” position,  
737 away from the Cl<sup>-</sup>-permeation pathway. (B) Overlay view (stereo) of panel A. (C) Overlay with the  
738 CLC-2 E<sub>gate</sub> conformations modeled in PDB ID: 7XJA (Ma et al., 2023).

739

740 **Figure 3 Pore profile detected in CLC-2.** (A). Left: The primary (orange) and secondary (yellow) pore  
741 detected in CLC-2 using Caver. Middle: The detected pore radii are displayed in dots as a color map.  
742 Right: Zoomed-in view of the restricted (narrowest) site of the pore profile, using the same coloring as  
743 in the middle panel. E<sub>gate</sub>, Ser<sub>C</sub> and Tyr<sub>C</sub> are shown as sticks. (B). Pore profile for CLC-1 (PDB  
744 ID:6coy), with display as in panel A.

745

746 **Figure 3 - figure supplement 1. Cl<sup>-</sup> pathway in CLC-2 and CLC-1.** (A) CLC-2 Cl<sup>-</sup> pathway as  
747 shown in Figure 3 but omitting sections with pore radius less than 1Å. E<sub>gate</sub>, occupying the S<sub>cen</sub> site,  
748 blocks the canonical Cl<sup>-</sup> pathway. (B) same as panel A, for CLC-1 (PDB ID:6coy).

749

750 **Figure 3 - figure supplement 2. Comparison of primary and secondary Cl<sup>-</sup> pathways with**  
751 **transporter Cl<sup>-</sup> and H<sup>+</sup> pathways. (A)** The top two panels are repeated from Figure 3A, indicating  
752 the primary (orange) and secondary (yellow) caver-detected pores in CLC-1 and CLC-2. The lower  
753 panel shows CLC-ec1 (PDB ID: 1OTS), a representative for the CLC transporters, where caver  
754 detects only the primary pore (orange dots as for CLC-1 and CLC-2). **(B)** Detected pore radii show a  
755 longer constriction in the CLC-ec1 transporter compared to the CLC-1 and CLC-2 channels. **(C)**  
756 Zoomed-in view of the secondary-pore region for CLC-2 (top), CLC-1 (middle) and CLC-ec1  
757 (bottom). The CLC-ec1 panel shows water wires (space-filled) detected in simulations of the QQQ  
758 mutant structure (PDB ID: 6V2J) (Chavan et al., 2020).

759

760 **Figure 4. Different conformations of the CTD. (A).** Overall structure of the two CLC-2  
761 conformations. Left: CLC2-CTDsym at 2.75 Å. Right: CLC2-CTDasym at 2.76 Å. The subunits of the  
762 homodimer are shown in orange (CLC2-CTDsym) or yellow (CLC2-CTDasym) and gray (for both).  
763 The subunits adopting different CTD conformations are shown in orange and yellow, while the  
764 subunits sharing the same CTD conformation are shown in gray. The dashed line demarcates the  
765 transmembrane (TM) and cytoplasmic (CTD) domains. A hairpin structure detected at the  
766 intracellular pore is shown in blue. **(B)** Overlay of two conformations. **(C)** Hinge movement of the  
767 CTD between two conformations. The middle panel shows an overlay of CLC2-CTDsym (orange and  
768 gray) and CLC1-CTDasym (yellow and gray), with the CTDs highlighted in boxes. For the subunits  
769 that adopt different conformations (orange and yellow), the double-headed arrow indicates the  
770 change between the two conformations. The RMSD between the subunits shown in orange/yellow is  
771 6.9 Å, while the RMSD for the subunits shown in gray is only 1.3 Å. Alignments of only the CTDs are  
772 shown at left and right; in these alignments, the low RMSD values (0.9 Å and 1.0 Å, respectively)  
773 indicate that the CTDs undergo a hinge movement.

774

775 **Figure 4 - figure supplement 1. Structure validation of CLC2-CTDsym and CLC2-CTDasym. (A)**  
776 Gold standard FSC plots calculated in cryoSPARC for CLC2-CTDsym. **(B)** Local resolution of the  
777 cryo-EM map of the CLC2-CTDsym. **(C)** Model validation using Q-scores of subunit A (left) and  
778 subunit B (right) of CLC2-CTDsym. The black line represents the expected Q-score at respective  
779 resolution based on the correlation between Q-scores and map resolution. **(D-F)** the same as **(A-C)**  
780 for CLC2-CTDasym.

781  
782 **Figure 4 – figure supplement 2. CryoEM density maps for the two CTD-containing CLC-2**  
783 **conformations, overlaid with structural models. (A)** CLC2-CTDsym (contour level: 0.68, 4.9  $\sigma$ ).  
784 **(B)** CLC2-CTDasym (contour level: 0.75, 6.8  $\sigma$ ). Side view (left) and top view (right) are shown. **(C)**  
785 CTD of CLC2-CTDsym shows two CBS domains on each subunit (orange and light orange for  
786 subunit A; gray and light gray for subunit B).

787  
788 **Figure 4 - figure supplement 3. MD analysis indicates conformational flexibility of the CTD. (A)**  
789 The CTD is highly mobile relative to the transmembrane domain, and often tilts upward or downward  
790 relative to its initial location. In the inset images, two representative frames from simulation are  
791 shown (orange) overlaid on the starting structure (black outline). **(B)** The RMSD (root mean square  
792 deviation) and RMSF (root mean square fluctuation) of the cytoplasmic domain backbone were  
793 calculated after aligning frames on the transmembrane domains. Bars show the mean of five  
794 independent simulations, each 2.0  $\mu$ s in length. Error bars are 68% confidence intervals of the mean.

795  
796 **Figure 4 - figure supplement 4. Comparison of CTD orientation with respect to the TM domain.**  
797 **(A)** The CLC-1 structure is shown in light blue. The angle of orientation for the CTDs was calculated  
798 using the far end residue of helix T (the second helix of first CBS domain) as the endpoint of rays and  
799 the center of the TM-CTD connecting plane as the vertex of the angle. On the right the CTD is shown  
800 in surface representation following rotation as indicated. Panels **(B) – (F)** show the CLC homolog

801 indicated, with angles calculated as for CLC-1, and the rotated view of the CTD shown to compare  
802 the positioning of the CTDs relative to the membrane domains. The dashed lines indicate the long  
803 axes of the CTDs. In each panel, CLC-1 is shown in light blue as a reference for comparison. **(G)** and  
804 **(H)** overlays compare the CTD orientations in the CLC-2 structures to that in CLC-7. PDB IDs are  
805 shown in the parentheses. PDB IDs for CLC2-CTDsym and CLC2-CTD asym are 8TA4 and 8TA5.

806

807 **Figure 4 – figure supplement 5. ATP binding site comparison between CLC-2 and CLC-5.** Top:  
808 Structural overlay of CLC2-CTDsym (in orange) and CLC5-CTD (in dark purple) with ATP (pink  
809 carbon atoms; CPK coloring on non-carbon atoms. PDB ID: 2J9L). Bottom: Zoomed in stereo view of  
810 ATP binding site in CLC5-CTD (dark purple) overlaid with the same region in CLC2-CTDsym  
811 (orange). Residue numbers are labeled in dark purple for CLC-5 and orange for CLC-2.

812

813 **Figure 5. The blocking hairpin structure corresponds to an N-terminal sequence of CLC-2. (A).**  
814 *Left:* The hairpin structure seen in the cryoEM density (blue mesh) fits N-terminal residues 14-28  
815 (blue). *Right:* The subunit in CLC2-CTDasym structure that contains a CTD with rotated orientation  
816 lacks density for the hairpin structure. In this structure, the residues linking TM helices J and K are  
817 not resolved. The dark blue circles indicate this unresolved region (right panel) and the  
818 corresponding resolved J-K helix that occurs in the other subunits. (Contour level: 0.76, 5.5  $\sigma$ .) **(B)**  
819 Model validation using Q-scores for the N-terminal hairpin: orange and light orange for subunits A &  
820 B of CLC2-CTDsymsubunit; yellow for subunit A (the hairpin-containing subunit) of CLC2-CTDasym.  
821 The black line represents the expected Q-score at 2.75 Å based on the correlation between Q-scores  
822 and map resolution. **(C)** Residues on the transmembrane domain interact with the N-terminal hairpin.  
823 The J-K helical linker and TM Helices C, D, R, and J are labeled with arrows. Inset: Zoomed-in view  
824 of two hydrogen bonds formed between the hairpin structure and the TM domain: Q19-Q153 and  
825 T20-R363. Mutation of these two residues (Q25 and T26 in rat CLC-2) generated an open-channel  
826 phenotype for CLC-2 expressed in *Xenopus* oocytes (Grunder et al., 1992).

827

828 **Figure 5 – figure supplement 1.** Comparison of peptide candidates fitting into the hairpin density.

829 (A) Best-fitting peptide candidate from the N-terminus (left shown in blue) and from the C-terminus

830 (right shown in purple) fitted into cryoEM hairpin density (blue mesh). (B) Q-score plot of the two

831 peptide candidates (residues 1-15 of the respective sequences). The Q-scores for the C-terminal

832 peptide are generally lower than the Q-score expected for the corresponding resolution (0.65).

833

834 **Figure 5 supplement 2. N-terminal hairpin sequence is conserved in CLC-2, but not other**

835 **CLCs.** (A) Alignment of the N-terminal hairpin sequence (blue boxed) amongst different species. (B)

836 Alignment of N-terminal hairpin sequence (blue boxed) amongst other human CLCs.

837

838 **Figure 5 – figure supplement 3.** Electrostatic map of the N-terminal hairpin blocking site. Left: view

839 from the cytoplasm showing the electrostatic surface potential of the TM region (blue, positive; red,

840 negative), with the hairpin shown in cartoon. Right: side view showing the electrostatic surface

841 potential of the hairpin (blue, positive; red, negative) and the TM blocking site shown in transparent

842 cartoon model.

843

844 **Figure 5 – figure supplement 4. MD simulations confirm the N-terminal hairpin structure is**

845 **stable** (A) In simulations, the N-terminus (blue) remains stably bound to the intracellular side of the

846 transmembrane domain (orange). In the inset image, frames of the N-terminus taken every 200 ns

847 from a representative simulation are overlaid. (B) The root-mean-square deviation (RMSD) and root-

848 mean-square fluctuation (RMSF) of the N-terminus backbone were calculated after aligning frames

849 on the transmembrane domains. Bars show the mean of five independent simulations, each 2.0  $\mu$ s in

850 length. Error bars are 68% CI (confidence interval of the mean).

851



852 **Figure 5 - figure supplement 5.** The N-terminal hairpin blocks the primary Cl<sup>-</sup> pore in CLC-2. **(A)**  
853 *Left:* Side view of CLC2-TM showing the caver-detected pore (primary in orange and secondary in  
854 yellow). *Right:* View of the primary pore from the intracellular side. **(B)** The N-terminal hairpin (blue)  
855 overlaid with CLC2-TM as shown in panel **A**.

856

857 **Figure 5 – figure supplement 6. Mapping mutant data onto the cryoEM structure. (A)** Left: same  
858 as Figure 5C, showing hairpin interactions. Right: Rotated view highlighting ball “receptor” residues  
859 identified by Jordt and Jentsch, 1997. **(B)** Residues mutated in human Aldosteronism (Fernandes-  
860 Rosa et al., 2018; Scholl et al., 2018) and Leukoencephalopathy (Gaitan-Penas et al., 2017) are  
861 shown on CLC2-CTDsym in magenta and green, respectively).

862

863 **Figure 6 Patch-clamp experiments support CLC-2 channel block by the N-terminal hairpin**  
864 **structure. (A)** Representative currents from WT and delta-N CLC-2, recorded using the whole-cell  
865 patch clamp configuration in response to the voltage protocol shown. **(B)** WT CLC-2 recording from  
866 panel A, shown on an expanded scale. **(C)** Summary of current levels measured for WT and delta-N  
867 CLC-2 at the end of the 1-s voltage pulse to -100 mV. Data are from six independent transfection  
868 samples, in each case with WT and delta-N recorded on the same day following transfection. WT: -  
869  $600 \pm 102$  pA (SEM, n=8); Delta-N:  $-3300 \pm 630$  pA (SEM, n=8). **(D)** Western blot detection of  
870 biotinylated surface-expressed CLC-2 from three independent experiments. **(E)** Summary data for  
871 electrophysiology and surface-biotinylation experiments. Points representing individual experiments  
872 for Delta-N surface biotinylation (each normalized to WT) are shown. Individual data points for the  
873 electrophysiology experiments are shown in panel C. **(F)** Representative examples of experiments to  
874 evaluate current run-up in WT and Delta-N CLC-2. *Left panels:* Time course data. Following an initial  
875 voltage-family measurement (I-V protocol as in panel A, taken at point “1”), currents were monitored  
876 by 1-s pulses to -100 mV every 5 s for five minutes, after which a second voltage-family  
877 measurement was made (point 2), followed by application of AK-42 to facilitate leak subtraction, and



878 a final voltage-family measurement at point 3. I-V traces are shown at right. **(G)** Summary data for  
879 “run-up” experiments. *Left panel:* Normalized time-dependent currents for WT and delta-N. Currents  
880 were first leak-subtracted (using the steady-state current after AK-42 application) and then  
881 normalized to the amplitude of the current measured in the first step of the 5-minute sequence. *Right*  
882 *panels:* Leak-subtracted current levels at -100 mV from “initial” and “final” IV traces measured at  
883 points “1” and “2” in the time course (panel F). Average initial and final currents ( $\mu\text{A} \pm \text{SEM}$ ,  $n=8$ ) are  
884 WT:  $-600 \pm 102$  and  $-1400 \pm 260$ ; Delta-N:  $-3300 \pm 630$  and  $-2900 \pm 420$ .

885

886 **Figure 6 – figure supplement 1.** Data traces from the CLC-2 run-up experiments summarized in  
887 Figure 6G. For Delta-N, separate scale bars indicate the currents for the top six and bottom 10  
888 traces. AK-42 leak currents, not subtracted in these raw data traces, are summarized in Figure 6 –  
889 source data 1.

890

891 **Figure 6 – figure supplement 2. CLC-2 current rectification.** **(A)** Example traces from two  
892 experiments on WT CLC-2. Current values at end of the -100-mV test pulses and in the steady-state  
893 portion of the +80-mV tail pulse (following the +20-mV test pulse) are indicated. Robust AK-42  
894 inhibition of the current at +80 mV indicates that CLC-2 is passing current at positive voltages. **(B)**  
895 Rectification ratios. Rectification was quantified by taking the ratio (absolute value) of the leak-  
896 subtracted currents at -100 mV and +80 mV. For WT initial currents, the low currents at +80 mV  
897 make this quantification challenging: for 5 out of 8 experiments on WT CLC-2, the AK-42 current at  
898 +80 mV was greater than the initial WT current at +80 mV, likely due to an increase in leak over the  
899 course of the experiment (~15 minutes of voltage pulsing). Therefore, the rectification calculated for  
900 the WT initial currents ( $99 \pm 34$ , SEM  $n=3$ ) has substantial uncertainty. That said, such high  
901 rectification is consistent with reports of CLC-2 rectification throughout the literature (Park et al.,  
902 1998; Arreola et al., 2002; Jentsch and Pusch, 2018). On the other hand, Delta-N currents display  
903 only mild rectification, which is straightforward to quantify given the high signal:noise (high AK-42-

904 sensitive current relative to background), and which does not change in response to voltage pulsing.  
905 For “WT-final”, the rectification ratio similarly can be accurately quantified. Thus, while the high  
906 uncertainty and variance in estimating WT initial rectification precludes quantitative statistical  
907 comparisons, these data strongly suggest that WT CLC-2 current rectification decreases in parallel to  
908 current run-up. **(C)** WT initial rectification ratio from panel B replotted to show the individual data  
909 points from the 3 experiments in which AK-42 current at +80 mV was less than the initial WT current  
910 at +80 mV. Data for all experiments are summarized in Figure 6 – source data 1.

911

912 **Figure 7 Bound AK-42 blocks the Cl<sup>-</sup> pathway in CLC-2.** **(A)** TM-domain structure of the CLC-2  
913 structure in complex with AK-42 (CLC2-TM-AK42) at 2.74 Å. The identical subunits of the homodimer  
914 are shown in hot pink and gray; Cl<sup>-</sup> ions are shown as green balls. Bound AK-42 is highlighted with a  
915 yellow circle on the pink subunit. The cyan arrow indicates the Cl<sup>-</sup> pathway. **(B)** Zoomed-in view of  
916 the AK-42 binding site (contour level: 0.91, 6.0  $\sigma$ ). **(C)** A sliced view of CLC-2 showing AK-42 (yellow  
917 carbon atoms; CPK coloring on non-carbon atoms) and E<sub>gate</sub> (CPK sticks). Both AK-42 and E<sub>gate</sub>  
918 obstruct the Cl<sup>-</sup> pathway, displayed as a color map.

919

920 **Figure 7 - figure supplement 1. CryoEM workflow of the CLC2-TM-AK42 single-particle cryo-**  
921 **EM data processing.** A total of 14,300 movie stacks were collected on a 300 kV Titan Krios cryo-  
922 electron microscope. cryoSPRAC was used for 2D classification and CLC2-TM-AK42 density map  
923 was obtained after 2D classification. Relion was used for 3D classification.

924

925 **Figure 7 - figure supplement 2.** Micrograph and 2D classes and structure validation of CLC2-AK42.  
926 **(A)** Representative motion-corrected cryo-EM micrograph. **(B)** 2D class averages. **(C)** Gold standard  
927 FSC plots calculated in cryoSPARC for CLC2-TM-AK42 (left) and CLC2-AK42-CTD-only (right). **(D)**  
928 Local resolution of the cryo-EM map for CLC2-TM-AK42 (left) and CLC2-AK42-CTD-only (right)

929 **Figure 7 - figure supplement 3. Model validation using Q-scores.** (A) Q-scores of CLC2-TM-  
930 AK42 for subunit A (left) and subunit B (right). (B) Q-scores of CLC2-AK42-CTD-only for subunit A  
931 (left) and subunit B (right). The black line represents the expected Q-score at respective resolution  
932 based on the correlation between Q-scores and map resolution.

933

934 **Figure 7 - figure supplement 4. cryoEM map and structure of CLC2-AK42.** (A) cryoEM model of  
935 CLC2-TM-AK42 with docked CTD. The transmembrane region is shown in hot pink and gray. The  
936 CTD is shown in green and gray. AK-42 is shown in yellow and highlighted by yellow circles. Chloride  
937 ions are shown in green. (B) cryoEM model overlay with density map of CLC2-AK42. Contour level:  
938 0.83, 6.8  $\sigma$  (TM region); 0.35, 14  $\sigma$  (CTD).

939

940 **Figure 7 - figure supplement 5. Helix map of CLC2-TM-AK42.** cryo-EM densities and model of  
941 CLC2-AK42 transmembrane helices (contour level: 0.52, 3.4  $\sigma$ )

942

943 **Figure 7 – figure supplement 6. Density overlay at key Cl<sup>-</sup>-pathway residues.** Zoomed-in view  
944 highlighting residues S162, E205, Y553, and the bound chloride ion, with cryoEM density overlay  
945 (contour level: 1.4, 9.0  $\sigma$ ).

946

947 **Figure 7 - figure supplement 7. AK-42 binding site comparison between CLC2-TM and CLC2-  
948 TM-AK42.** Top: Stereo view of structural overlay at the AK-42 binding site. Hydrogen bonds between  
949 AK-42 and residues K204,S392,K394 are indicated by blue dashed lines. Bottom: A view highlighting  
950 the movement of residue M460 to make space for AK-42.

951

952 **Figure 7 - figure supplement 8. Structural comparison of CLC2-TM and CLC2-TM-AK42.**  
953 Difference distance matrices comparing Ca residues on TM helices between CLC2-TM and CLC2-  
954 TM-AK42 in subunits A (A) or B (B). Residues in loops connecting helices, where there is low

955 confidence in the model building (Q score lower than the expected Q score of 0.65), were omitted  
956 from the matrices.

957

958 **Figure 7 - figure supplement 9 AK-42 binding site comparison between CLC-2 and CLC-1. (A)**

959 Top: Stereo view of the AK-42 binding site in CLC2-TM-AK42 (hot pink) overlaid with the same  
960 region in CLC-1 (blue, PDB:6coy). Residue numbers correspond to those of CLC-2. The five residues  
961 that differ between CLC-2 and CLC-1 are: I112 (S139), S392 (M419), Q393 (P420), K394 (R421),  
962 and L397 (I424). Bottom: Rotated (stereo) view of AK-42 binding site to compare residues S392,  
963 Q393 and K394 in CLC-2 versus M419, P420 and R421 in CLC-1. These three were calculated to  
964 contribute most significantly to the AK-42 binding energy (Ma, 2023). **(B)** Residues in CLC-1  
965 predicted to clash with AK-42. AK-42 is shown in yellow sticks and white surface. F252 and M460 in  
966 CLC-2 correspond to F279 and M485 in CLC-1.

967

968 **FIGURE 8:** CLC-2's gating is illustrated based on our new structural data. Opening of each protopore  
969 requires at least two events – unblock by the N-terminal hairpin (“N-ter”) and rotation of  $E_{\text{gate}}$  away  
970 from the permeation pathway. The dashed green arrow represents the  $\text{Cl}^-$  conduction pathway.  
971 Hairpin unblock (ball and chain gating) is coupled to conformational change of the CTD: rotation of  
972 the CTD towards the membrane precludes hairpin binding, thus facilitating channel opening. Opening  
973 of the channel pore following these two events is depicted for one subunit of the homodimer (filled  
974 green arrow).

975

976 **Video 1. CLC-2 pore detected using Caver.**

977 **Video 2. CLC-1 pore detected using Caver.**

978 **Video 3. CLC-ec1 Caver detected pathway.**

979 **Video 4. Rigid body movement from CLC2-CTDsym to CLC2-CTDasym.**

980 **Video 5. Hairpin surface potential.**

981 **Video 6. AK-42 density.**

982

983

984

985 **REFERENCES**

- 986 Accardi, A., and C. Miller. 2004. Secondary active transport mediated by a prokaryotic homologue of  
987 ClC Cl<sup>-</sup> channels. *Nature*. 427:803-807.
- 988 Ahmed, N., M. Ramjeesingh, S. Wong, A. Varga, E. Garami, and C.E. Bear. 2000. Chloride channel  
989 activity of ClC-2 is modified by the actin cytoskeleton. *Biochem. J.* 352 Pt 3:789-794.
- 990 Alioth, S., S. Meyer, R. Dutzler, and K. Pervushin. 2007. The cytoplasmic domain of the chloride channel  
991 ClC-0: structural and dynamic characterization of flexible regions. *J. Mol. Biol.* 369:1163-1169.
- 992 Altamura, C., J.F. Desaphy, D. Conte, A. De Luca, and P. Imbrici. 2020. Skeletal muscle ClC-1 chloride  
993 channels in health and diseases. *Pflugers Arch.* 472:961-975.
- 994 Anashkin, V.A., A.A. Baykov, and R. Lahti. 2017. Enzymes Regulated via Cystathionine beta-Synthase  
995 Domains. *Biochemistry (Mosc.)*. 82:1079-1087.
- 996 Arreola, J., T. Begenisich, and J.E. Melvin. 2002. Conformation-dependent regulation of inward rectifier  
997 chloride channel gating by extracellular protons. *J. Physiol.* 541:103-112.
- 998 Betz, R.M. 2017. v2.6.3. *Zenodo*.
- 999 Bosl, M.R., V. Stein, C. Hubner, A.A. Zdebik, S.E. Jordt, A.K. Mukhopadhyay, M.S. Davidoff, A.F. Holstein,  
1000 and T.J. Jentsch. 2001. Male germ cells and photoreceptors, both dependent on close cell-cell  
1001 interactions, degenerate upon ClC-2 Cl<sup>-</sup> channel disruption. *EMBO J.* 20:1289-1299.
- 1002 Brenes, O., M. Pusch, and F. Morales. 2023. ClC-1 Chloride Channel: Inputs on the Structure-Function  
1003 Relationship of Myotonia Congenita-Causing Mutations. *Biomedicines*. 11.
- 1004 Bykova, E.A., X.D. Zhang, T.Y. Chen, and J. Zheng. 2006. Large movement in the C terminus of CLC-0  
1005 chloride channel during slow gating. *Nat. Struct. Mol. Biol.* 13:1115-1119.
- 1006 Cederholm, J.M., G.Y. Rychkov, C.J. Bagley, and A.H. Bretag. 2010. Inter-subunit communication and  
1007 fast gate integrity are important for common gating in hClC-1. *Int. J. Biochem. Cell Biol.* 42:1182-  
1008 1188.
- 1009 Chavan, T.S., R.C. Cheng, T. Jiang, Mathews, II, R.A. Stein, A. Koehl, H.S. McHaourab, E. Tajkhorshid, and  
1010 M. Maduke. 2020. A CLC-ec1 mutant reveals global conformational change and suggests a  
1011 unifying mechanism for the CLC Cl<sup>-</sup>/H<sup>+</sup> transport cycle. *Elife*. 9.
- 1012 Chovancova, E., A. Pavelka, P. Benes, O. Strnad, J. Brezovsky, B. Kozlikova, A. Gora, V. Sustr, M. Klvana,  
1013 P. Medek, L. Biedermannova, J. Sochor, and J. Damborsky. 2012. CAVER 3.0: a tool for the  
1014 analysis of transport pathways in dynamic protein structures. *PLoS Comput. Biol.* 8:e1002708.
- 1015 Cid, L.P., M.I. Niemeyer, A. Ramirez, and F.V. Sepulveda. 2000. Splice variants of a ClC-2 chloride  
1016 channel with differing functional characteristics. *Am. J. Physiol. Cell Physiol.* 279:C1198-1210.
- 1017 Croll, T.I. 2018. ISOLDE: a physically realistic environment for model building into low-resolution  
1018 electron-density maps. *Acta Crystallogr D Struct Biol.* 74:519-530.
- 1019 De Jesus-Perez, J.J., A. Castro-Chong, R.C. Shieh, C.Y. Hernandez-Carballo, J.A. De Santiago-Castillo, and  
1020 J. Arreola. 2016. Gating the glutamate gate of CLC-2 chloride channel by pore occupancy. *J. Gen.  
1021 Physiol.* 147:25-37.
- 1022 De Jesus-Perez, J.J., G.A. Mendez-Maldonado, A.E. Lopez-Romero, D. Esparza-Jasso, I.L. Gonzalez-  
1023 Hernandez, V. De la Rosa, R. Gastelum-Garibaldi, J.E. Sanchez-Rodriguez, and J. Arreola. 2021.  
1024 Electro-steric opening of the CLC-2 chloride channel gate. *Sci Rep.* 11:13127.
- 1025 de Santiago, J.A., K. Nehrke, and J. Arreola. 2005. Quantitative analysis of the voltage-dependent gating  
1026 of mouse parotid ClC-2 chloride channel. *J. Gen. Physiol.* 126:591-603.
- 1027 Duan, D.D. 2013. Phenomics of cardiac chloride channels. *Compr Physiol.* 3:667-692.

- 1028 Duncan, A.R., M.M. Polovitskaya, H. Gaitan-Penas, S. Bertelli, G.E. VanNoy, P.E. Grant, A. O'Donnell-  
1029 Luria, Z. Valivullah, A.K. Lovgren, E.M. England, E. Agolini, J.A. Madden, K. Schmitz-Abe, A.  
1030 Kritzer, P. Hawley, A. Novelli, P. Alfieri, G.S. Colafati, D. Wiczorek, K. Platzer, J. Luppe, M. Koch-  
1031 Hoglebe, R. Abou Jamra, J. Neira-Fresneda, A. Lehman, C.F. Boerkoel, K. Seath, L. Clarke, C.  
1032 Study, Y. van Ierland, E. Argilli, E.H. Sherr, A. Maiorana, T. Diel, M. Hempel, T. Bierhals, R.  
1033 Estevez, T.J. Jentsch, M. Pusch, and P.B. Agrawal. 2021. Unique variants in CLCN3, encoding an  
1034 endosomal anion/proton exchanger, underlie a spectrum of neurodevelopmental disorders.  
1035 *Am. J. Hum. Genet.* 108:1450-1465.
- 1036 Dutzler, R., E.B. Campbell, M. Cadene, B.T. Chait, and R. MacKinnon. 2002. X-ray structure of a CLC  
1037 chloride channel at 3.0 Å reveals the molecular basis of anion selectivity. *Nature.* 415:287-294.
- 1038 Dutzler, R., E.B. Campbell, and R. MacKinnon. 2003. Gating the selectivity filter in CLC chloride channels.  
1039 *Science.* 300:108-112.
- 1040 Emsley, P., and K. Cowtan. 2004. Coot: model-building tools for molecular graphics. *Acta Crystallogr. D*  
1041 *Biol. Crystallogr.* 60:2126-2132.
- 1042 Ereno-Orbea, J., I. Oyenarte, and L.A. Martinez-Cruz. 2013. CBS domains: Ligand binding sites and  
1043 conformational variability. *Arch. Biochem. Biophys.* 540:70-81.
- 1044 Estevez, R., M. Pusch, C. Ferrer-Costa, M. Orozco, and T.J. Jentsch. 2004. Functional and structural  
1045 conservation of CBS domains from CLC chloride channels. *J. Physiol.* 557:363-378.
- 1046 Feng, L., E.B. Campbell, Y. Hsiung, and R. MacKinnon. 2010. Structure of a eukaryotic CLC transporter  
1047 defines an intermediate state in the transport cycle. *Science.* 330:635-641.
- 1048 Feng, L., E.B. Campbell, and R. MacKinnon. 2012. Molecular mechanism of proton transport in CLC Cl-  
1049 /H+ exchange transporters. *Proc. Natl. Acad. Sci. U. S. A.* 109:11699-11704.
- 1050 Fernandes-Rosa, F.L., G. Daniil, I.J. Orozco, C. Goppner, R. El Zein, V. Jain, S. Boulkroun, X. Jeunemaitre,  
1051 L. Amar, H. Lefebvre, T. Schwarzmayr, T.M. Strom, T.J. Jentsch, and M.C. Zennaro. 2018. A gain-  
1052 of-function mutation in the CLCN2 chloride channel gene causes primary aldosteronism. *Nat.*  
1053 *Genet.* 50:355-361.
- 1054 Furukawa, T., S. Horikawa, T. Terai, T. Ogura, Y. Katayama, and M. Hiraoka. 1995. Molecular cloning  
1055 and characterization of a novel truncated from (CLC-2 beta) of CLC-2 alpha (CLC-2G) in rabbit  
1056 heart. *FEBS. Lett.* 375:56-62.
- 1057 Gaitan-Penas, H., P.M. Apaja, T. Arnedo, A. Castellanos, X. Elorza-Vidal, D. Soto, X. Gasull, G.L. Lukacs,  
1058 and R. Estevez. 2017. Leukoencephalopathy-causing CLCN2 mutations are associated with  
1059 impaired Cl(-) channel function and trafficking. *J. Physiol.* 595:6993-7008.
- 1060 Garcia-Olivares, J., A. Alekov, M.R. Boroumand, B. Begemann, P. Hidalgo, and C. Fahlke. 2008. Gating of  
1061 human CLC-2 chloride channels and regulation by carboxy-terminal domains. *J. Physiol.*  
1062 586:5325-5336.
- 1063 Ganesello, L., D. Del Prete, M. Ceol, G. Priante, L.A. Calo, and F. Anglani. 2020. From protein uptake to  
1064 Dent disease: An overview of the CLCN5 gene. *Gene.* 747:144662.
- 1065 Giorgio, E., G. Vaula, P. Benna, N. Lo Buono, C.M. Eandi, D. Dino, C. Mancini, S. Cavalieri, E. Di Gregorio,  
1066 E. Pozzi, M. Ferrero, M.T. Giordana, C. Depienne, and A. Brusco. 2017. A novel homozygous  
1067 change of CLCN2 (p.His590Pro) is associated with a subclinical form of leukoencephalopathy  
1068 with ataxia (LKPAT). *J. Neurol. Neurosurg. Psychiatry.* 88:894-896.
- 1069 Goehring, A., C.H. Lee, K.H. Wang, J.C. Michel, D.P. Claxton, I. Bacongus, T. Althoff, S. Fischer, K.C.  
1070 Garcia, and E. Gouaux. 2014. Screening and large-scale expression of membrane proteins in  
1071 mammalian cells for structural studies. *Nat. Protoc.* 9:2574-2585.



- 1072 Goppner, C., I.J. Orozco, M.B. Hoegg-Beiler, A.H. Soria, C.A. Hubner, F.L. Fernandes-Rosa, S. Boulkroun,  
1073 M.C. Zennaro, and T.J. Jentsch. 2019. Pathogenesis of hypertension in a mouse model for  
1074 human CLCN2 related hyperaldosteronism. *Nat. Commun.* 10:4678.
- 1075 Grieschat, M., R.E. Guzman, K. Langschwager, C. Fahlke, and A.K. Alekov. 2020. Metabolic energy  
1076 sensing by mammalian CLC anion/proton exchangers. *EMBO Rep.* 21:e47872.
- 1077 Grunder, S., A. Thiemann, M. Pusch, and T.J. Jentsch. 1992. Regions involved in the opening of ClC-2  
1078 chloride channel by voltage and cell volume. *Nature.* 360:759-762.
- 1079 Guo, Z., T. Lu, L. Peng, H. Cheng, F. Peng, J. Li, Z. Lu, S. Chen, and W. Qiu. 2019. CLCN2-related  
1080 leukoencephalopathy: a case report and review of the literature. *BMC Neurol.* 19:156.
- 1081 Hansen, T.H., Y. Yan, G. Ahlberg, O.B. Vad, L. Refsgaard, J.L. Dos Santos, N. Mutsaers, J.H. Svendsen,  
1082 M.S. Olesen, B.H. Bentzen, and N. Schmitt. 2020. A Novel Loss-of-Function Variant in the  
1083 Chloride Ion Channel Gene *Clcn2* Associates with Atrial Fibrillation. *Sci Rep.* 10:1453.
- 1084 Huang, J., and A.D. MacKerell, Jr. 2013. CHARMM36 all-atom additive protein force field: validation  
1085 based on comparison to NMR data. *J Comput Chem.* 34:2135-2145.
- 1086 Humphrey, W., A. Dalke, and K. Schulten. 1996. VMD: visual molecular dynamics. *J. Mol. Graph.* 14:33-  
1087 38, 27-38.
- 1088 Jardetzky, O. 1966. Simple allosteric model for membrane pumps. *Nature.* 211:969-970.
- 1089 Jentsch, T.J., and M. Pusch. 2018. CLC Chloride Channels and Transporters: Structure, Function,  
1090 Physiology, and Disease. *Physiol. Rev.* 98:1493-1590.
- 1091 Jeworutzki, E., T. Lopez-Hernandez, X. Capdevila-Nortes, S. Sirisi, L. Bengtsson, M. Montolio, G. Zifarelli,  
1092 T. Arnedo, C.S. Muller, U. Schulte, V. Nunes, A. Martinez, T.J. Jentsch, X. Gasull, M. Pusch, and R.  
1093 Estevez. 2012. GlialCAM, a Protein Defective in a Leukodystrophy, Serves as a ClC-2 Cl(-)  
1094 Channel Auxiliary Subunit. *Neuron.* 73:951-961.
- 1095 Jordt, S.E., and T.J. Jentsch. 1997. Molecular dissection of gating in the ClC-2 chloride channel. *EMBO J.*  
1096 16:1582-1592.
- 1097 Kieferle, S., P. Fong, M. Bens, A. Vandewalle, and T.J. Jentsch. 1994. Two highly homologous members  
1098 of the ClC chloride channel family in both rat and human kidney. *Proc. Natl. Acad. Sci. U.S.A.*  
1099 91:6943-6947.
- 1100 Koster, A.K., A.L. Reese, Y. Kuryshv, X. Wen, K.A. McKiernan, E.E. Gray, C. Wu, J.R. Huguenard, M.  
1101 Maduke, and J. Du Bois. 2020. Development and validation of a potent and specific inhibitor for  
1102 the CLC-2 chloride channel. *Proc. Natl. Acad. Sci. U. S. A.*
- 1103 Lein, E.S., M.J. Hawrylycz, N. Ao, M. Ayres, A. Bensinger, A. Bernard, A.F. Boe, M.S. Boguski, K.S.  
1104 Brockway, E.J. Byrnes, L. Chen, L. Chen, T.M. Chen, M.C. Chin, J. Chong, B.E. Crook, A.  
1105 Czaplinska, C.N. Dang, S. Datta, N.R. Dee, A.L. Desaki, T. Desta, E. Diep, T.A. Dolbeare, M.J.  
1106 Donelan, H.W. Dong, J.G. Dougherty, B.J. Duncan, A.J. Ebbert, G. Eichele, L.K. Estin, C. Faber,  
1107 B.A. Facer, R. Fields, S.R. Fischer, T.P. Fliss, C. Frensley, S.N. Gates, K.J. Glattfelder, K.R.  
1108 Halverson, M.R. Hart, J.G. Hohmann, M.P. Howell, D.P. Jeung, R.A. Johnson, P.T. Karr, R. Kawal,  
1109 J.M. Kidney, R.H. Knapik, C.L. Kuan, J.H. Lake, A.R. Laramée, K.D. Larsen, C. Lau, T.A. Lemon, A.J.  
1110 Liang, Y. Liu, L.T. Luong, J. Michaels, J.J. Morgan, R.J. Morgan, M.T. Mortrud, N.F. Mosqueda,  
1111 L.L. Ng, R. Ng, G.J. Orta, C.C. Overly, T.H. Pak, S.E. Parry, S.D. Pathak, O.C. Pearson, R.B.  
1112 Puchalski, Z.L. Riley, H.R. Rockett, S.A. Rowland, J.J. Royall, M.J. Ruiz, N.R. Sarno, K. Schaffnit,  
1113 N.V. Shapovalova, T. Sivasay, C.R. Slaughterbeck, S.C. Smith, K.A. Smith, B.I. Smith, A.J. Sodt,  
1114 N.N. Stewart, K.R. Stumpf, S.M. Sunkin, M. Sutram, A. Tam, C.D. Teemer, C. Thaller, C.L.  
1115 Thompson, L.R. Varnam, A. Visel, R.M. Whitlock, P.E. Wohnoutka, C.K. Wolkey, V.Y. Wong, M.  
1116 Wood, M.B. Yaylaoglu, R.C. Young, B.L. Youngstrom, X.F. Yuan, B. Zhang, T.A. Zwingman, and

- 1117 A.R. Jones. 2007. Genome-wide atlas of gene expression in the adult mouse brain. *Nature*.  
1118 445:168-176.
- 1119 Leisle, L., Y. Xu, E. Fortea, S. Lee, J.D. Galpin, M. Vien, C.A. Ahern, A. Accardi, and S. Berneche. 2020.  
1120 Divergent Cl(-) and H(+) pathways underlie transport coupling and gating in CLC exchangers and  
1121 channels. *Elife*. 9.
- 1122 Liebschner, D., P.V. Afonine, M.L. Baker, G. Bunkoczi, V.B. Chen, T.I. Croll, B. Hintze, L.W. Hung, S. Jain,  
1123 A.J. McCoy, N.W. Moriarty, R.D. Oeffner, B.K. Poon, M.G. Prisant, R.J. Read, J.S. Richardson, D.C.  
1124 Richardson, M.D. Sammito, O.V. Sobolev, D.H. Stockwell, T.C. Terwilliger, A.G. Urzhumtsev, L.L.  
1125 Videau, C.J. Williams, and P.D. Adams. 2019. Macromolecular structure determination using X-  
1126 rays, neutrons and electrons: recent developments in Phenix. *Acta Crystallogr D Struct Biol*.  
1127 75:861-877.
- 1128 Liebschner, D., N.W. Moriarty, B.K. Poon, and P.D. Adams. 2023. In situ ligand restraints from quantum-  
1129 mechanical methods. *Acta Crystallogr D Struct Biol*. 79:100-110.
- 1130 Lin, Y.W., C.W. Lin, and T.Y. Chen. 1999. Elimination of the slow gating of ClC-0 chloride channel by a  
1131 point mutation. *J. Gen. Physiol*. 114:1-12.
- 1132 Lisal, J., and M. Maduke. 2008. The ClC-0 chloride channel is a 'broken' Cl-/H+ antiporter. *Nat. Struct.*  
1133 *Mol. Biol*. 15:805-810.
- 1134 Ma, L., G.Y. Rychkov, E.A. Bykova, J. Zheng, and A.H. Bretag. 2011. Movement of hClC-1 C-termini  
1135 during common gating and limits on their cytoplasmic location. *Biochem. J*. 436:415-428.
- 1136 Ma, T., L. Wang, A. Chai, C. Liu, W. Cui, S. Yuan, S. Wing Ngor Au, L. Sun, X. Zhang, Z. Zhang, J. Lu, Y.  
1137 Gao, P. Wang, Z. Li, Y. Liang, H. Vogel, Y.T. Wang, D. Wang, K. Yan, and H. Zhang. 2023. Cryo-EM  
1138 structures of ClC-2 chloride channel reveal the blocking mechanism of its specific inhibitor AK-  
1139 42. *Nat. Commun*. 14:3424.
- 1140 Maduke, M.C., and R.J. Reimer. 2012. Biochemistry to the rescue: a ClC-2 auxiliary subunit provides a  
1141 tangible link to leukodystrophy. *Neuron*. 73:855-857.
- 1142 Miller, C. 1982. Open-state substructure of single chloride channels from Torpedo electroplax. *Philos.*  
1143 *Trans. R. Soc. Lond. B. Biol. Sci*. 299:401-411.
- 1144 Miller, C. 2006. ClC chloride channels viewed through a transporter lens. *Nature*. 440:484-489.
- 1145 Miller, C. 2021. Q-cubed mutant cues clues to CLC antiport mechanism. *J. Gen. Physiol*. 153.
- 1146 Morozenko, A., and A.A. Stuchebrukhov. 2016. Dowser++, a new method of hydrating protein  
1147 structures. *Proteins*. 84:1347-1357.
- 1148 Nicoli, E.R., M.R. Weston, M. Hackbarth, A. Becerril, A. Larson, W.M. Zein, P.R. Baker, 2nd, J.D. Burke,  
1149 H. Dorward, M. Davids, Y. Huang, D.R. Adams, P.M. Zerfas, D. Chen, T.C. Markello, C. Toro, T.  
1150 Wood, G. Elliott, M. Vu, N. Undiagnosed Diseases, W. Zheng, L.J. Garrett, C.J. Tifft, W.A. Gahl,  
1151 D.L. Day-Salvatore, J.A. Mindell, and M.C.V. Malicdan. 2019. Lysosomal Storage and Albinism  
1152 Due to Effects of a De Novo CLCN7 Variant on Lysosomal Acidification. *Am. J. Hum. Genet*.  
1153 104:1127-1138.
- 1154 Niemeyer, M.I., L.P. Cid, Y.R. Yusef, R. Briones, and F.V. Sepulveda. 2009. Voltage-dependent and -  
1155 independent titration of specific residues accounts for complex gating of a ClC chloride channel  
1156 by extracellular protons. *J. Physiol*. 587:1387-1400.
- 1157 Niemeyer, M.I., L.P. Cid, L. Zuniga, M. Catalan, and F.V. Sepulveda. 2003. A conserved pore-lining  
1158 glutamate as a voltage- and chloride-dependent gate in the ClC-2 chloride channel. *J. Physiol*.  
1159 553:873-879.

- 1160 Nighot, P.K., L. Leung, and T.Y. Ma. 2017. Chloride channel CLC- 2 enhances intestinal epithelial tight  
1161 junction barrier function via regulation of caveolin-1 and caveolar trafficking of occludin. *Exp.*  
1162 *Cell Res.* 352:113-122.
- 1163 Nishikawa, K.O., T.; Isogai, Y.; Saitô, N. 1972. Tertiary Structure of Proteins. I. Representation and  
1164 Computation of the Conformations. *Journal of the physical society of Japan.* 32.
- 1165 Okamoto, Y., Y. Nagasawa, Y. Obara, K. Ishii, D. Takagi, and K. Ono. 2019. Molecular identification of  
1166 HSPA8 as an accessory protein of a hyperpolarization-activated chloride channel from rat  
1167 pulmonary vein cardiomyocytes. *J. Biol. Chem.* 294:16049-16061.
- 1168 Palmer, E.E., M. Pusch, A. Picollo, C. Forwood, M.H. Nguyen, V. Suckow, J. Gibbons, A. Hoff, L. Sigfrid, A.  
1169 Megarbane, M. Nizon, B. Cogne, C. Beneteau, F.S. Alkuraya, A. Chedrawi, M.O. Hashem, H.  
1170 Stamberger, S. Weckhuysen, A. Vanlander, B. Ceulemans, S. Rajagopalan, K. Nunn, S. Arpin, M.  
1171 Raynaud, C.S. Motter, C. Ward-Melver, K. Janssens, M. Meuwissen, D. Beysen, N. Dikow, M.  
1172 Grimmel, T.B. Haack, E. Clement, A. McTague, D. Hunt, S. Townshend, M. Ward, L.J. Richards, C.  
1173 Simons, G. Costain, L. Dupuis, R. Mendoza-Londono, T. Dudding-Byth, J. Boyle, C. Saunders, E.  
1174 Fleming, S. El Chehadeh, M.A. Spitz, A. Piton, B. Gerard, M.T. Abi Warde, G. Rea, C. McKenna, S.  
1175 Douzgou, S. Banka, C. Akman, J.M. Bain, T.T. Sands, G.N. Wilson, E.J. Silvertooth, L. Miller, D.  
1176 Lederer, R. Sachdev, R. Macintosh, O. Monestier, D. Karadurmus, F. Collins, M. Carter, L.  
1177 Rohena, M.H. Willemsen, C.W. Ockeloen, R. Pfundt, S.D. Kroft, M. Field, F.E.R. Laranjeira, A.M.  
1178 Fortuna, A.R. Soares, V. Michaud, S. Naudion, S. Golla, D.D. Weaver, L.M. Bird, J. Friedman, V.  
1179 Clowes, S. Joss, L. Polsler, P.M. Campeau, M. Blazo, E.K. Bijlsma, J.A. Rosenfeld, C. Beetz, Z.  
1180 Powis, K. McWalter, T. Brandt, E. Torti, M. Mathot, S.S. Mohammad, R. Armstrong, and V.M.  
1181 Kalscheuer. 2023. Functional and clinical studies reveal pathophysiological complexity of  
1182 CLCN4-related neurodevelopmental condition. *Mol. Psychiatry.* 28:668-697.
- 1183 Park, E., E.B. Campbell, and R. MacKinnon. 2017. Structure of a CLC chloride ion channel by cryo-  
1184 electron microscopy. *Nature.* 541:500-505.
- 1185 Park, E., and R. MacKinnon. 2018. Structure of the CLC-1 chloride channel from Homo sapiens. *Elife.* 7.
- 1186 Park, K., J. Arreola, T. Begenisich, and J.E. Melvin. 1998. Comparison of voltage-activated Cl<sup>-</sup> channels in  
1187 rat parotid acinar cells with CLC-2 in a mammalian expression system. *J. Membr. Biol.* 163:87-95.
- 1188 Paul, J., S. Jeyaraj, S.M. Huber, G. Seebohm, C. Bohmer, F. Lang, P.G. Kreamsner, and J.F. Kun. 2007.  
1189 Alterations in the cytoplasmic domain of CLCN2 result in altered gating kinetics. *Cell. Physiol.*  
1190 *Biochem.* 20:441-454.
- 1191 Pettersen, E.F., T.D. Goddard, C.C. Huang, G.S. Couch, D.M. Greenblatt, E.C. Meng, and T.E. Ferrin.  
1192 2004. UCSF Chimera--a visualization system for exploratory research and analysis. *J Comput*  
1193 *Chem.* 25:1605-1612.
- 1194 Picollo, A., M. Malvezzi, J.C. Houtman, and A. Accardi. 2009. Basis of substrate binding and  
1195 conservation of selectivity in the CLC family of channels and transporters. *Nat. Struct. Mol. Biol.*  
1196 16:1294-1301.
- 1197 Pintilie, G., K. Zhang, Z. Su, S. Li, M.F. Schmid, and W. Chiu. 2020. Measurement of atom resolvability in  
1198 cryo-EM maps with Q-scores. *Nat. Methods.* 17:328-334.
- 1199 Pusch, M., S. Jordt, V. Stein, and T.J. Jentsch. 1999. Chloride dependence of hyperpolarization-activated  
1200 chloride channel gates. *J. Physiol.* 515:341-353.
- 1201 Pusch, M., U. Ludewig, and T.J. Jentsch. 1997. Temperature dependence of fast and slow gating  
1202 relaxations of CLC-0 chloride channels. *J. Gen. Physiol.* 109:105-116.
- 1203 Pusch, M., U. Ludewig, A. Rehfeldt, and T.J. Jentsch. 1995. Gating of the voltage-dependent chloride  
1204 channel CLC-0 by the permeant anion. *Nature.* 373:527-531.

- 1205 Roe, D.R., and T.E. Cheatham, 3rd. 2013. PTRAJ and CPPTRAJ: Software for Processing and Analysis of  
1206 Molecular Dynamics Trajectory Data. *Journal of chemical theory and computation*. 9:3084-3095.
- 1207 Saint-Martin, C., G. Gauvain, G. Teodorescu, I. Gourfinkel-An, E. Fedirko, Y.G. Weber, S. Maljevic, J.P.  
1208 Ernst, J. Garcia-Olivares, C. Fahlke, R. Nabbout, E. LeGuern, H. Lerche, J.C. Poncer, and C.  
1209 Depienne. 2009. Two novel CLCN2 mutations accelerating chloride channel deactivation are  
1210 associated with idiopathic generalized epilepsy. *Hum. Mutat.* 30:397-405.
- 1211 Salomon-Ferrer, R., A.W. Gotz, D. Poole, S. Le Grand, and R.C. Walker. 2013. Routine Microsecond  
1212 Molecular Dynamics Simulations with AMBER on GPUs. 2. Explicit Solvent Particle Mesh Ewald.  
1213 *Journal of chemical theory and computation*. 9:3878-3888.
- 1214 Sanchez-Rodriguez, J.E., J.A. De Santiago-Castillo, and J. Arreola. 2010. Permeant anions contribute to  
1215 voltage dependence of CLC-2 chloride channel by interacting with the protopore gate. *J. Physiol.*  
1216 588:2545-2556.
- 1217 Sanchez-Rodriguez, J.E., J.A. De Santiago-Castillo, J.A. Contreras-Vite, P.G. Nieto-Delgado, A. Castro-  
1218 Chong, and J. Arreola. 2012. Sequential interaction of chloride and proton ions with the fast  
1219 gate steer the voltage-dependent gating in CLC-2 chloride channels. *J. Physiol.* 590:4239-4253.
- 1220 Scholl, U.I., G. Stolting, J. Schewe, A. Thiel, H. Tan, C. Nelson-Williams, A.A. Vichot, S.C. Jin, E. Loring, V.  
1221 Untiet, T. Yoo, J. Choi, S. Xu, A. Wu, M. Kirchner, P. Mertins, L.C. Rump, A.M. Onder, C. Gamble,  
1222 D. McKenney, R.W. Lash, D.P. Jones, G. Chune, P. Gagliardi, M. Choi, R. Gordon, M. Stowasser,  
1223 C. Fahlke, and R.P. Lifton. 2018. CLCN2 chloride channel mutations in familial  
1224 hyperaldosteronism type II. *Nat. Genet.* 50:349-354.
- 1225 Schrecker, M., J. Korobenko, and R.K. Hite. 2020. Cryo-EM structure of the lysosomal chloride-proton  
1226 exchanger CLC-7 in complex with OSTM1. *Elife*. 9.
- 1227 Sepela, R.J., and J.T. Sack. 2018. Taming unruly chloride channel inhibitors with rational design. *Proc.*  
1228 *Natl. Acad. Sci. U. S. A.* 115:5311-5313.
- 1229 Steinmeyer, K., C. Ortland, and T.J. Jentsch. 1991. Primary structure and functional expression of a  
1230 developmentally regulated skeletal muscle chloride channel. *Nature*. 354:301-304.
- 1231 Stolting, G., M. Fischer, and C. Fahlke. 2014. CLC channel function and dysfunction in health and  
1232 disease. *Front Physiol.* 5:378.
- 1233 Stolting, G., G. Teodorescu, B. Begemann, J. Schubert, R. Nabbout, M.R. Toliat, T. Sander, P. Nurnberg,  
1234 H. Lerche, and C. Fahlke. 2013. Regulation of CLC-2 gating by intracellular ATP. *Pflugers Arch.*  
1235 465:1423-1437.
- 1236 Suomivuori, C.M., N.R. Latorraca, L.M. Wingler, S. Eismann, M.C. King, A.L.W. Kleinhenz, M.A. Skiba,  
1237 D.P. Staus, A.C. Kruse, R.J. Lefkowitz, and R.O. Dror. 2020. Molecular mechanism of biased  
1238 signaling in a prototypical G protein-coupled receptor. *Science*. 367:881-887.
- 1239 Thiemann, A., S. Grunder, M. Pusch, and T.J. Jentsch. 1992. A chloride channel widely expressed in  
1240 epithelial and non-epithelial cells. *Nature*. 356:57-60.
- 1241 Varela, D., M.I. Niemeyer, L.P. Cid, and F.V. Sepulveda. 2002. Effect of an N-terminus deletion on  
1242 voltage-dependent gating of the CLC-2 chloride channel. *J. Physiol.* 544:363-372.
- 1243 Wang, H., M. Xu, Q. Kong, P. Sun, F. Yan, W. Tian, and X. Wang. 2017. Research and progress on CLC2  
1244 (Review). *Mol Med Rep.* 16:11-22.
- 1245 Wang, K., S.S. Preisler, L. Zhang, Y. Cui, J.W. Missel, C. Gronberg, K. Gotfryd, E. Lindahl, M. Andersson,  
1246 K. Calloe, P.F. Egea, D.A. Klaerke, M. Pusch, P.A. Pedersen, Z.H. Zhou, and P. Gourdon. 2019.  
1247 Structure of the human CLC-1 chloride channel. *PLoS Biol.* 17:e3000218.
- 1248 Xu, P., Z. Chen, J. Ma, Y. Shan, Y. Wang, B. Xie, D. Zheng, F. Guo, X. Song, G. Gao, K. Ye, Y. Liu, G. Pan, B.  
1249 Jiang, F. Peng, and X. Zhong. 2023. Biallelic CLCN2 mutations cause retinal degeneration by

1250           impairing retinal pigment epithelium phagocytosis and chloride channel function. *Hum. Genet.*  
1251           142:577-593.

1252 Yamada, T., M. Krzeminski, Z. Bozoky, J.D. Forman-Kay, and K. Strange. 2016. Role of CBS and Bateman  
1253           Domains in Phosphorylation-Dependent Regulation of a CLC Anion Channel. *Biophys. J.*  
1254           111:1876-1886.

1255 Yusef, Y.R., L. Zuniga, M. Catalan, M.I. Niemeyer, L.P. Cid, and F.V. Sepulveda. 2006. Removal of gating  
1256           in voltage-dependent CLC-2 chloride channel by point mutations affecting the pore and C-  
1257           terminus CBS-2 domain. *J. Physiol.* 572:173-181.

1258 Zagotta, W.N., T. Hoshi, and R.W. Aldrich. 1990. Restoration of inactivation in mutants of Shaker  
1259           potassium channels by a peptide derived from ShB [see comments]. *Science.* 250:568-571.

1260 Zifarelli, G. 2022. The Role of the Lysosomal Cl(-)/H(+) Antiporter CLC-7 in Osteopetrosis and  
1261           Neurodegeneration. *Cells.* 11.

1262 Zuniga, L., M.I. Niemeyer, D. Varela, M. Catalan, L.P. Cid, and F.V. Sepulveda. 2004. The voltage-  
1263           dependent CLC-2 chloride channel has a dual gating mechanism. *J. Physiol.* 555:671-682.  
1264

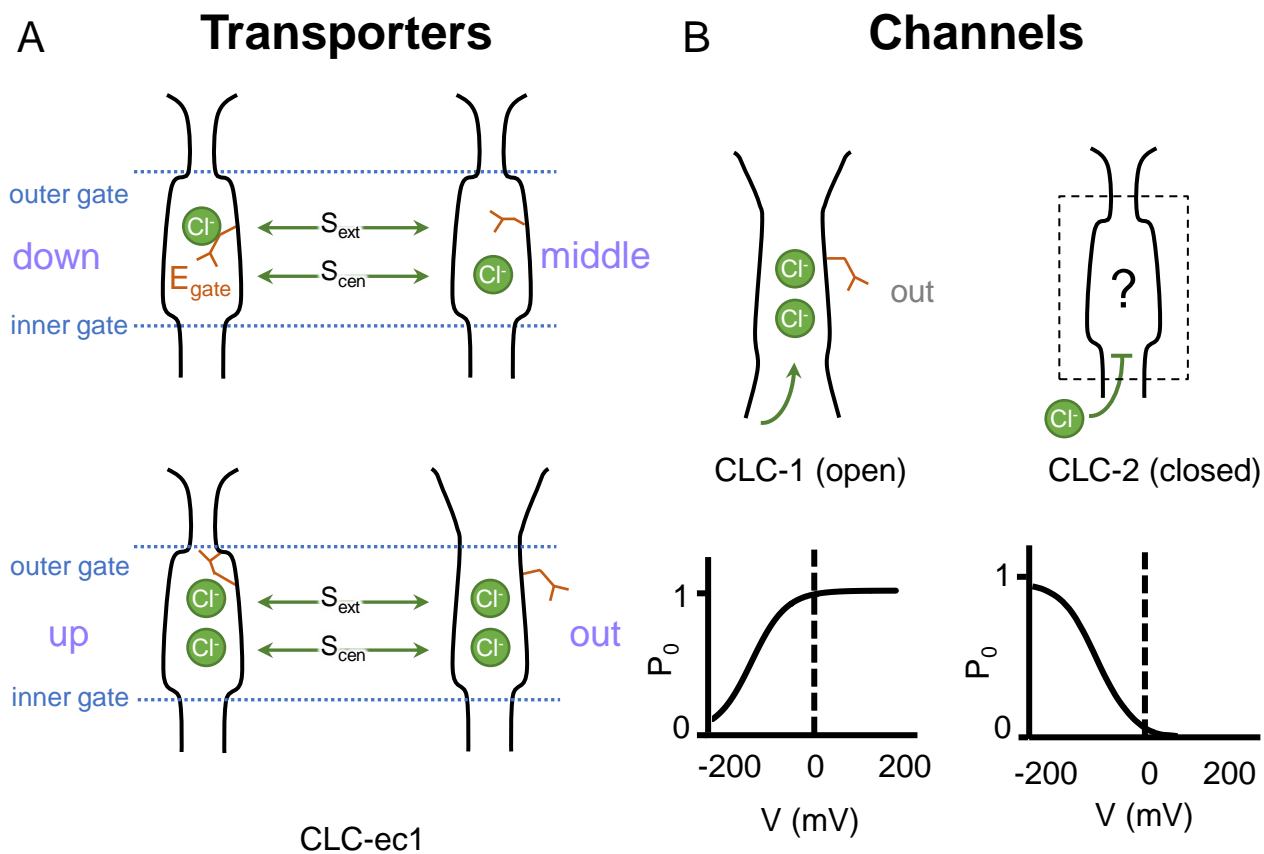


**Figure 1. Gating conformations in CLC transporters and channels.** (A) Cartoon depictions of the CLC anion-permeation pathway. The “gating glutamate” ( $E_{gate}$ ) can occupy anion binding sites within the permeation pathway (“down” and “middle” conformations, occupying the central ( $S_{cen}$ ) and external ( $S_{ext}$ ) anion-binding sites respectively) or away from these sites (“up” and “out” conformations). Coupling of  $E_{gate}$  movement to  $Cl^-/H^+$  binding/unbinding and global conformational change generates 2:1  $Cl^-/H^+$  exchange. (B)  $E_{gate}$  is required for voltage-dependent gating in CLC channels but has been observed structurally only in CLC-1 (PDB ID: 6coy), in the “out” position. In contrast to CLC-1, which is predominantly open at zero mV, CLC-2 is predominantly closed. The open probability ( $P_o$ ) versus voltage ( $V$ ) traces are based on published data reported for CLC-1 (Lisal and Maduke, 2008) and CLC-2 (Stolting et al., 2013).



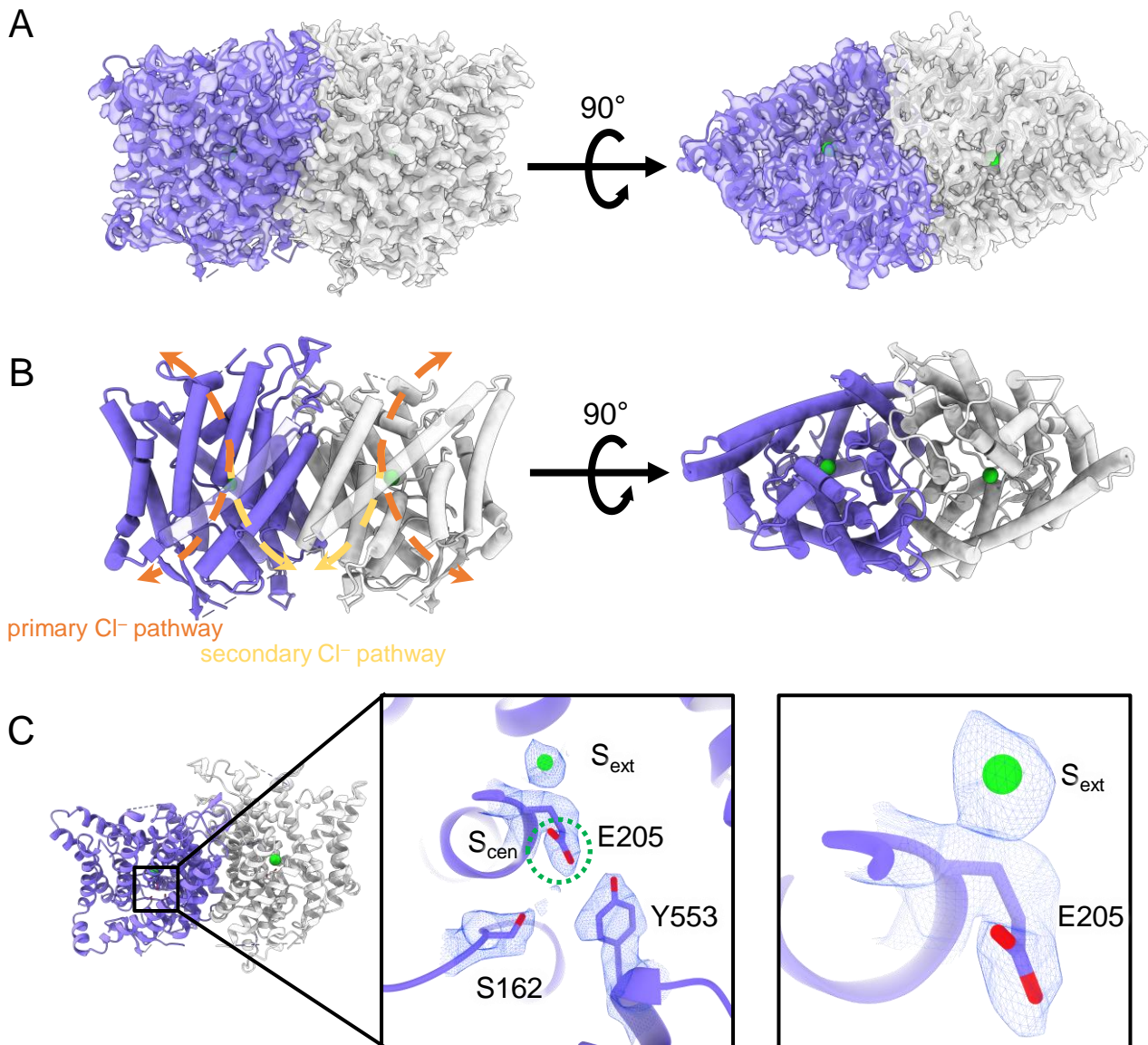


**Figure 2. CryoEM structure of the human CLC-2 channel.** Overall structure of the transmembrane domain (“CLC2-TM”) at 2.46 Å. The identical subunits of the homodimer are shown in purple and gray, Cl<sup>-</sup> ions are shown as green balls. **(A)** cryoEM density map with model overlay (contour level: 0.71, 5.5  $\sigma$ ) and **(B)** model only with dashed arrows indicating the locations of pathways detected by Caver: orange, primary Cl<sup>-</sup> pathway common to all CLCs; yellow, secondary Cl<sup>-</sup> pathway detected in CLC-2 and CLC-1. Details of the pathways are presented in Figure 3. The secondary pathway, whose function is not yet known, was so named when first observed in the CLC-1 structure (Park and MacKinnon, 2018). **(C)** Zoomed-in views showing cryoEM density overlay of bound Cl<sup>-</sup> and key residues – E<sub>gate</sub> (E205) and inner-gate residues Ser<sub>C</sub> (S162) and Tyr<sub>C</sub> (Y553). S<sub>cen</sub> is indicated with a green dashed circle. Contour level: 1.1, 7.2  $\sigma$  (middle panel); 0.97, 6.3  $\sigma$  (right panel).



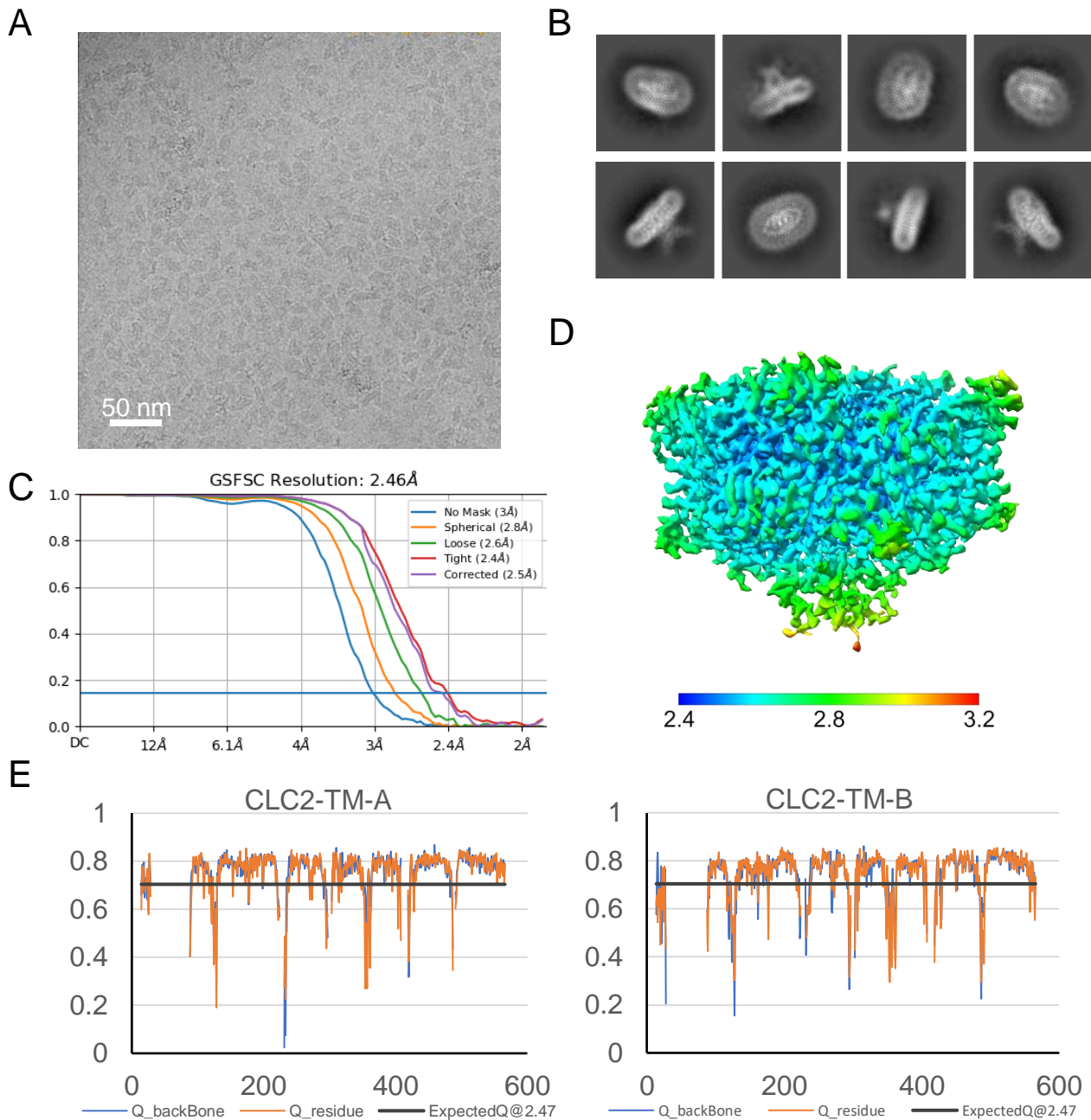


**Figure 2 - figure supplement 1. Micrograph and 2D classes and structure validation of CLC2-TM.** (A) Representative motion-corrected cryo-EM micrograph. (B) 2D class averages. (C) Gold standard FSC plots calculated in cryoSPARC. (D) Local resolution of the cryo-EM map of the CLC2-TM. (E) Model validation using Q-scores (Pintilie et al., 2020) of subunit A (left) and subunit B (right). The black line represents the expected Q-score at respective resolution based on the correlation between Q-scores and map resolution.

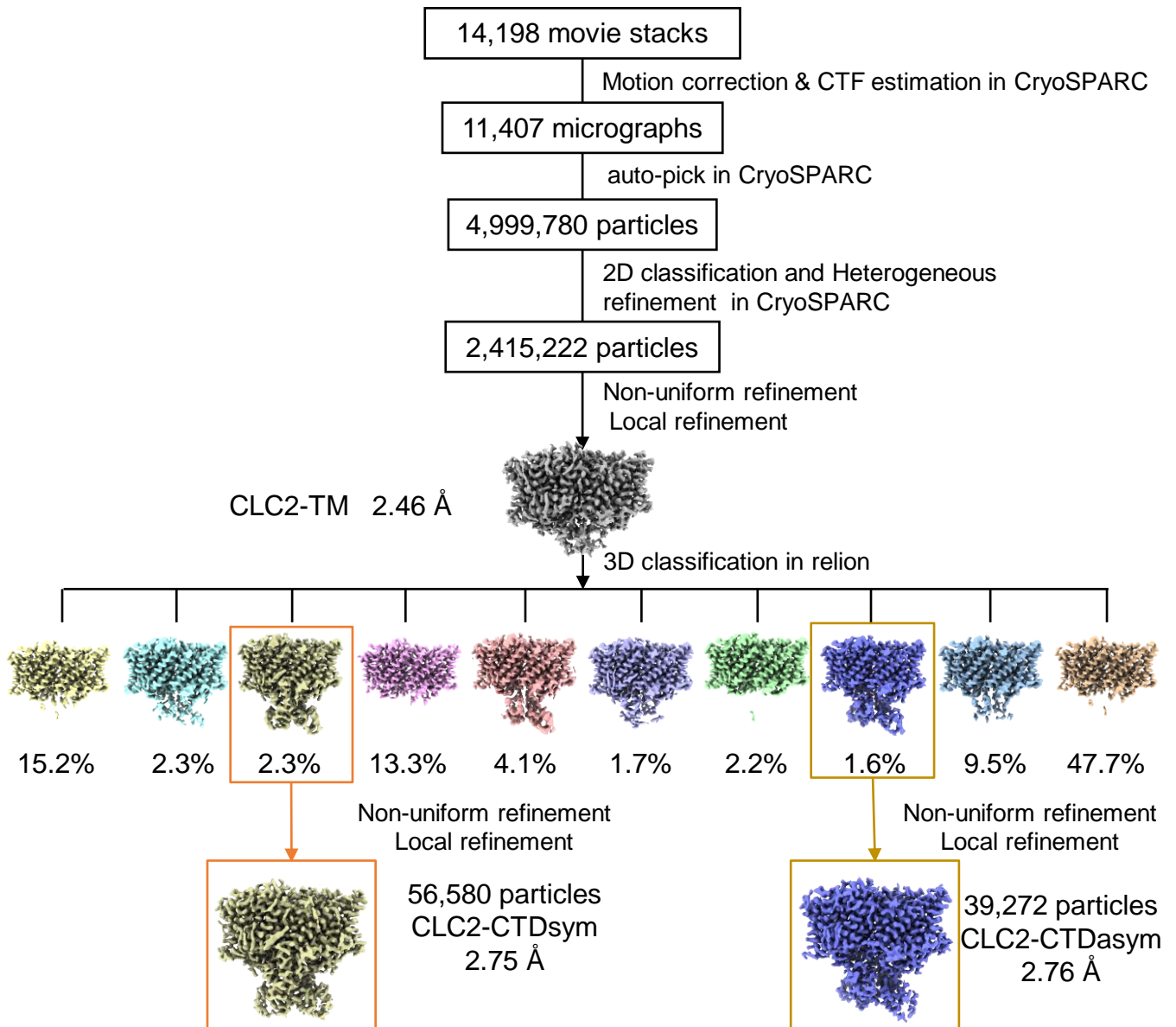


**Figure 2 - figure supplement 2. CryoEM workflow of the CLC2 single-particle cryoEM data processing.** A total of 14,198 movie stacks were collected on a 300 kV Titan Krios cryo-electron microscope. cryoSPARC was used for 2D classification, and the CLC2-TM density map was obtained after 2D classification. Relion was used for 3D classification and yielded two conformations differing in the CTD: CLC2-CTD<sub>sym</sub> and CLC2-CTD<sub>asym</sub>. Resolutions shown refer to the whole protein molecule.

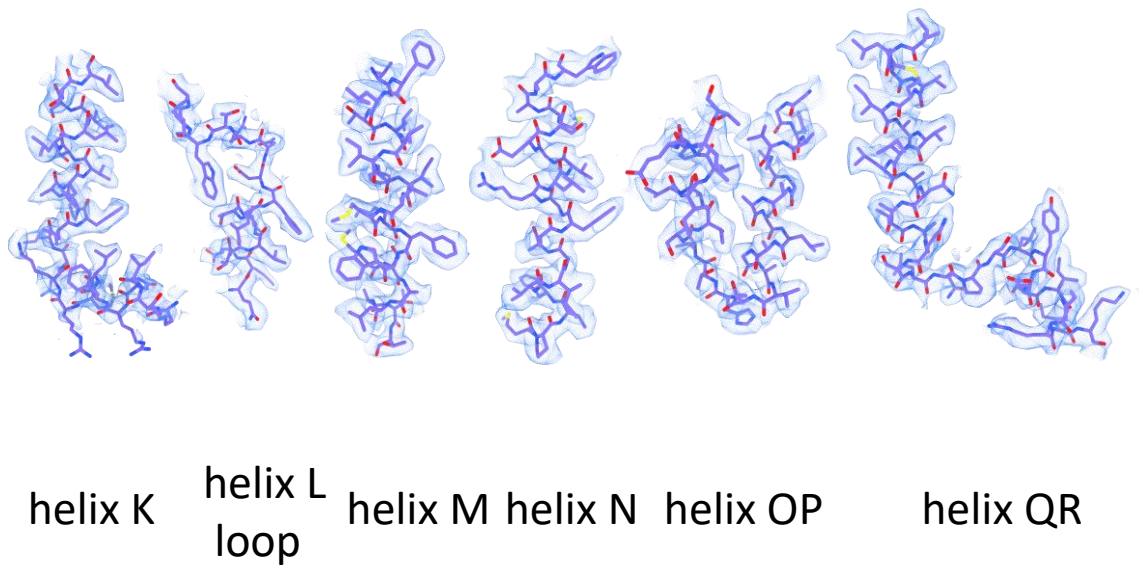
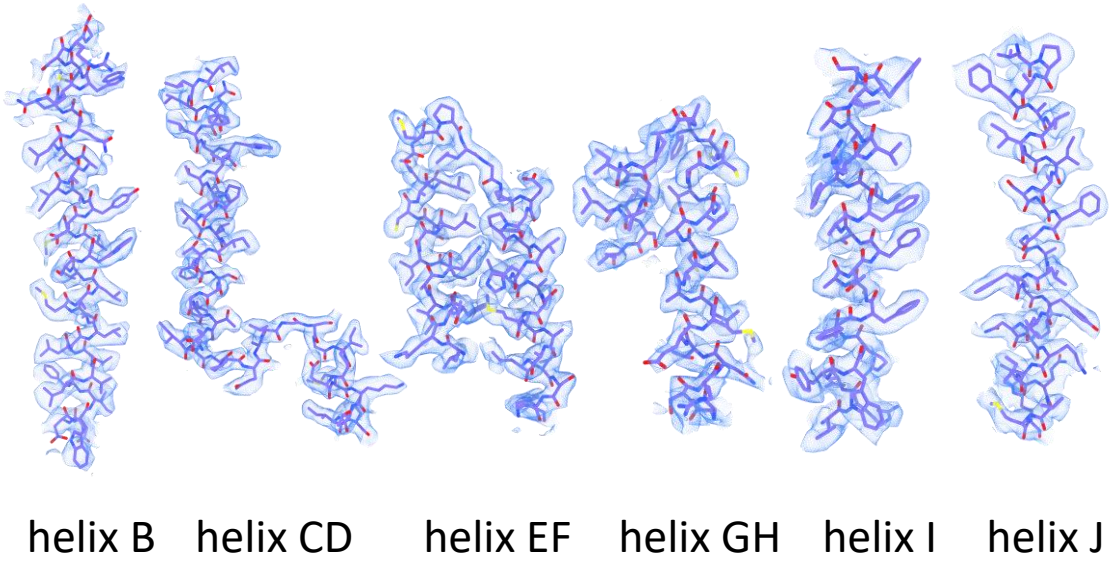


**Figure 2 - figure supplement 3. Helix map of CLC2-TM.** cryo-EM densities and model of CLC-2 transmembrane helices.

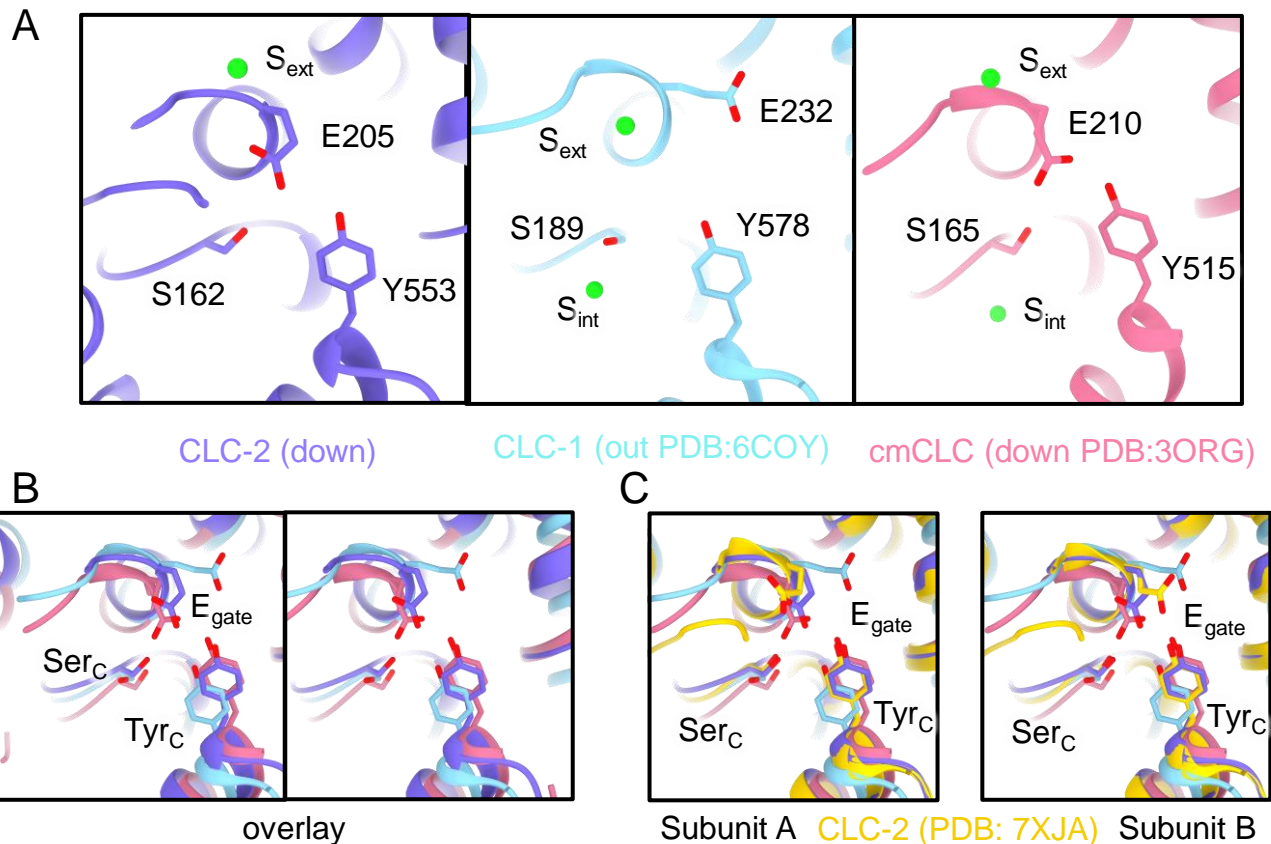


**Figure 2 - figure supplement 4.  $E_{\text{gate}}$  position and  $\text{Cl}^-$  binding sites ( $S_{\text{ext}}$  and  $S_{\text{cen}}$ ).** (A) Comparison between CLC-2 (purple), CLC-1 (light blue), and cmCLC (salmon pink).  $E_{\text{gate}}$  (E205 in CLC-2, E232 in CLC-1, and E210 in cmCLC),  $\text{Ser}_C$  (S162 in CLC2, S189 in CLC-1, and S165 in cmCLC) and  $\text{Tyr}_C$  (Y553 in CLC-2, Y578 in CLC-1, and Y515 in cmCLC) are shown as sticks. In CLC-2 and cmCLC,  $S_{\text{ext}}$  is occupied by  $\text{Cl}^-$ , and  $S_{\text{cen}}$  is occupied by  $E_{\text{gate}}$ .  $E_{\text{gate}}$  is in the “down” position. In CLC-1,  $S_{\text{ext}}$  is occupied by  $\text{Cl}^-$ , and  $S_{\text{cen}}$  lacks anion density.  $E_{\text{gate}}$  is in the “out” position, away from the  $\text{Cl}^-$ -permeation pathway. (B) Overlay view (stereo) of panel A. (C) Overlay with the CLC-2  $E_{\text{gate}}$  conformations modeled in PDB ID: 7XJA (Ma et al., 2023).



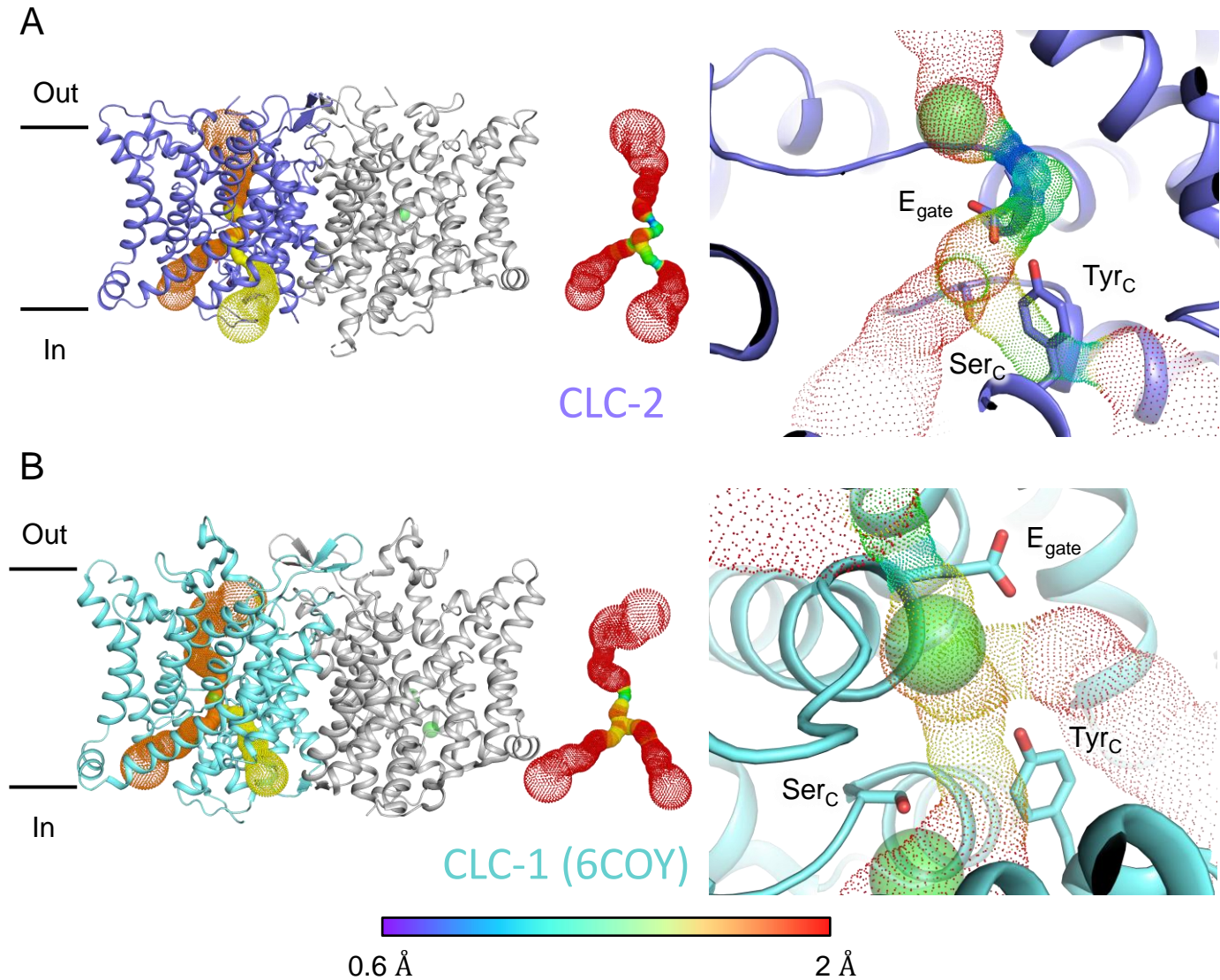


**Figure 3** Pore profile detected in CLC-2. **(A)** Left: The primary (orange) and secondary (yellow) pore detected in CLC-2 using Caver. Middle: The detected pore radii are displayed in dots as a color map. Right: Zoomed-in view of the restricted (narrowest) site of the pore profile, using the same coloring as in the middle panel.  $E_{gate}$ ,  $Ser_C$  and  $Tyr_C$  are shown as sticks. **(B)** Pore profile for CLC-1 (PDB ID:6coy), with display as in panel **A**.

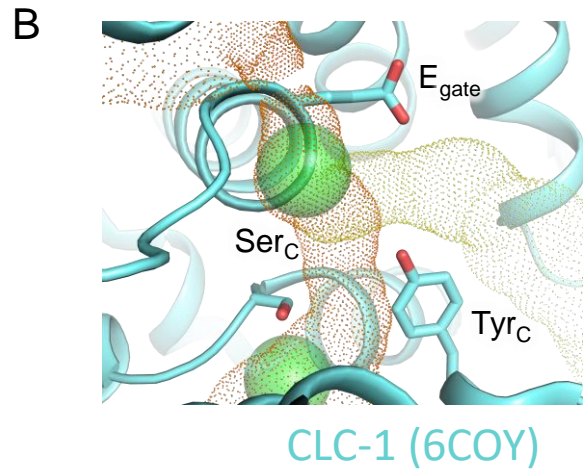
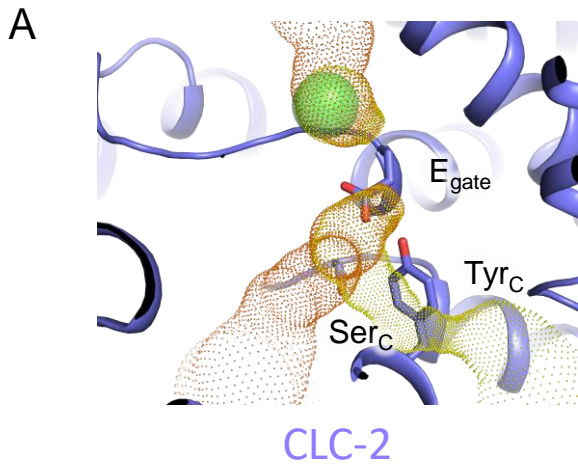


**Figure 3 - figure supplement 1. Cl<sup>-</sup> pathway in CLC-2 and CLC-1.** (A) CLC-2 Cl<sup>-</sup> pathway as shown in Figure 3 but omitting sections with pore radius less than 1 Å. E<sub>gate</sub>, occupying the S<sub>cen</sub> site, blocks the canonical Cl<sup>-</sup> pathway. (B) same as panel A, for CLC-1 (PDB ID:6coy).

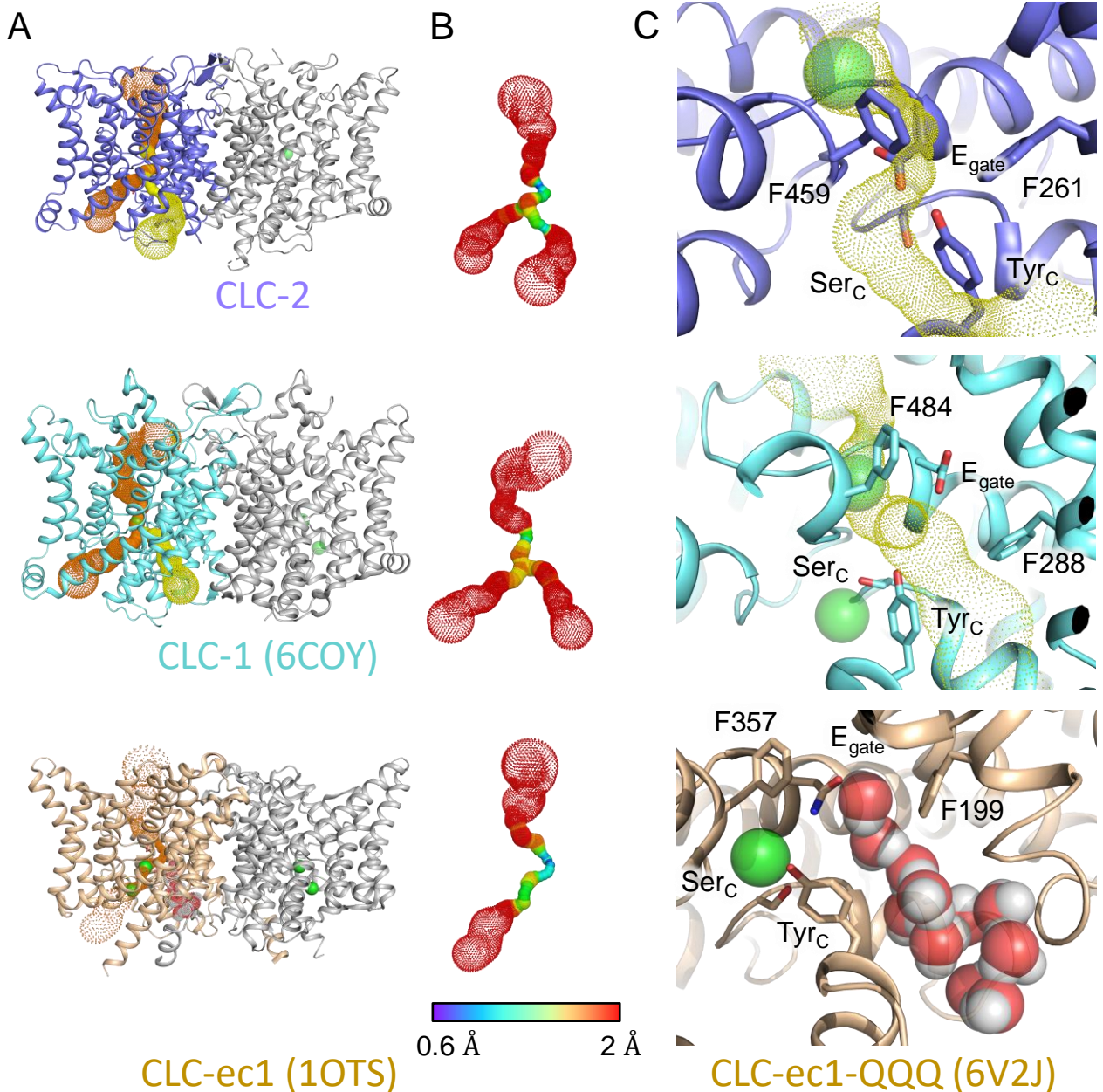


**Figure 3 - figure supplement 2. Comparison of primary and secondary Cl<sup>-</sup> pathways with transporter Cl<sup>-</sup> and H<sup>+</sup> pathways.** (A) The top two panels are repeated from Figure 3A, indicating the primary (orange) and secondary (yellow) cover-detected pores in CLC-1 and CLC-2. The lower panel shows CLC-ec1 (PDB ID: 1OTS), a representative for the CLC transporters, where cover detects only the primary pore (orange dots as for CLC-1 and CLC-2). (B) Detected pore radii show a longer constriction in the CLC-ec1 transporter compared to the CLC-1 and CLC-2 channels. (C) Zoomed-in view of the secondary-pore region for CLC-2 (top), CLC-1 (middle) and CLC-ec1 (bottom). The CLC-ec1 panel shows water wires (space-filled) detected in simulations of the QQQ mutant structure (PDB ID: 6V2J) (Chavan et al., 2020).



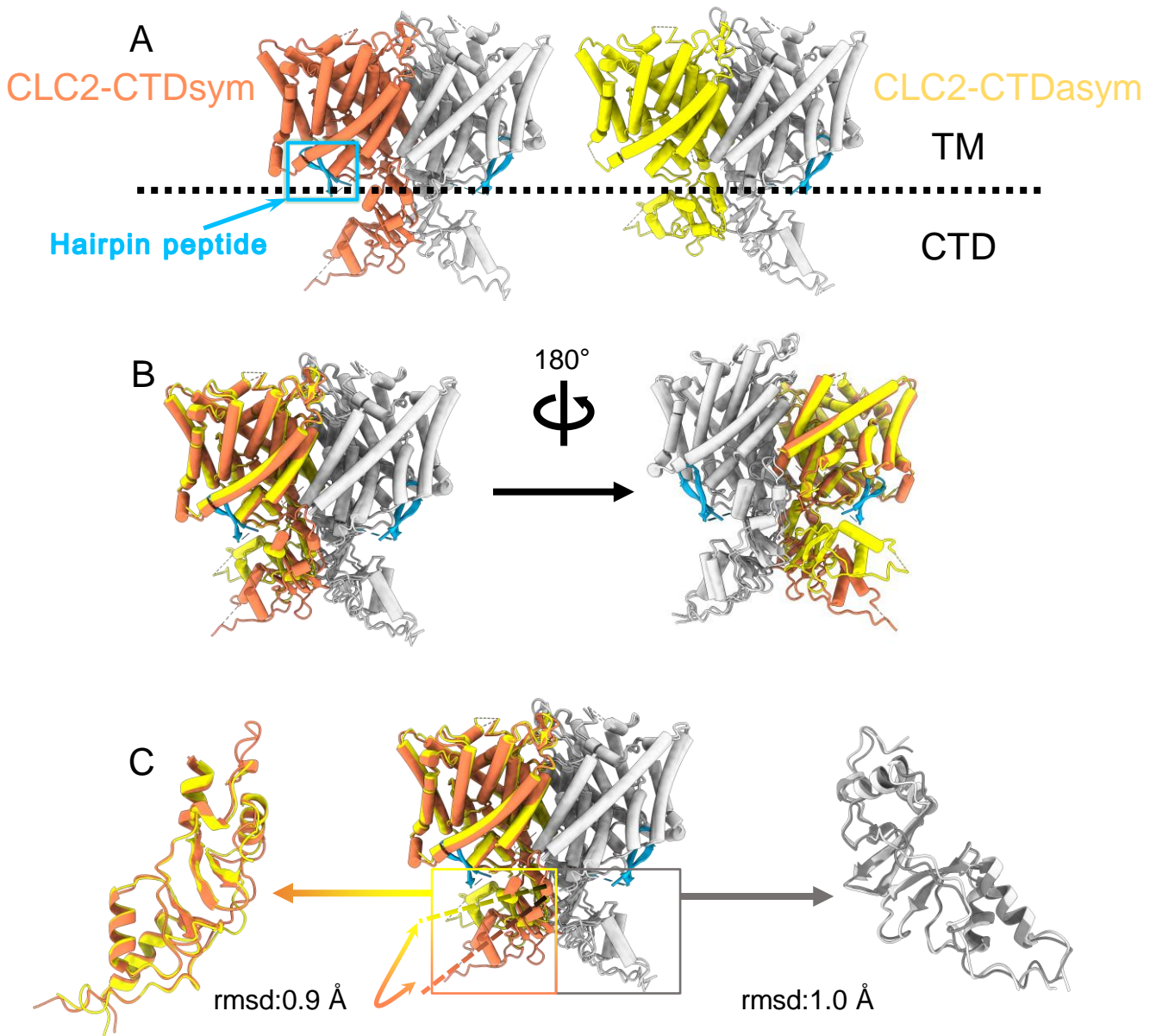


**Figure 4. Different conformations of the CTD.** (A). Overall structure of the two CLC-2 conformations. Left: CLC2-CTD<sub>sym</sub> at 2.75 Å. Right: CLC2-CTD<sub>asym</sub> at 2.76 Å. The subunits of the homodimer are shown in orange (CLC2-CTD<sub>sym</sub>) or yellow (CLC2-CTD<sub>asym</sub>) and gray (for both). The subunits adopting different CTD conformations are shown in orange and yellow, while the subunits sharing the same CTD conformation are shown in gray. The dashed line demarcates the transmembrane (TM) and cytoplasmic (CTD) domains. A hairpin structure detected at the intracellular pore is shown in blue. (B) Overlay of two conformations. (C) Hinge movement of the CTD between two conformations. The middle panel shows an overlay of CLC2-CTD<sub>sym</sub> (orange and gray) and CLC1-CTD<sub>asym</sub> (yellow and gray), with the CTDs highlighted in boxes. For the subunits that adopt different conformations (orange and yellow), the double-headed arrow indicates the change between the two conformations. The RMSD between the subunits shown in orange/yellow is 6.9 Å, while the RMSD for the subunits shown in gray is only 1.3 Å. Alignments of only the CTDs are shown at left and right; in these alignments, the low RMSD values (0.9 Å and 1.0 Å, respectively) indicate that the CTDs undergo a hinge movement.

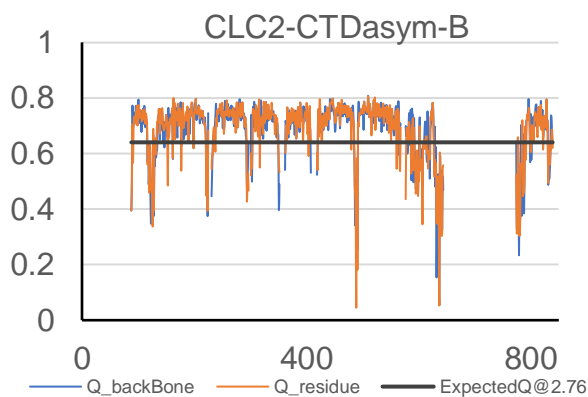
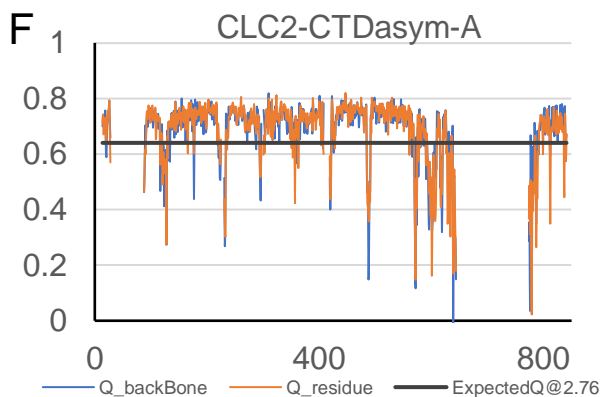
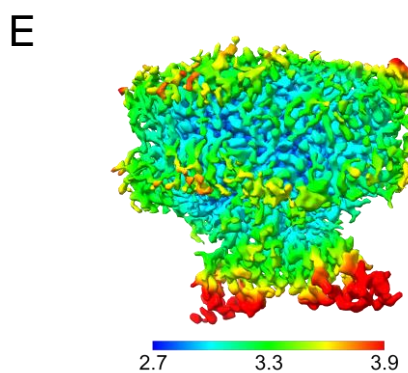
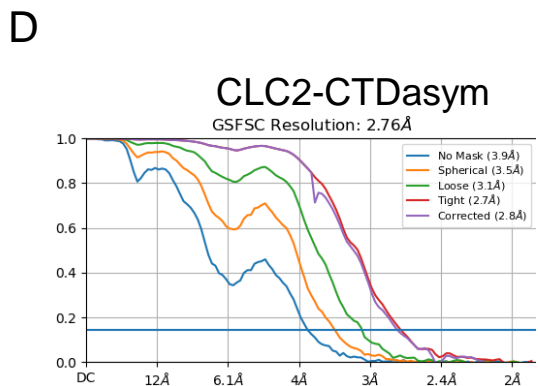
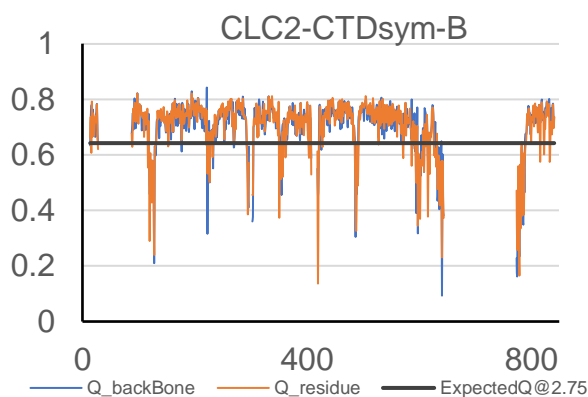
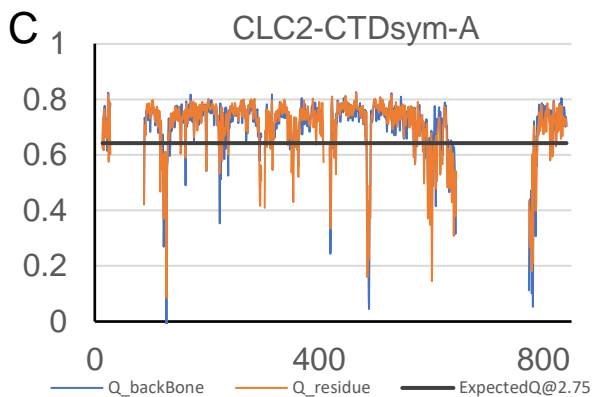
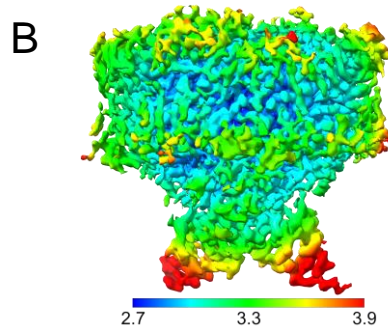
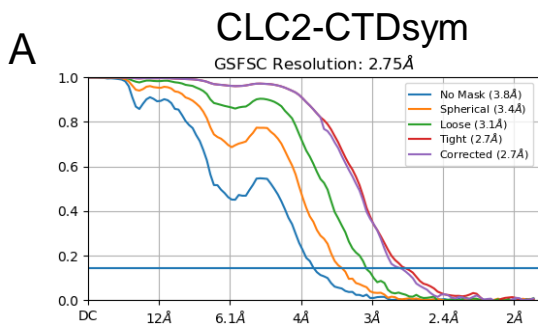


**Figure 4 - figure supplement 1. Structure validation of CLC2-CTDsym and CLC2-CTDasym. (A)** Gold standard FSC plots calculated in cryoSPARC for CLC2-CTDsym. **(B)** Local resolution of the cryo-EM map of the CLC2-CTDsym. **(C)** Model validation using Q-scores of subunit A (left) and subunit B (right) of CLC2-CTDsym. The black line represents the expected Q-score at respective resolution based on the correlation between Q-scores and map resolution. **(D-F)** the same as **(A-C)** for CLC2-CTDasym.

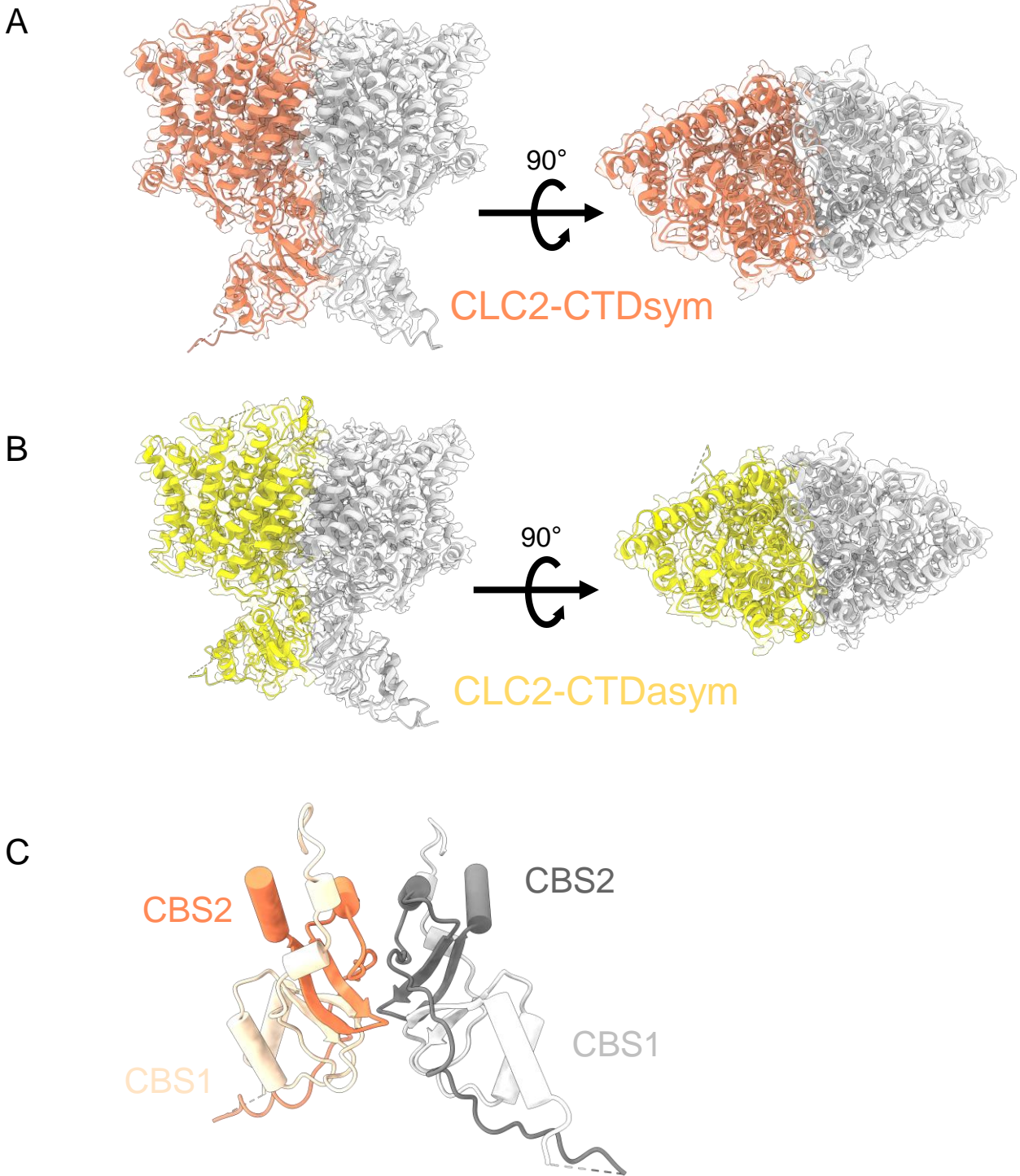


**Figure 4 – figure supplement 2. CryoEM density maps for the two CTD-containing CLC-2 conformations, overlaid with structural models. (A) CLC2-CTD<sub>sym</sub>. (B) CLC2-CTD<sub>asym</sub>. Side view (left) and top view (right) are shown. (C) CTD of CLC2-CTD<sub>sym</sub> shows two CBS domains on each subunit (orange and light orange for subunit A; gray and light gray for subunit B).**

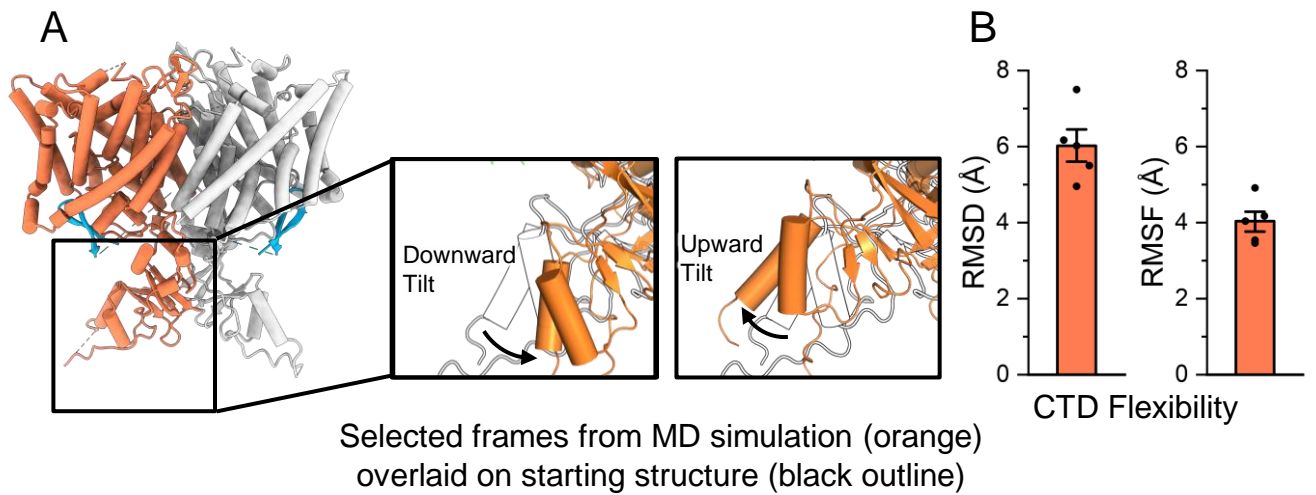


**Figure 4 - figure supplement 3. MD analysis indicates conformational flexibility of the CTD.** (A) The CTD is highly mobile relative to the transmembrane domain, and often tilts upward or downward relative to its initial location. In the inset images, two representative frames from simulation are shown (orange) overlaid on the starting structure (black outline). (B) The RMSD (root mean square deviation) and RMSF (root mean square fluctuation) of the cytoplasmic domain backbone were calculated after aligning frames on the transmembrane domains. Bars show the mean of five independent simulations, each 2.0  $\mu$ s in length. Error bars are 68% confidence intervals of the mean.



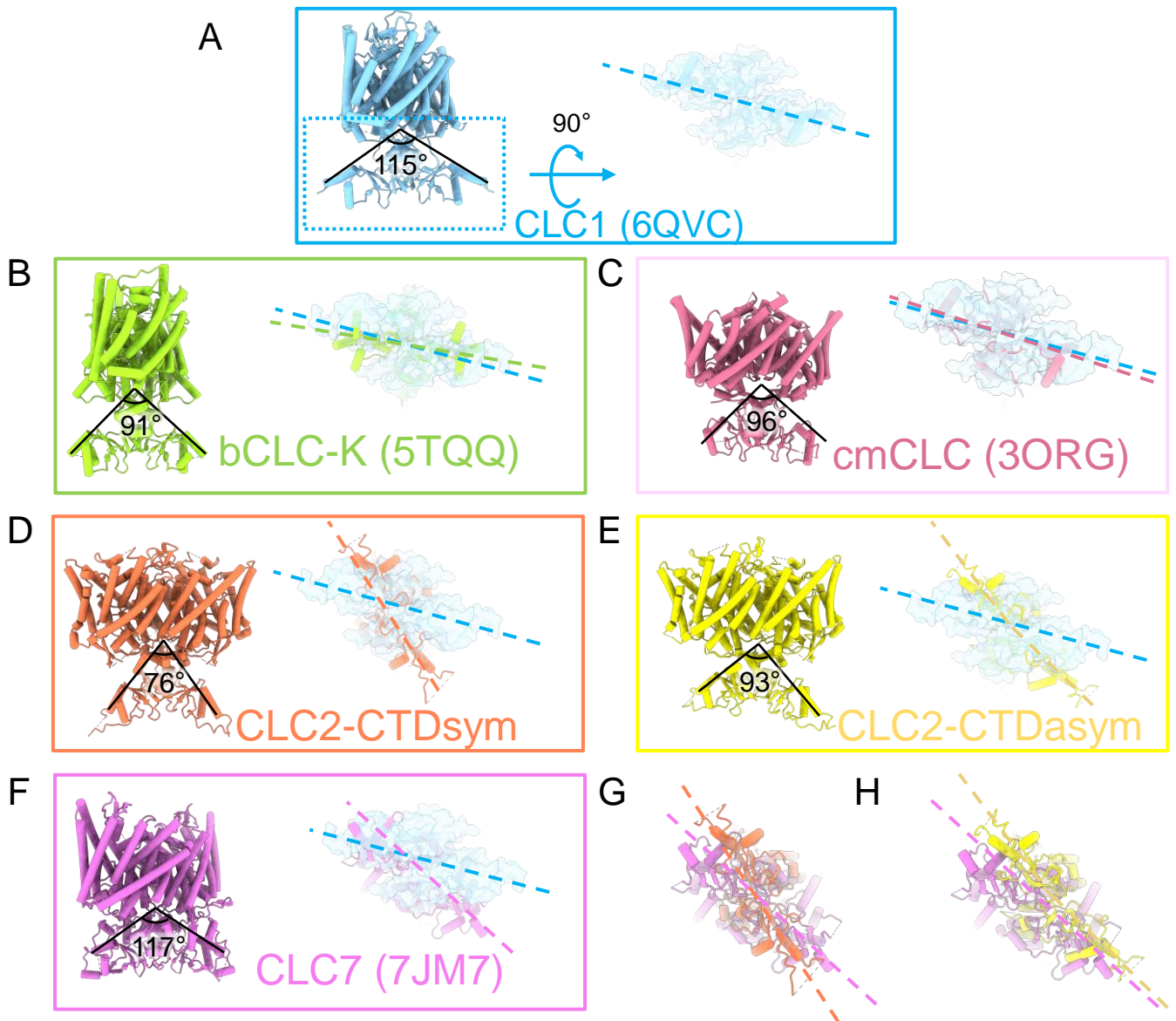


**Figure 4 - figure supplement 4. Comparison of CTD orientation with respect to the TM domain.** (A) The CLC-1 structure is shown in light blue. The angle of orientation for the CTDs was calculated using the far end residue of helix T (the second helix of first CBS domain) as the end point of rays and the center of the TM-CTD connecting plane as the vertex of the angle. On the right the CTD is shown in surface representation following rotation as indicated. Panels (B) – (F) show the CLC homolog indicated, with angles calculated as for CLC-1, and the rotated view of the CTD shown to compare the positioning of the CTDs relative to the membrane domains. The dashed lines indicate the long axes of the CTDs. In each panel, CLC-1 is shown in light blue as a reference for comparison. (G) and (H) overlays compare the CTD orientations in the CLC-2 structures to that in CLC-7. PDB IDs are shown in the parentheses. PDB IDs for CLC2-CTD<sub>sym</sub> and CLC2-CTD<sub>asym</sub> are 8TA4 and 8TA5.

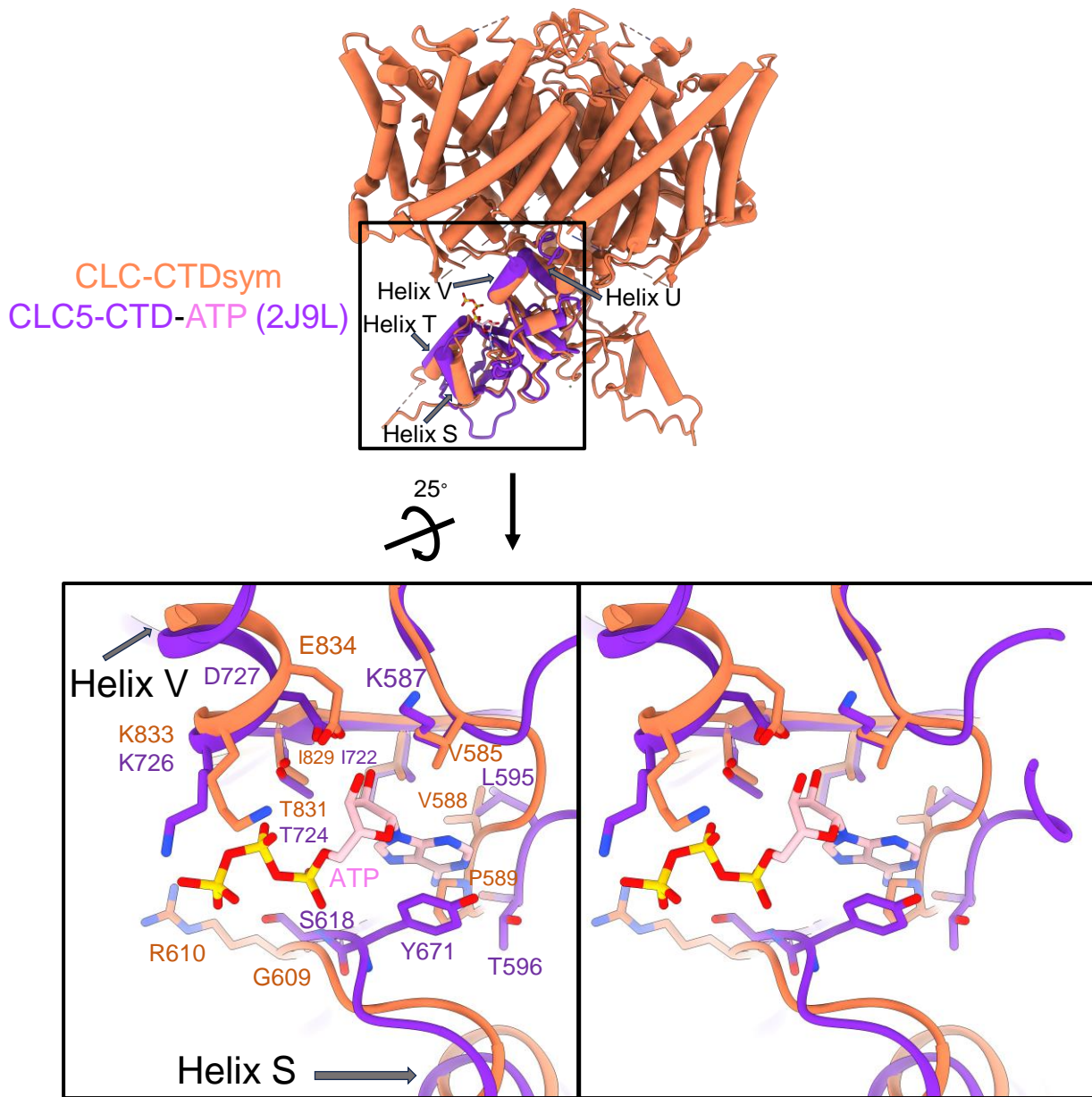


**Figure 4 – figure supplement 5. ATP binding site comparison between CLC-2 and CLC-5.** Top: Structural overlay of CLC2-CTD<sub>sym</sub> (in orange) and CLC5-CTD (in dark purple) with ATP (pink carbon atoms; CPK coloring on non-carbon atoms. PDB ID: 2J9L). Bottom: Zoomed in stereo view of ATP binding site in CLC5-CTD (dark purple) overlaid with the same region in CLC2-CTD<sub>sym</sub> (orange). Residue numbers are labeled in dark purple for CLC-5 and orange for CLC-2.

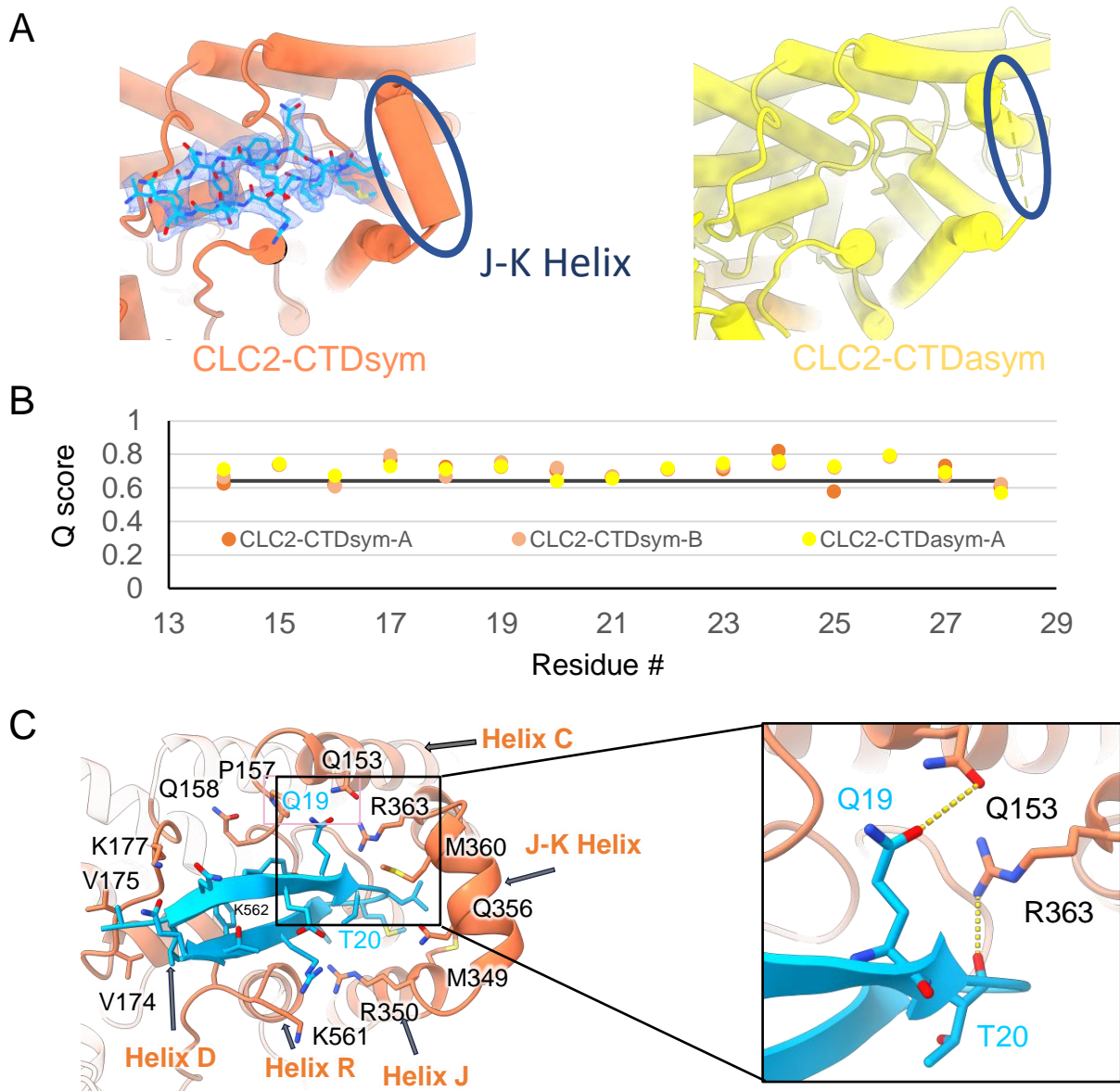
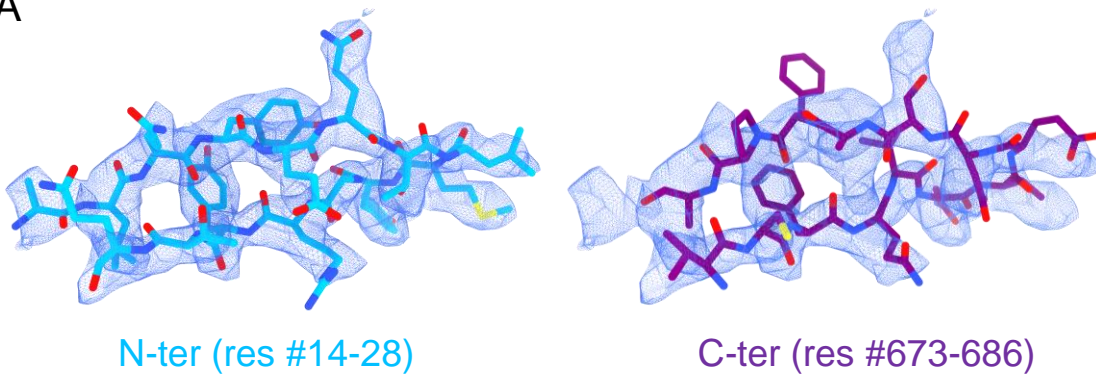


**Figure 5. The blocking hairpin structure corresponds to an N-terminal sequence of CLC-2.** (A) *Left:* The hairpin structure seen in the cryoEM density (blue mesh) fits N-terminal residues 14-28 (blue). *Right:* The subunit in CLC2-CTDasym structure that contains a CTD with rotated orientation lacks density for the hairpin structure. In this structure, the residues linking TM helices J and K are not resolved. The dark blue circles indicate this unresolved region (right panel) and the corresponding resolved J-K helix that occurs in the other subunits. (B) Model validation using Q-scores for the N-terminal hairpin: orange and light orange for subunits A & B of CLC2-CTDsym subunit; yellow for subunit A (the hairpin-containing subunit) of CLC2-CTDasym. The black line represents the expected Q-score at 2.75 Å based on the correlation between Q-scores and map resolution. (C) Residues on the transmembrane domain interact with the N-terminal hairpin. The J-K helical linker and TM Helices C, D, R, and J are labeled with arrows. Inset: Zoomed-in view of two hydrogen bonds formed between the hairpin structure and the TM domain: Q19-Q153 and T20-R363. Mutation of these two residues (Q25 and T26 in rat CLC-2) generated an open-channel phenotype for CLC-2 expressed in *Xenopus* oocytes (Grunder et al., 1992).



A



B

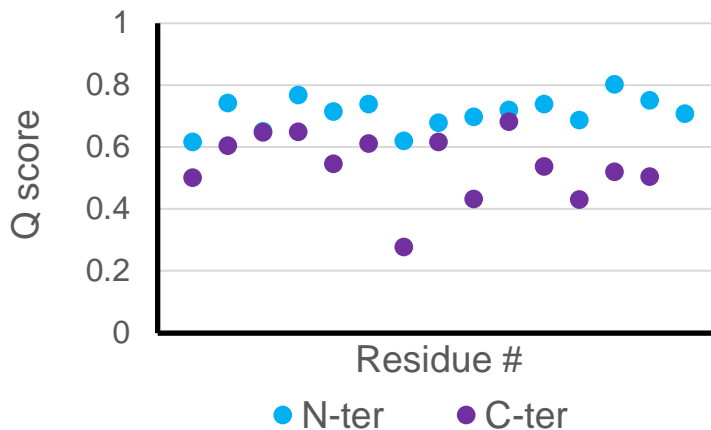
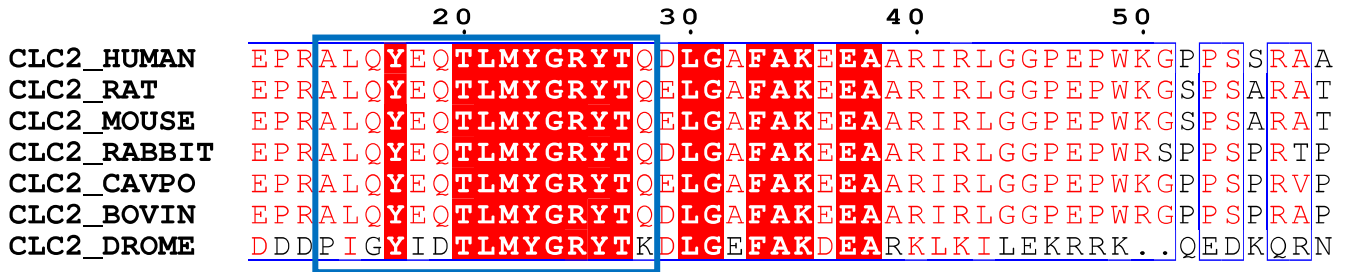
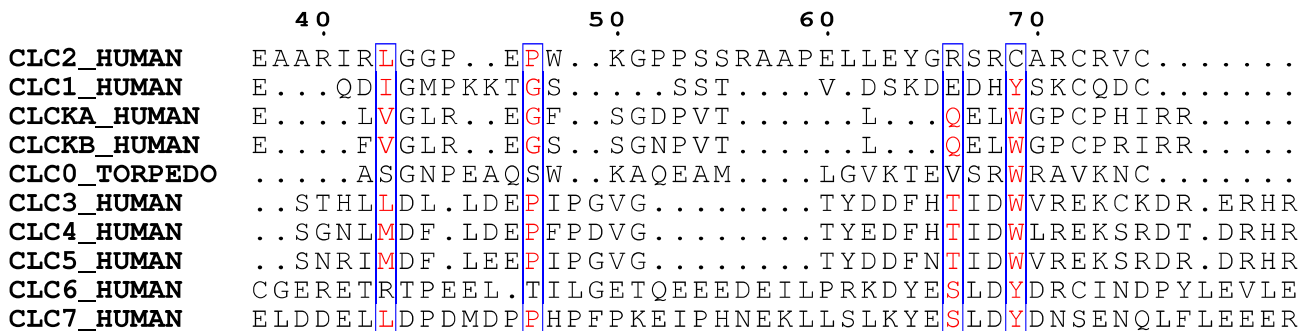
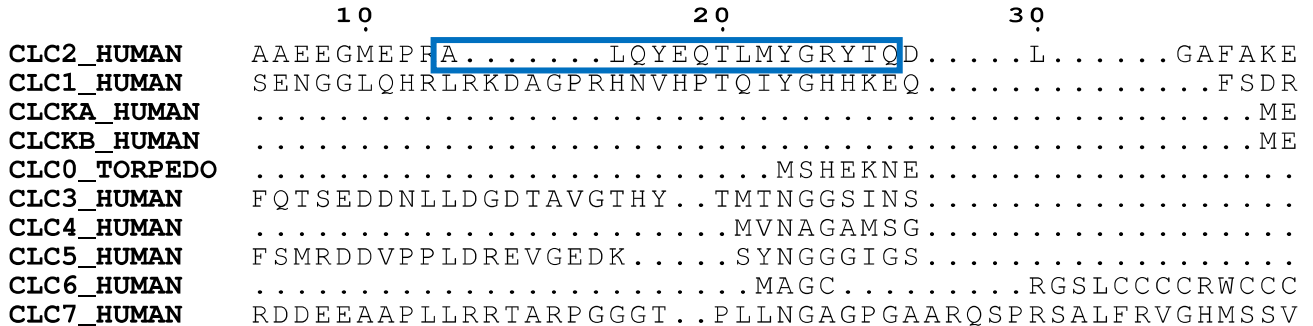


**Figure 5 – figure supplement 1.** Comparison of peptide candidates fitting into the hairpin density. **(A)** Best-fitting peptide candidate from the N-terminus (left shown in blue) and from the C-terminus (right shown in purple) fitted into cryoEM hairpin density (blue mesh). **(B)** Q-score plot of the two peptide candidates (residues 1-15 of the respective sequences). The Q-scores for the C-terminal peptide are generally lower than the Q-score expected for the corresponding resolution (0.65).

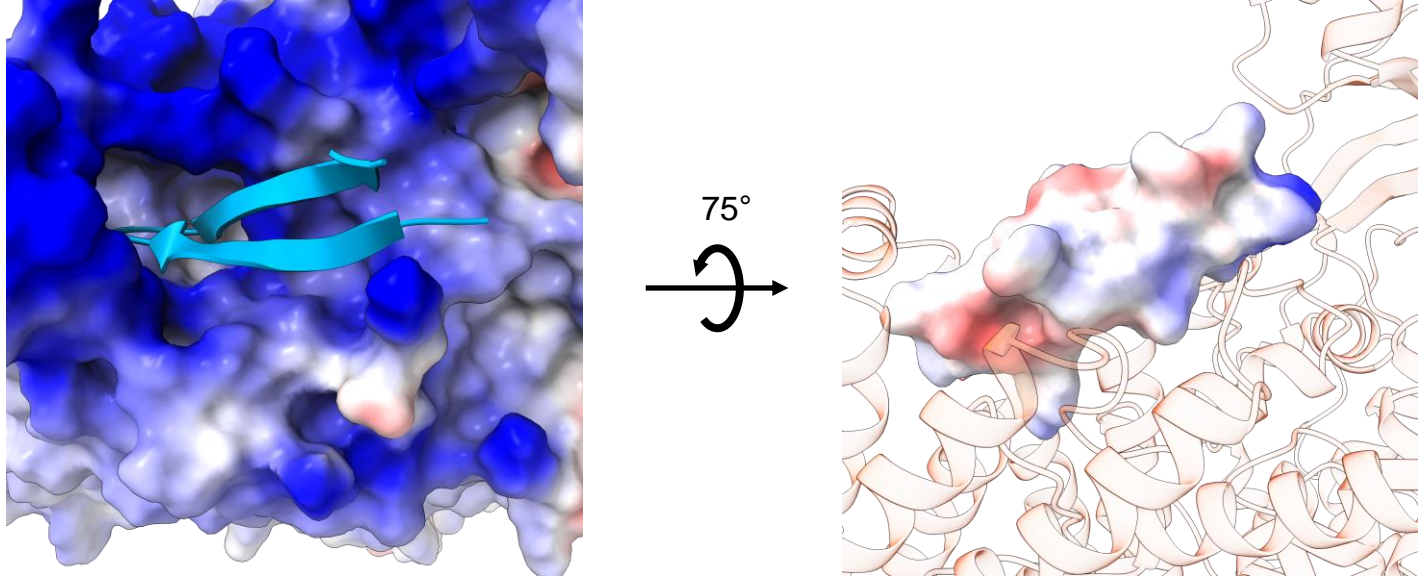
A



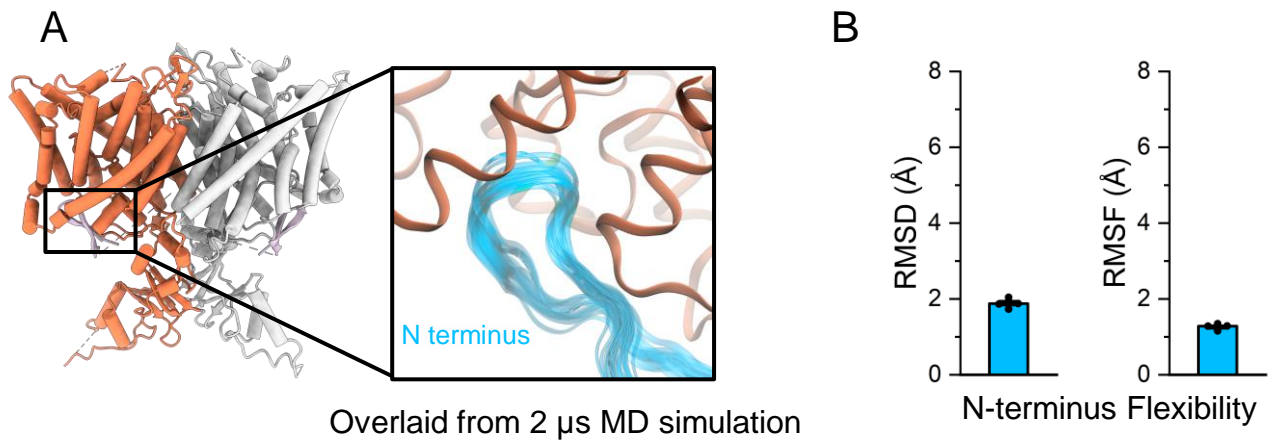
B



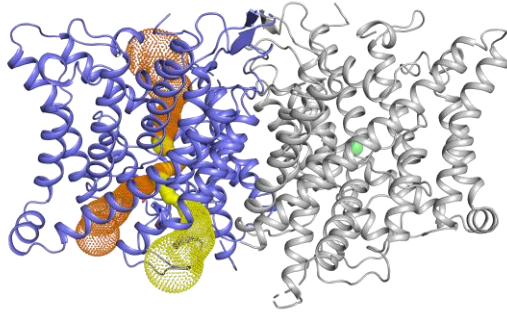
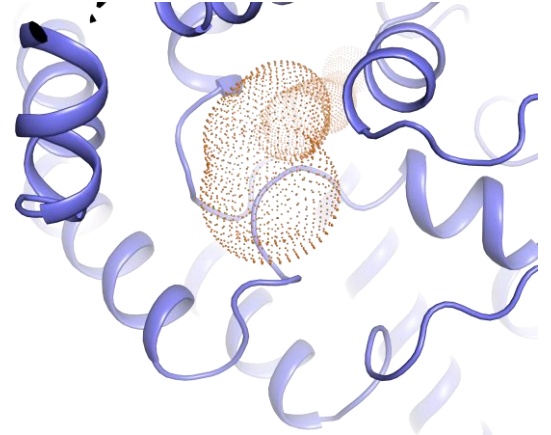
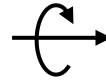
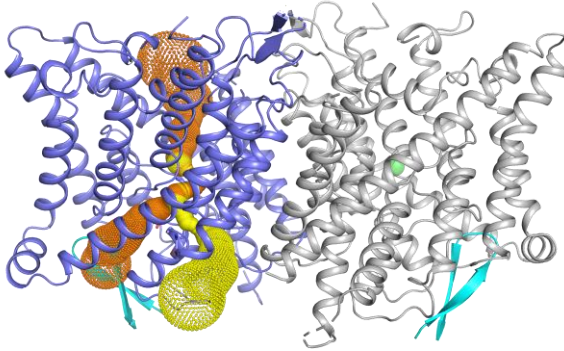
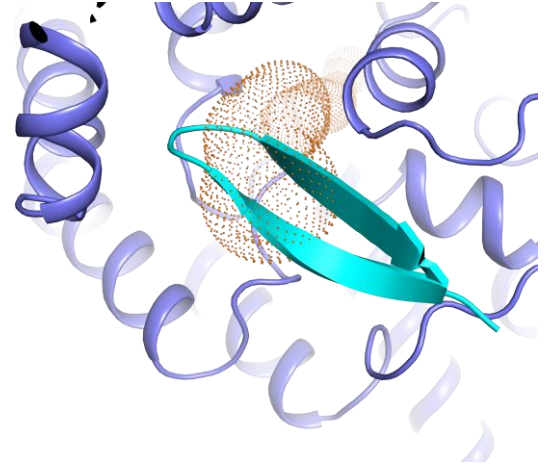
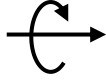
**Figure 5 – figure supplement 2. N-terminal hairpin sequence is conserved in CLC-2, but not other CLCs. (A)** Alignment of the N-terminal hairpin sequence (blue boxed) amongst different species. **(B)** Alignment of N-terminal hairpin sequence (blue boxed) amongst other human CLCs.



**Figure 5 – figure supplement 3.** Electrostatic map of the N-terminal hairpin blocking site. Left: view from the cytoplasm showing the electrostatic surface potential of the TM region (blue, positive; red, negative), with the hairpin shown in cartoon. Right: side view showing the electrostatic surface potential of the hairpin (blue, positive; red, negative) and the TM blocking site shown in transparent cartoon model.



**Figure 5 - figure supplement 4. MD simulations confirm the N-terminal hairpin structure is stable** (A) In simulations, the N-terminus (blue) remains stably bound to the intracellular side of the transmembrane domain (orange). In the inset image, frames of the N-terminus taken every 200 ns from a representative simulation are overlaid. (B) The root-mean-square deviation (RMSD) and root-mean-square fluctuation (RMSF) of the N-terminus backbone were calculated after aligning frames on the transmembrane domains. Bars show the mean of five independent simulations, each 2.0  $\mu$ s in length. Error bars are 68% CI (confidence interval of the mean).

**A**90°  
**B**90°  


**Figure 5 - figure supplement 5.** The N-terminal hairpin blocks the primary Cl<sup>-</sup> pore in CLC-2. **(A)** *Left:* Side view of CLC2-TM showing the caver-detected pore (primary in orange and secondary in yellow). *Right:* View of the primary pore from the intracellular side. **(B)** The N-terminal hairpin (blue) overlaid with CLC2-TM as shown in panel **A**.

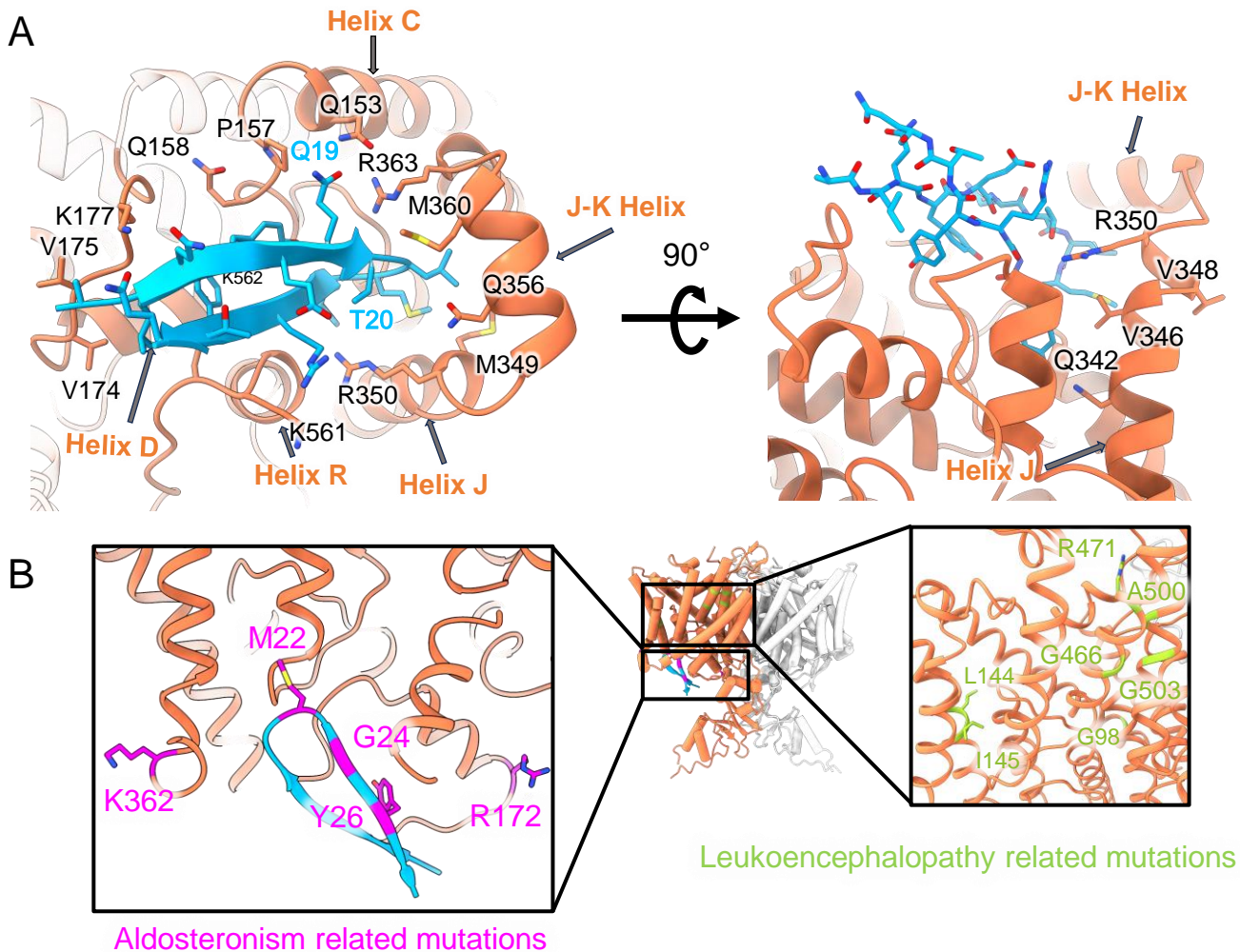


**Figure 5 – figure supplement 6. Mapping mutant data onto the cryoEM structure. (A)** Left: same as Figure 5C, showing hairpin interactions. Right: Rotated view highlighting ball “receptor” residues identified by Jordt and Jentsch, 1997. **(B)** Residues mutated in human Aldosteronism (Fernandes-Rosa et al., 2018, Scholl et al., 2018) and Leukoencephalopathy (Hector Gaitan-Penas., 2017) are shown on CLC2-CTDsym in magenta and green, respectively.



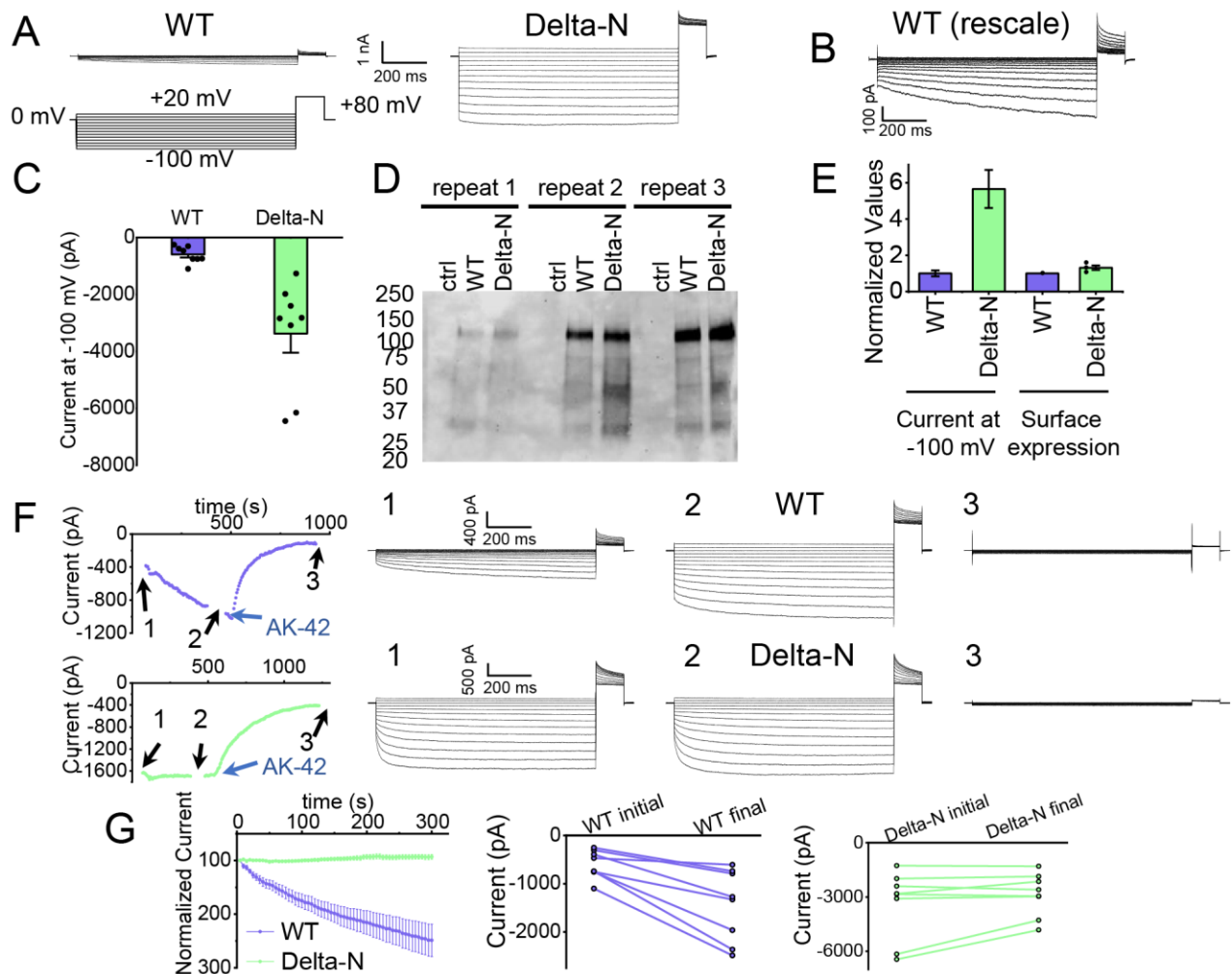


**Figure 6 Patch-clamp experiments support CLC-2 channel block by the N-terminal hairpin structure.**

(A) Representative currents from WT and Delta-N CLC-2, recorded using the whole-cell patch clamp configuration in response to the voltage protocol shown. (B) WT CLC-2 recording from panel A, shown on an expanded scale. (C) Summary of current levels measured for WT and Delta-N CLC-2 at the end of the 1-s voltage pulse to -100 mV. Data are from six independent transfection samples, in each case with WT and Delta-N recorded on the same day following transfection. WT:  $-600 \pm 102$  pA (SEM, n=8); Delta-N:  $-3300 \pm 630$  pA (SEM, n=8). (D) Western blot detection of biotinylated surface-expressed CLC-2 from three independent experiments. (E) Summary data for electrophysiology and surface-biotinylation experiments. Points representing individual experiments for Delta-N surface biotinylation (each normalized to WT) are shown. Individual data points for the electrophysiology experiments are shown in panel C. (F) Representative examples of experiments to evaluate current run-up in WT and Delta-N CLC-2. *Left panels*: Time course data. Following an initial voltage-family measurement (I-V protocol as in panel A, taken at point “1”), currents were monitored by 1-s pulses to -100 mV every 5 s for five minutes, after which a second voltage-family measurement was made (point 2), followed by application of AK-42 to facilitate leak subtraction, and a final voltage-family measurement at point 3. I-V traces are shown at right. (G) Summary data for “run-up” experiments. *Left panel*: Normalized time-dependent currents for WT and Delta-N. Currents were first leak-subtracted (using the steady-state current after AK-42 application) and then normalized to the amplitude of the current measured in the first step of the 5-minute sequence. *Right panels*: Leak-subtracted current levels at -100 mV from “initial” and “final” IV traces measured at points “1” and “2” in the time course (panel F). Average initial and final currents (pA  $\pm$  SEM, n=8) are WT:  $-600 \pm 102$  and  $-1400 \pm 260$ ; Delta-N:  $-3300 \pm 630$  and  $-2900 \pm 420$ .



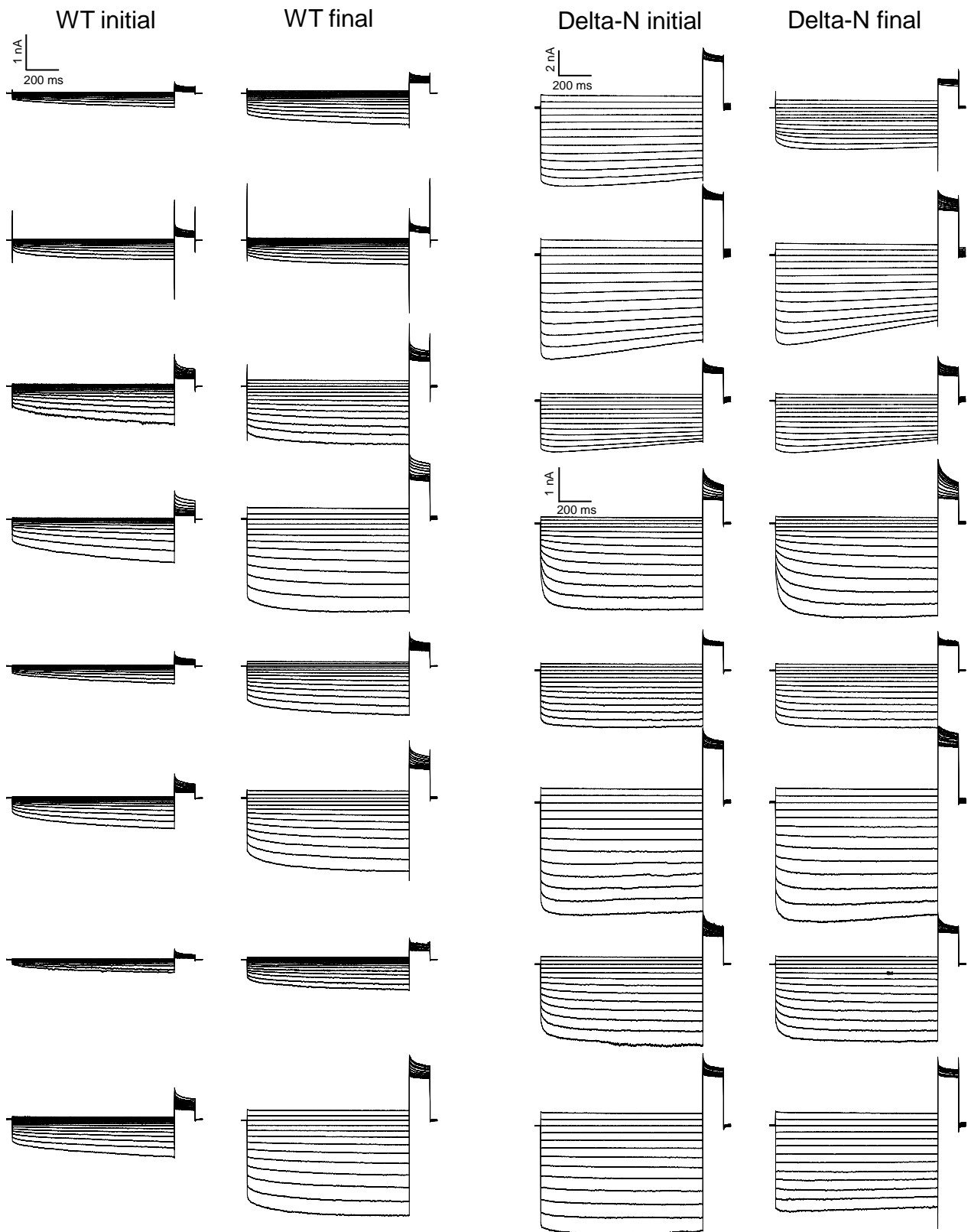


**Figure 6 – figure supplement 1.** Data traces from the CLC-2 run-up experiments summarized in Figure 6G. For Delta-N, separate scale bars indicate the currents for the top six and bottom 10 traces. AK-42 leak currents, not subtracted in these raw data traces, are summarized in Figure 6 – source data 1.

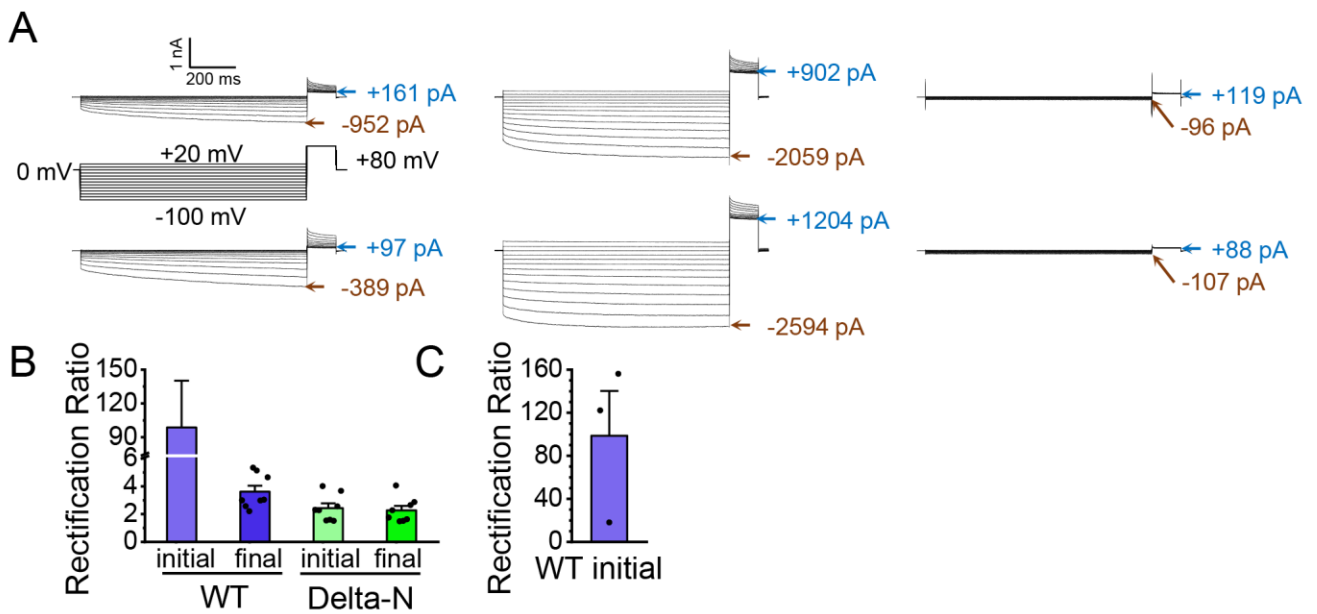


**Figure 6 – figure supplement 2. CLC-2 current rectification.** (A) Example traces from two experiments on WT CLC-2. Current values at end of the -100-mV test pulses and in the steady-state portion of the +80-mV tail pulse (following the +20-mV test pulse) are indicated. Robust AK-42 inhibition of the current at +80 mV indicates that CLC-2 is passing current at positive voltages. (B) Rectification ratios. Rectification was quantified by taking the ratio (absolute value) of the leak-subtracted currents at -100 mV and +80 mV. For WT initial currents, the low currents at +80 mV make this quantification challenging: for 5 out of 8 experiments on WT CLC-2, the AK-42 current at +80 mV was greater than the initial WT current at +80 mV, likely due to an increase in leak over the course of the experiment (~15 minutes of voltage pulsing). Therefore, the rectification calculated for the WT initial currents ( $99 \pm 34$ , SEM  $n=3$ ) has substantial uncertainty. That said, such high rectification is consistent with reports of CLC-2 rectification throughout the literature (Park et al., 1998; Arreola et al., 2002; Jentsch and Pusch, 2018). On the other hand, Delta-N currents display only mild rectification, which is straightforward to quantify given the high signal:noise (high AK-42-sensitive current relative to background), and which does not change in response to voltage pulsing. For “WT-final”, the rectification ratio similarly can be accurately quantified. Thus, while the high uncertainty and variance in estimating WT initial rectification precludes quantitative statistical comparisons, these data strongly suggest that WT CLC-2 current rectification decreases in parallel to current run-up. (C) WT initial rectification ratio from panel B replotted to show the individual data points from the 3 experiments in which AK-42 current at +80 mV was less than the initial WT current at +80 mV. Data for all experiments are summarized in Figure 6 – source data 1.

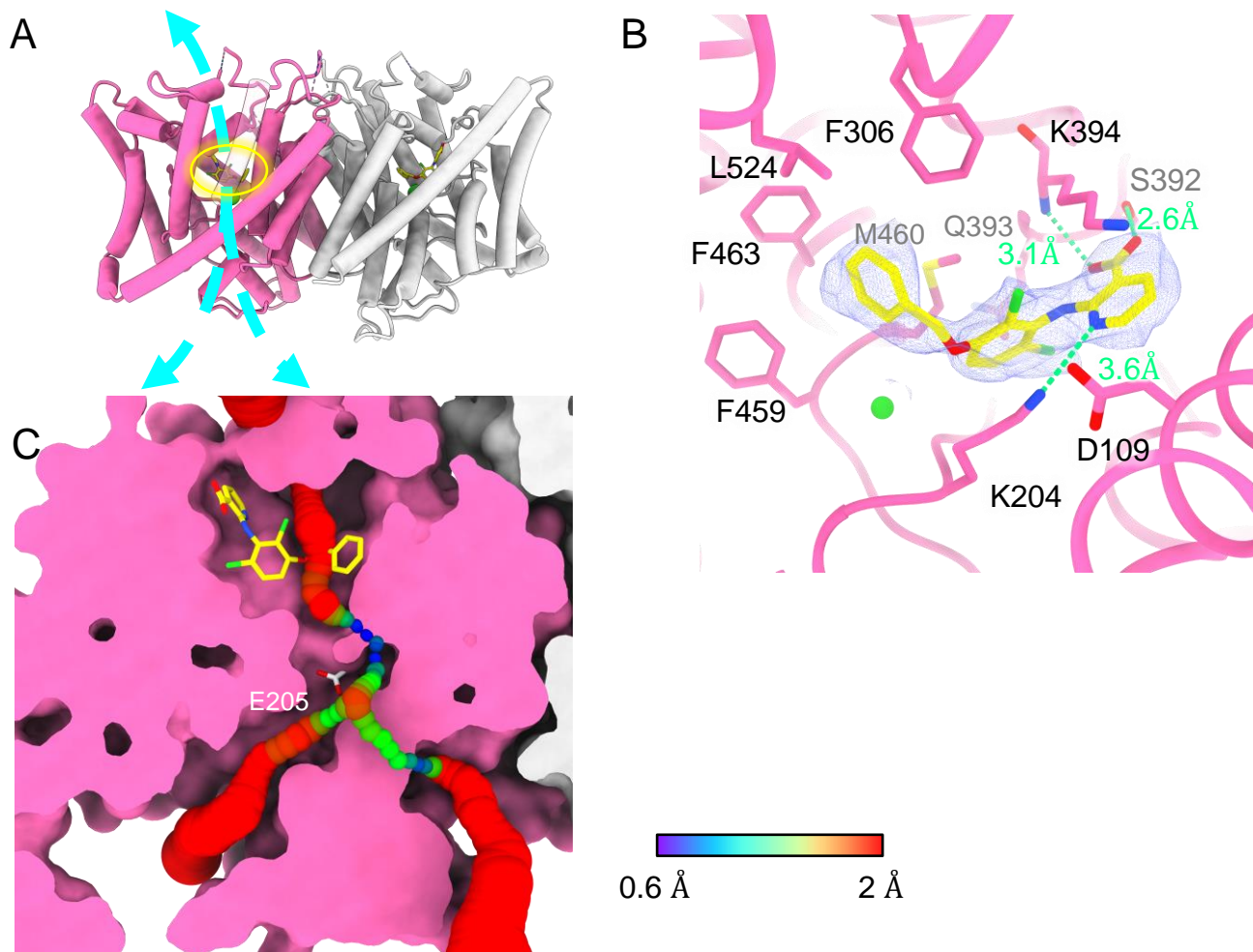


**Figure 7 Bound AK-42 blocks the Cl<sup>-</sup> pathway in CLC-2.** (A) TM-domain structure of the CLC-2 structure in complex with AK-42 (CLC2-TM-AK42) at 2.74 Å. The identical subunits of the homodimer are shown in hot pink and gray; Cl<sup>-</sup> ions are shown as green balls. Bound AK-42 is highlighted with a yellow circle on the pink subunit. The cyan arrow indicates the Cl<sup>-</sup> pathway. (B) Zoomed-in view of the AK-42 binding site (contour level: 0.91, 6.0  $\sigma$ ). (C) A sliced view of CLC-2 showing AK-42 (yellow carbon atoms; CPK coloring on non-carbon atoms) and E<sub>gate</sub> (CPK sticks). Both AK-42 and E<sub>gate</sub> obstruct the Cl<sup>-</sup> pathway, displayed as a color map.

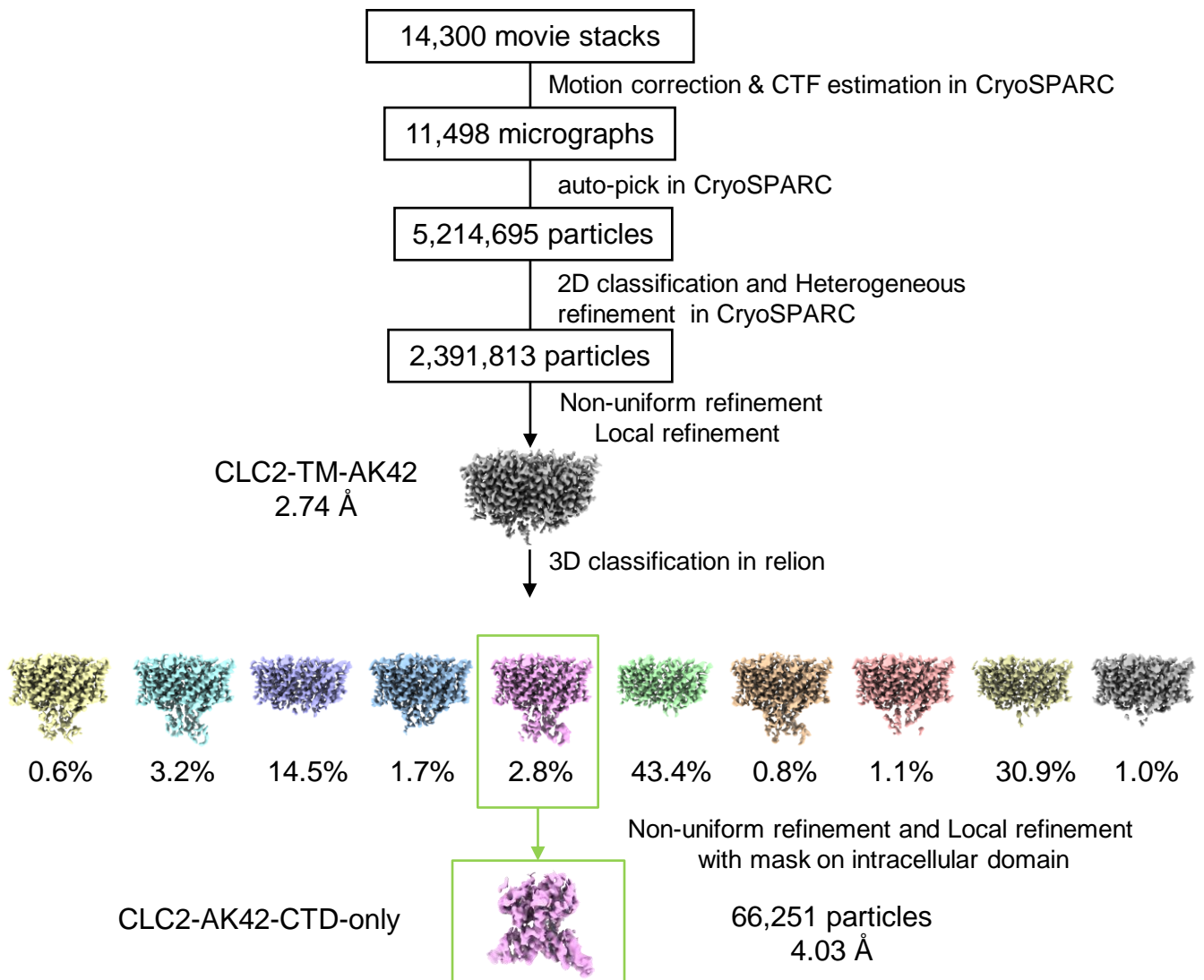


**Figure 7 - figure supplement 1. cryoEM workflow of the CLC2-TM-AK42 single-particle cryo-EM data processing.** A total of 14,300 movie stacks were collected on a 300 kV Titan Krios cryo-electron microscope. cryoSPARC was used for 2D classification and CLC2-TM-AK42 density map was obtained after 2D classification. Relion was used for 3D classification.

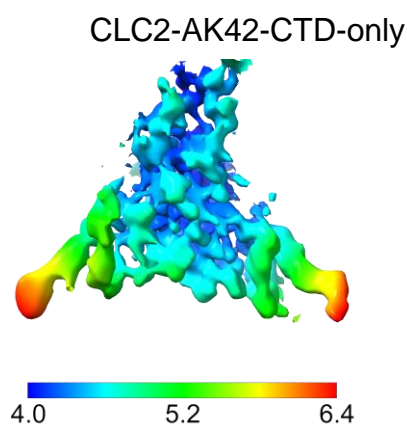
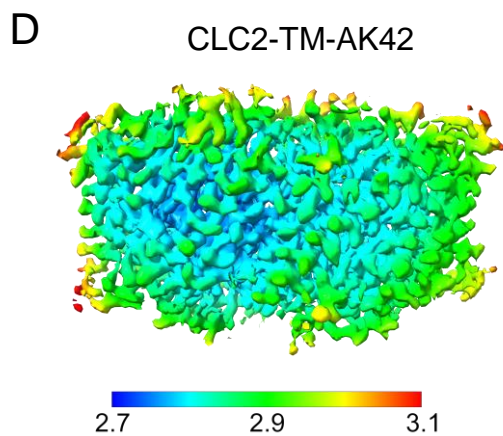
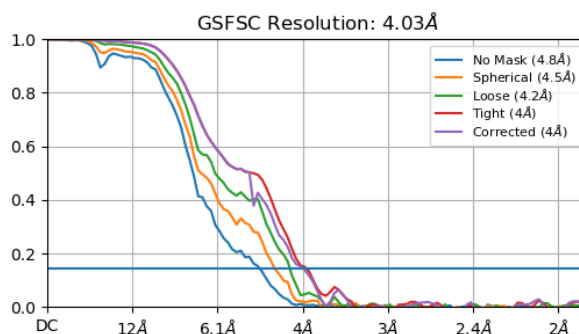
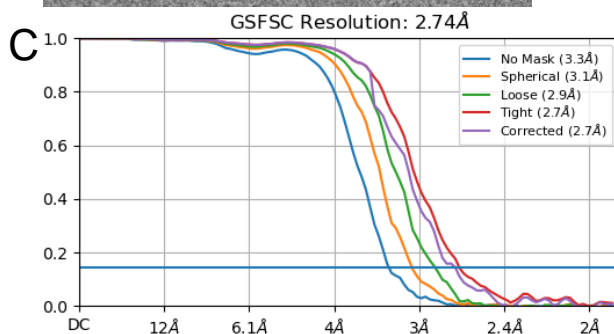
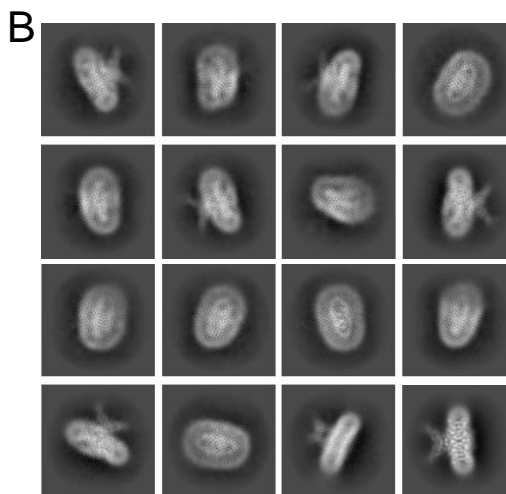
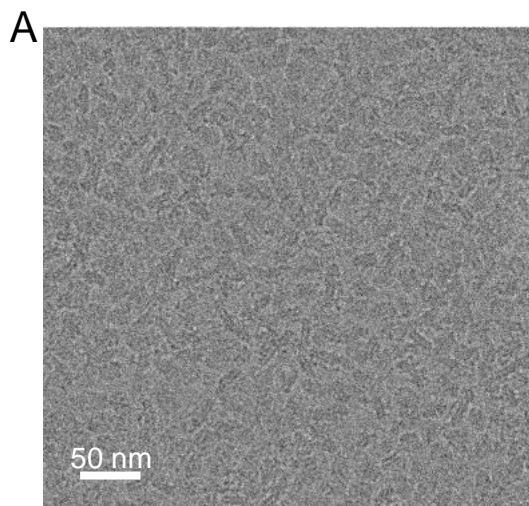


**Figure 7 - figure supplement 2.** Micrograph and 2D classes and structure validation of CLC2-AK42. (A) Representative motion-corrected cryo-EM micrograph. (B) 2D class averages. (C) Gold standard FSC plots calculated in cryoSPARC for CLC2-TM-AK42 (left) and CLC2-AK42-CTD-only (right). (D) Local resolution of the cryo-EM map for CLC2-TM-AK42 (left) and CLC2-AK42-CTD-only (right)

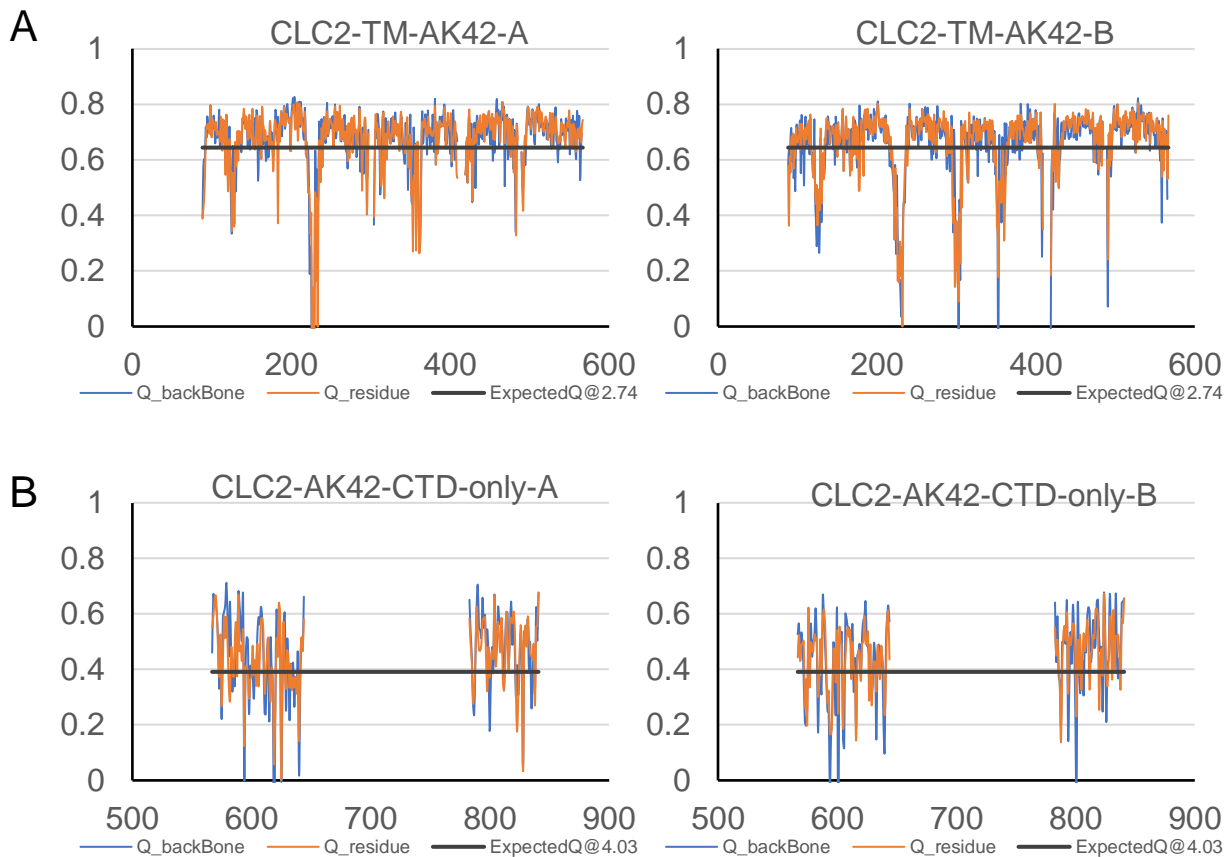


**Figure 7 - figure supplement 3. Model validation using Q-scores. (A)** Q-scores of CLC2-TM-AK42 for subunit A (left) and subunit B (right). **(B)** Q-scores of CLC2-AK42-CTD-only for subunit A (left) and subunit B (right). The black line represents the expected Q-score at respective resolution based on the correlation between Q-scores and map resolution.



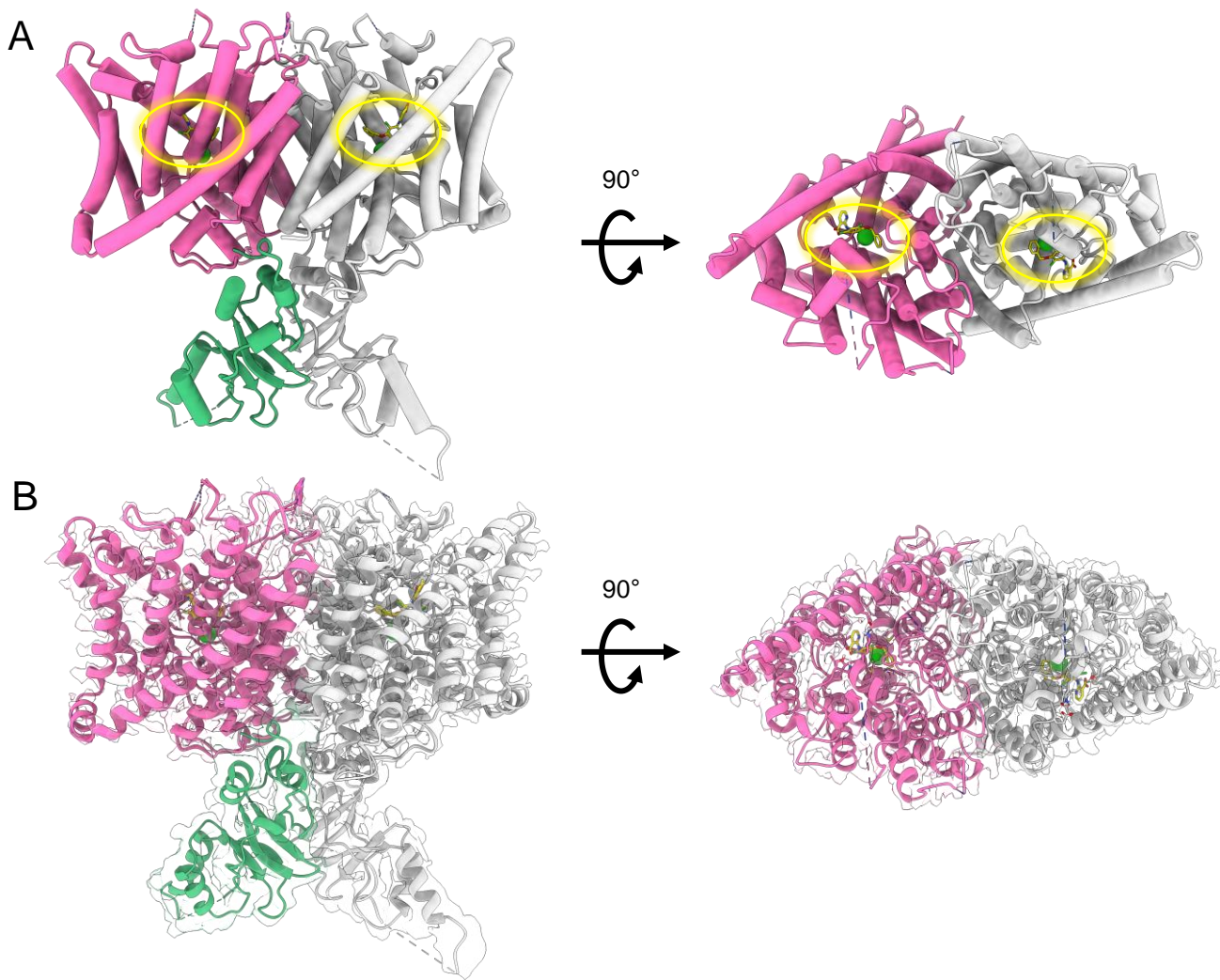


**Figure 7 - figure supplement 4. cryoEM map and structure of CLC2-AK42. (A)** cryoEM model of CLC2-TM-AK42 with docked CTD. The transmembrane region is shown in hot pink and gray. The CTD is shown in green and gray. AK-42 is shown in yellow and highlighted by yellow circles. Chloride ions are shown in green. **(B)** cryoEM model overlay with density map of CLC2-AK42. Contour level: 0.83, 6.8  $\sigma$  (TM region); 0.35, 14  $\sigma$  (CTD).

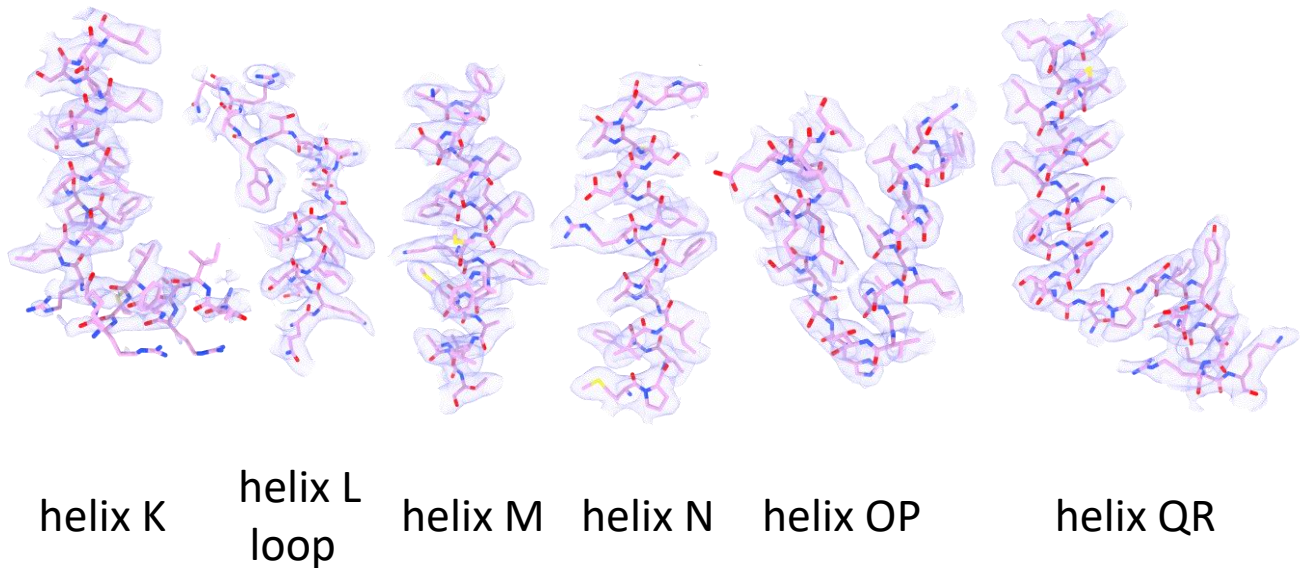
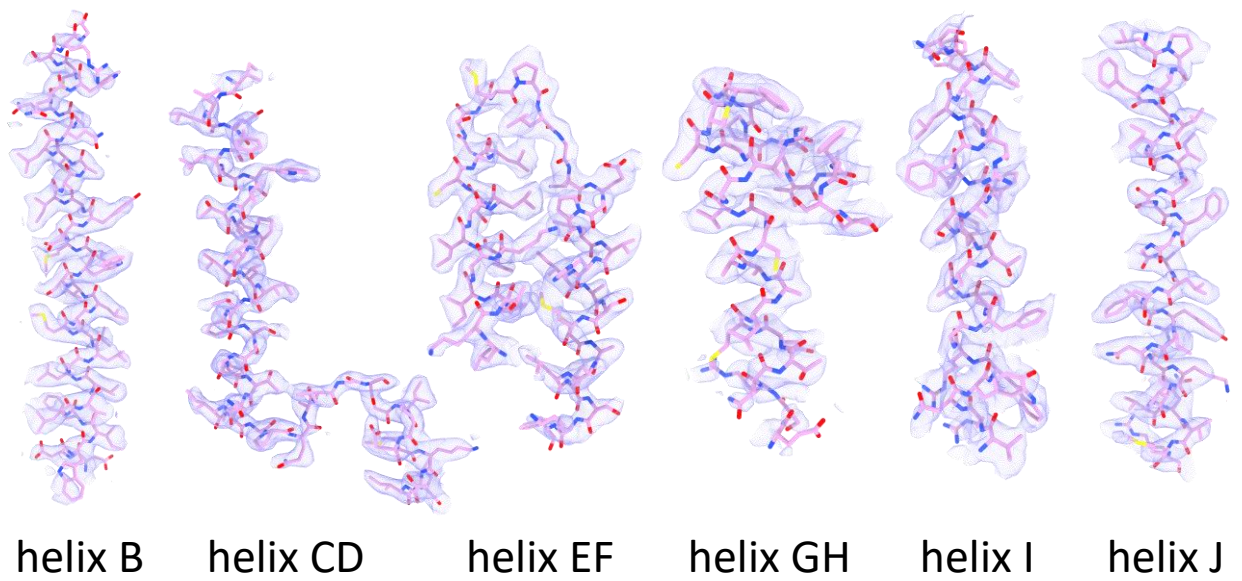


**Figure 7 - figure supplement 5. Helix map of CLC2-TM-AK42.** cryo-EM densities and model of CLC2-AK42 transmembrane helices (contour level: 0.52, 3.4  $\sigma$ ).

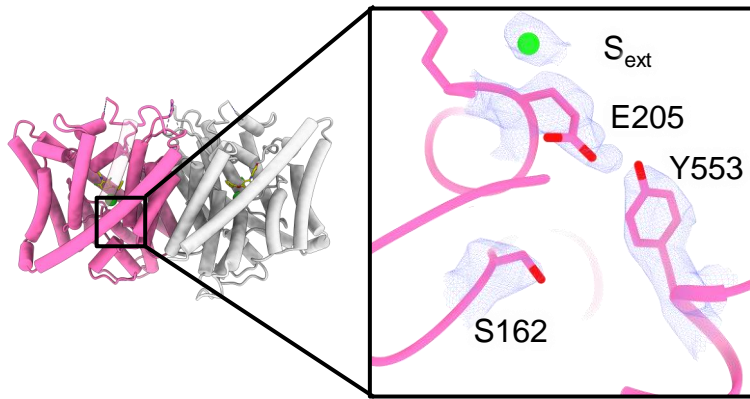


**Figure 7 – figure supplement 6. Density overlay at key Cl<sup>-</sup>-pathway residues.** Zoomed-in view highlighting residues S162, E205, Y533, and the bound chloride ion, with cryoEM density overlay (contour level: 1.4, 9.0  $\sigma$ ).

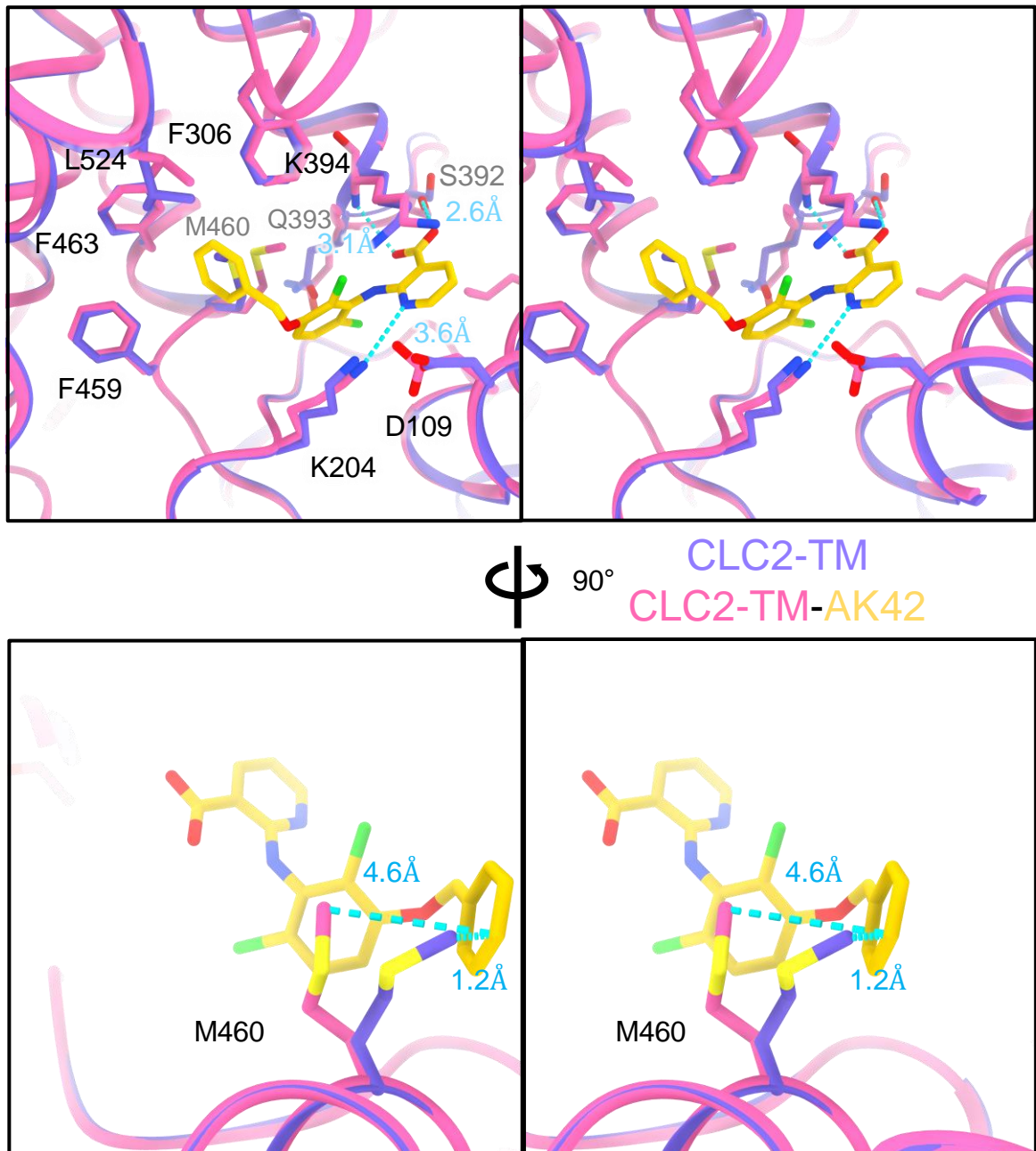


**Figure 7 - figure supplement 7. AK-42 binding site comparison between CLC2-TM and CLC2-TM-AK42.** Top: Stereo view of structural overlay at the AK-42 binding site. Hydrogen bonds between AK-42 and residues K204,S392,K394 are indicated by blue dashed lines. Bottom: A view highlighting the movement of residue M460 to make space for AK-42.



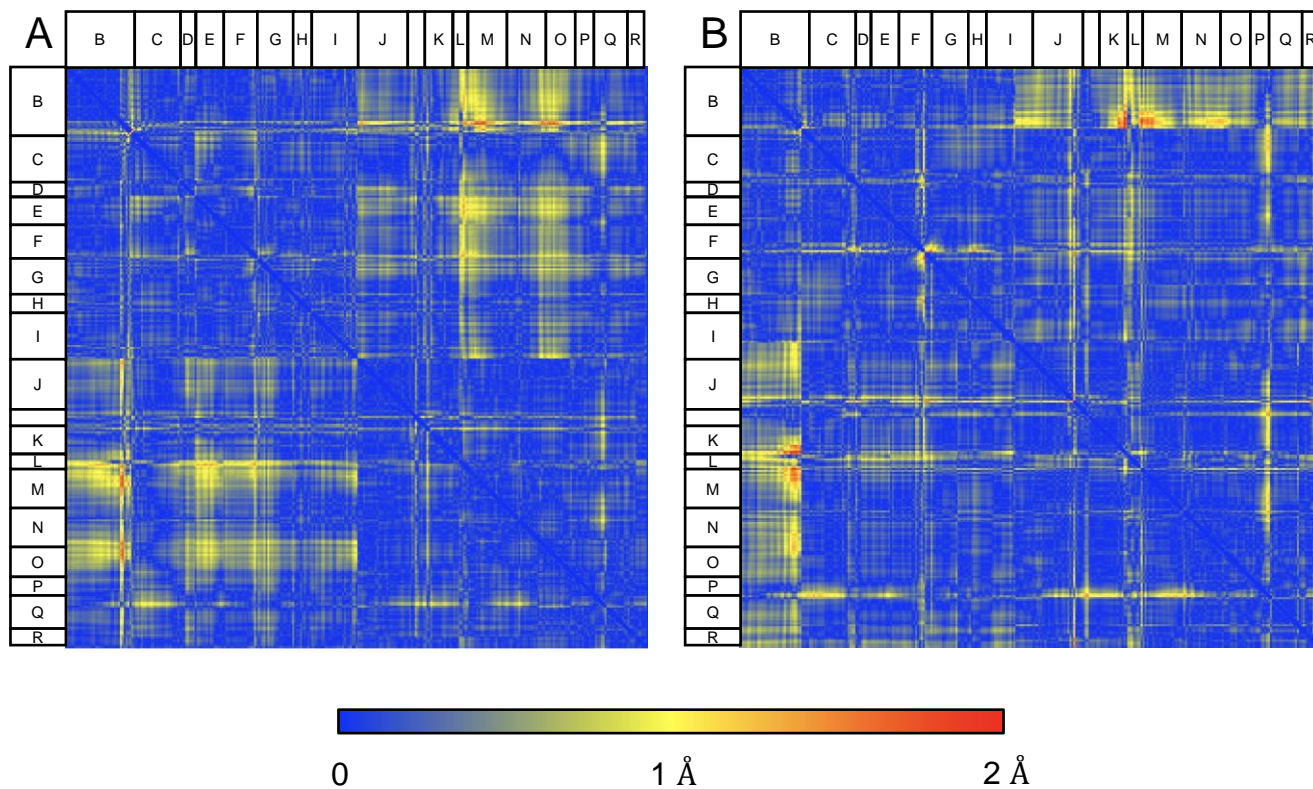
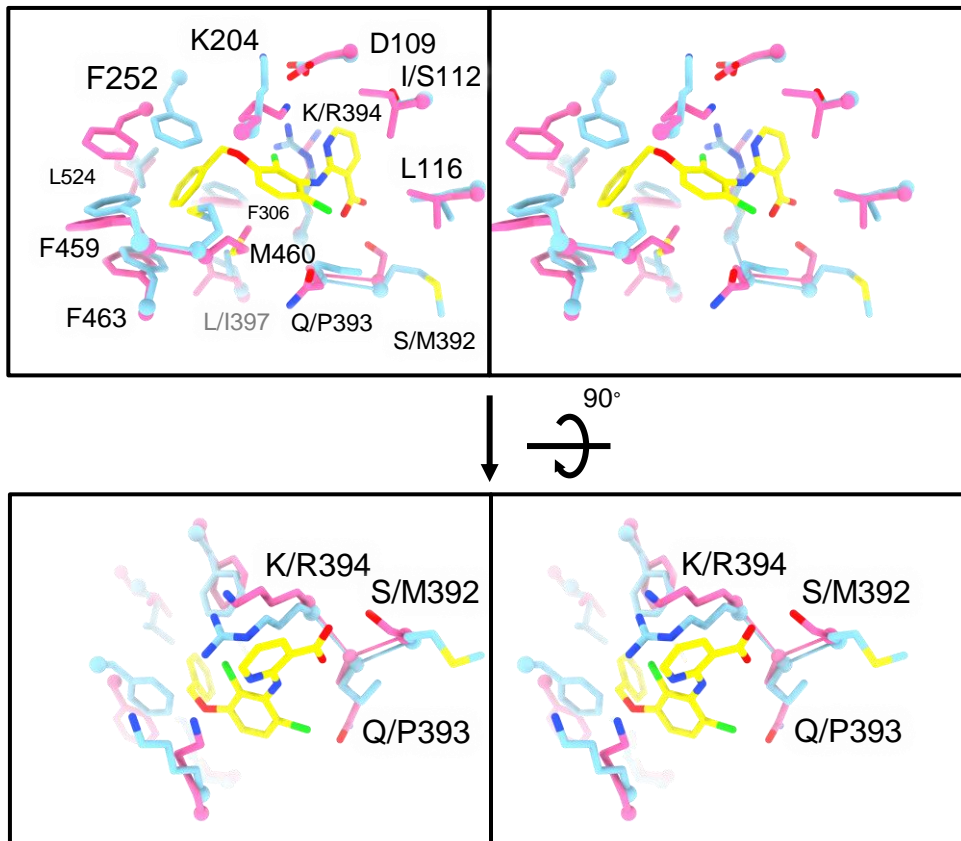


**Figure 7 - figure supplement 8. Structural comparison of CLC2-TM and CLC2-TM-AK42.** Difference distance matrices comparing Ca residues on TM helices between CLC2-TM and CLC2-TM-AK42 in subunits A (**A**) or B (**B**). Residues in loops connecting helices, where there is low confidence in the model building (Q score lower than the expected Q score of 0.65), were omitted from the matrices.

A



B

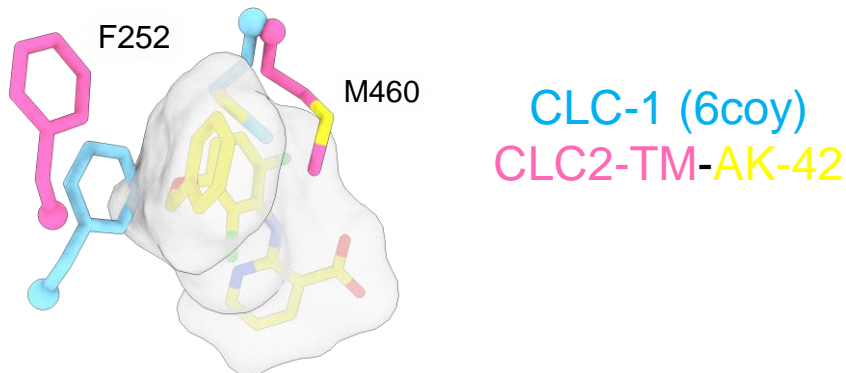


**Figure 7 - figure supplement 9 AK-42 binding site comparison between CLC-2 and CLC-1.** (A) Top: Stereo view of the AK-42 binding site in CLC2-TM-AK42 (hot pink) overlaid with the same region in CLC-1 (blue, PDB:6coy). Residue numbers correspond to those of CLC-2. The five residues that differ between CLC-2 and CLC-1 are: I112 (S139), S392 (M419), Q393 (P420), K394 (R421), and L397 (I424). Bottom: Rotated (stereo) view of AK-42 binding site to compare residues S392, Q393 and K394 in CLC-2 versus M419, P420 and R421 in CLC-1. These three were calculated to contribute most significantly to the AK-42 binding energy (Ma, 2023). (B) Residues in CLC-1 predicted to clash with AK-42. AK-42 is shown in yellow sticks and white surface. F252 and M460 in CLC-2 correspond to F279 and M485 in CLC-1.



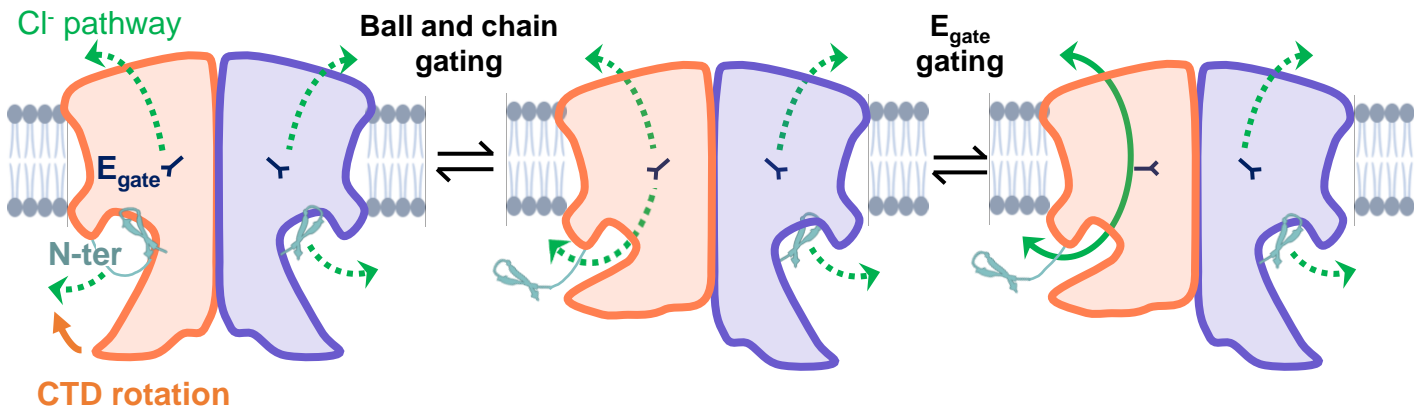


**FIGURE 8:** CLC-2's gating is illustrated based on our new structural data. Opening of each protopore requires at least two events – unblock by the N-terminal hairpin (“N-ter”) and rotation of E<sub>gate</sub> away from the permeation pathway. The dashed green arrow represents the Cl<sup>-</sup> conduction pathway. Hairpin unblock (ball and chain gating) is coupled to conformational change of the CTD: rotation of the CTD towards the membrane precludes hairpin binding, thus facilitating channel opening. Opening of the channel pore following these two events is depicted for one subunit of the homodimer (filled green arrow).